



**University of
Nottingham**

UK | CHINA | MALAYSIA

Predicting Process-induced Distortion for Composite Structures

Thesis submitted to the University of Nottingham for the degree of
Doctor of Philosophy, March 2024.

Shuang Yan

4342144

Supervised by

Prof. Nicholas Warrior

Dr. Mikhail Matveev

Abstract

Process-induced distortion (PID) is inevitable during the manufacturing of composite structures. A precise prediction of PID would benefit the design and manufacturing process so that the dimensional accuracy of the produced composite part is within tolerance. In this work, a sequentially coupled thermal-chemical and mechanical model was developed to predict the chemical, thermal and tool-part interaction (TPI) effects contributing to PID. The proposed model was based on the Cure Hardening Instantaneous Linear Elastic (CHILE) constitutive law and executed within ABAQUS finite element analysis, with the mechanical and thermal material properties defined through user subroutines.

As a starting point, this work presented a Matlab model based on forward discretisation method. This model provides a good opportunity to rapidly estimate the DoC and residual stresses distribution through the thickness of a laminate under an autoclave cure cycle, so that the validity and the effectiveness of the manufacturing recommend cure cycle (MRCC) could be examined.

This work then investigated the spring-in and warpage distortions in relating to the geometric features of composite structures. Subsequently, experimental and numerical investigations of PID in L-shaped laminates were performed. The specimens were manufactured using IM7/8552 UD prepregs under autoclave cure processing conditions. Factors contributing to the PID were isolated and the mechanism of each

was discussed in details. The study found that the corner component of spring-in was primarily the results of chemical and thermal shrinkage, while the warpage in the flange part was found to have strong dependence on tool-part interactions.

The novelty presented in this work is to quantify TPI effects through a semi-empirical approach. An equivalent shear stress can be determined through a set of experimental data, so that it could be implemented in the modelling to replicate the warpage distortion occurred in the flat part of a laminate. The validity and limitations of the proposed TPI model on L-shaped laminates were also discussed.

Following that, the study extended its modelling approach to predict PID of laminated structure with thickness reduction along the length, exploring different ply-drop designs. Parameters include dropped ply orientation and number of dropped plies. This work found that the lay-up sequence at the ply-drop zone is crucial in determining the out-of-plane displacement. The study also found that the magnitude of warpage due to the TPI effect is still a major factor. Therefore, the importance of precise modelling of TPI effect was emphasised. The study also demonstrated that although mechanical performance is the design priority for tapered laminates, the PID could also be mitigated if handled properly in the design stage.

Acknowledgements

Firstly I wish to express my sincere gratitude to my supervisors, Dr Mikhail Matveev and Professor Nicholas Warrior for their continuous support and encouragement throughout this PhD. Their expertise and guidance have been an invaluable asset to me during this rewarding journey.

Special thanks go to Dr Wenxuan Qi for spending numerous hours helping me to overcome challenges encountered during this PhD. Gratitude is also extended to Paul Johns and Liam Sprake for their technical assistance. I would also like to thank Philippe Bastid for his mentoring during my times at TWI Cambridge.

The author gratefully acknowledges the financial supports from the University of Nottingham Faculty of Engineering, TWI NSIRC and the EPSRC Future Composites Manufacturing Research Hub (EP/P006701/1).

Lastly, my deep gratitude must go to my parents and my boyfriend for their unwavering support and encouragement throughout this academic endeavour.

Contents

Abstract	i
Acknowledgements	iii
List of Tables	xi
List of Figures	xii
Chapter 1 Introduction	1
1.1 Background	1
1.2 Autoclave Process	2
1.3 Process-induced Distortions	3
1.4 Research Objectives	5
1.5 Thesis Outline	5
Chapter 2 Literature Review	7
2.1 Introduction	7
2.2 Mechanisms of Distortion	7
2.2.1 Thermal Effect	7
2.2.2 Chemo-rheological Effect	9
2.2.3 Tool-Part Interaction Effect	11
2.3 Current Studies on Predicting PIDs	12
2.3.1 Analytical Model of Predicting PIDs	12
2.3.2 Numerical models of Predicting PIDs	13
2.4 Factors Contributing to PIDs	16
2.4.1 Current Studies on TPI Effects on PIDs	17
2.4.2 Current Studies on Ply-drop Effects on PIDs	19

2.5	Summary	19
Chapter 3	Modelling Framework	21
3.1	Thermal-Chemical-Mechanical Analysis	22
3.1.1	Thermal-Chemical Analysis	22
3.1.1.1	Governing Equation	22
3.1.1.2	Boundary Conditions	24
3.1.1.3	Cure-kinetics Models	25
3.1.2	Mechanical Analysis	27
3.1.2.1	Stiffness Matrix	27
3.1.2.2	Micromechanics Model	28
3.1.3	Resin Property Modelling	31
3.1.3.1	Linear Elastic Model	31
3.1.3.2	CHILE Model	31
3.2	Effective Laminate Distortion using CLT	34
3.2.1	Classic Laminate Theory	34
3.2.2	Process-Induced Strains	38
3.2.3	Effective Laminate Residual Stresses	41
3.3	Material Characterisations	42
3.3.1	Cure-Kinetic Properties of the Resin	42
3.3.2	DoC-dependent Mechanical Properties	44
3.3.3	Thermal-Chemical Shrinkage	45
3.4	Summary	48
Chapter 4	1D Modelling of Residual Stresses in Laminates	49
4.1	Overview	49
4.2	Numerical Implementation in Matlab	50
4.2.1	Forward Euler Discretisation Method	50
4.2.2	Computational Framework	51
4.3	Framework Verification	52

4.3.1	Model Description	52
4.3.2	Resin Modulus and Chemical Shrinkage	54
4.3.3	Temperature and DoC Evolution	55
4.3.4	Thickness Effect on Residual Stresses	56
4.3.5	Cure Cycle Effect on Residual Stresses	58
4.4	1D Modelling of IM7/8552 Laminates	59
4.4.1	Material Properties of IM7/8552 Laminates	59
4.4.2	Boundary Conditions	60
4.4.3	Residual Stresses of IM7/8552 Laminates	61
4.5	Summary	63
Chapter 5	3D Modelling of Spring-in in Curved Laminates	65
5.1	Overview	65
5.2	Numerical Implementation in ABAQUS	66
5.3	3D Modelling of Curved Laminates	69
5.3.1	Model Description	69
5.3.2	Boundary Conditions	71
5.3.3	Temperature and DoC Distribution Prediction	72
5.3.4	Residual Stresses Prediction	74
5.3.5	Spring-in Predictions	75
5.4	Investigation of Geometry Effect on Spring-in	78
5.5	Investigation of Shear-lag Effect on Spring-in	81
5.6	Summary	83
Chapter 6	Investigation on Spring-in of L-shaped Laminates	85
6.1	Overview	85
6.2	Experimental Investigation on Factors Contributing to Spring-in . . .	86
6.2.1	Tool Preparation	86
6.2.2	Prepregs Description	87
6.2.3	Manufacturing Procedures	87

6.2.4	Autoclave Cure Process	87
6.2.5	Manufacturing of Specimens	90
6.2.6	Measurement of Spring-in	92
6.2.7	Measurement of Warpage	94
6.2.7.1	Warpage in flat specimens	94
6.2.7.2	Warpage in the flange part of L-shaped specimens	96
6.2.8	Experimental Uncertainties	98
6.3	Semi-empirical Investigation on Tool-Part Shear Interaction	99
6.3.1	Analytical Prediction of Tool-Part Interaction Effect	99
6.3.2	Numerical Prediction of Tool-Part Interaction Effect	102
6.4	Numerical Investigation on Factors Contributing to Spring-in	106
6.4.1	Model Description	106
6.4.2	Definition of 'Spring-in' angle	108
6.4.3	Comparison of Numerical and Experimental Results	108
6.4.4	Sensitivity Analysis on Tool-part Shear	112
6.5	Summary	113
Chapter 7	Investigation on Distortions of Tapered Laminates	114
7.1	Overview	114
7.2	Design Guidelines	115
7.3	Modelling of Laminates with Ply-drops	116
7.3.1	Microscopy of Ply-drop Regions	116
7.3.2	Model Description	117
7.4	Investigation on the Influence of Ply-drops	118
7.4.1	Laminates without Ply-drops	118
7.4.2	Laminates with Ply-drops	120
7.4.3	Effect of Dropped Ply Orientations	123
7.4.4	Effect of Number of Dropped Plies	125
7.4.5	Effect of Ply-drop Strategies	127

7.4.6	Effect of Resin Pocket Ratio	133
7.5	Summary	133
Chapter 8	Conclusions and Future Works	135
8.1	Concluding Remarks	137
8.2	Future Works	138
Bibliography		140

List of Tables

1.1	Factors contributing to distortion	4
2.1	Resin states during cure process	9
3.1	Phenomenological cure kinetics models	26
3.2	Parameters used for 8552 resin modulus development using CHILE model (Johnston, 1997)	33
3.3	Value of constants in Eq.(3.80)	43
3.4	Constants for 8552 cure kinetics model (Ersoy et al., 2005a)	43
3.5	Material properties of AS4/3501-6 prepregs (White and Kim, 1998) .	44
3.6	Mechanical properties of AS4 fibre and 8552 uncured and cured resin (Ersoy et al., 2010a)	45
3.7	Effective mechanical properties of AS4/8552 unidirectional laminates using SCFM and FEBM	45
3.8	CTE and CCS of fully cured AS4/3501-6 prepregs in principle directions	46
3.9	Thermal and chemical shrinkage measurements for unidirectional and cross-ply AS4/8552 prepregs	47
3.10	CTE and CCS measurements of M21/IMA prepregs	48
4.1	Material properties of E-glass fibre and polyester resin	53
4.2	Cure kinetics parameters	54
4.3	Constants for 8552 cure kinetics model (Ersoy et al., 2005a)	59
4.4	Thermal properties of UD IM7/8552 laminates (Saad et al., 2014) . .	60

4.5	Effective mechanical properties of IM7/8552 unidirectional laminates using SCFM	60
4.6	Mechanical properties of IM7 fibre and 8552 resin	61
4.7	Thermal and chemical shrinkage for IM7/8552 laminates (Ratcliffe et al., 2013)	61
5.1	Constants for 8552 cure kinetics model (Ersoy et al., 2005a)	70
5.2	Effective mechanical properties of AS4/8552 unidirectional laminates using SCFM	71
5.3	Thermal and chemical shrinkage for unidirectional AS4/8552 prepregs	71
5.4	Comparison of the modelling and experimental results of the spring-in angle for UD laminated curved part	75
5.5	Comparison of the modelling and experimental results of the spring-in angle for cross-ply laminated curved part	76
5.6	Parametric analysis of different factors contributing to spring-in	78
5.7	Arc-to-thickness ratio effect on spring-in angle	80
5.8	Parametric analysis of shear-lag effect on spring-in	82
6.1	Configuration of L-shaped specimens	90
6.2	The evaluation of the plane fitting quality	94
6.3	Angle profile of tools with different corner radius	94
6.4	Measured spring-in angle of the L-shaped specimens	95
6.5	Warpage of the flat specimens	96
6.6	Measured thickness at flange and corner of the specimens	98
6.7	Equivalent tool-part interface shear of the flat specimens	103
7.1	Comparison between experimental and numerically predicted warpage for two specimen configurations	122
7.2	Experimental measurement and numerical prediction of the maximum warpage in 5to4 ply-drop specimens	125

7.3 Experimental measurement and numerical prediction of the maximum warpage in specimens dropping single and double [0°] plies 127

7.4 Experimental measurement and numerical prediction of the maximum warpage in three specimens 132

List of Figures

1.1	Autoclave in the composites manufacturing laboratory at University of Nottingham	2
1.2	Illustration of (a) spring-in and (b) warpage distortions	3
1.3	Mechanism of spring-in phenomenon	4
3.1	The modulus development of 8552 resin as a function of (a) DoC and (b) temperature using the CHILE approach	33
4.1	Schematic of the unidirectional-reinforced laminate	53
4.2	Prediction of the (a) resin modulus and (b) chemical shrinkage under an isothermal cure at 100°C	55
4.3	(a) The temperature and (b) the curing evolution under the autoclave cure cycle for the laminates with 25.4 mm thickness	55
4.4	The through-thickness distribution of (a) the temperature and (b) the DoC in the laminate at curing time=164 mins	56
4.5	The transverse residual stresses distribution from (a) the Matlab model prediction and from (b) Bogetti and Gillespie Jr (1992)	57
4.6	Residual stresses distribution of the 25.4 mm thick laminates under heating-up ramps of 0.25, 0.5 and 1.0°C/minute	58
4.7	(a) Temperature and (b) DoC evolution at the centre and the surface of the laminates under MRCC	62
4.8	The transverse residual stresses distributions of thick and thin laminates	63

5.1	Computation flowchart for sequentially coupled thermal-chemical-mechanical analysis in ABAQUS	67
5.2	Modelling framework including user-subroutines	68
5.3	Framework of thermal-chemical analysis with user-subroutines USD-FLD and HETVAL	69
5.4	The geometry description of the curved part	70
5.5	Boundary conditions for the two-step analysis of the curved part (Ersoy et al., 2010b)	72
5.6	DoC and temperature evolution of resin 8552 under MRCC	73
5.7	Transverse in-plane stress distribution through thickness of (a) UD and (b) cross-ply laminated C-section	74
5.8	Spring-in deformation for UD laminated curved part with various thickness (unit=m, scale factor=8)	76
5.9	Spring-in deformation for cross-ply laminated curved part with various thickness (unit=m, scale factor=8)	77
5.10	Spring-in deformation for cross-ply laminated curved part with various tool radius (unit=m, scale factor=8)	79
5.11	Arc-to-thickness ratio versus spring-in angle	80
5.12	Shear-lag at resin vitrification point	81
5.13	Shear-lag angle versus spring-in angle of the curved part	83
6.1	Aluminium tools with 0.25/0.5/1.0 inch radius at the curvature . . .	86
6.2	Experimental procedure of preparing L-shaped specimen from step (a) to step (d)	88
6.3	Monitored and target autoclave cure cycles	89
6.4	All the L-shaped specimens manufactured in this work	91
6.5	L-shaped specimens with varying (a) thickness (b) radius (c) flange length	91
6.6	All the flat specimens manufactured in this work	92

6.7	Measurements of L-shaped specimen using Creaform 3D HandySCAN	93
6.8	Measurements of enclosed angle in GOM Inspect with fitting planes in transparent red and scanned image in grey	93
6.9	Measurements of a flat specimen using Creaform 3D HandySCAN . . .	95
6.10	Warpage of the specimens with 240 mm flange length	96
6.11	Warpage of the flat specimens from batch 1 and batch 2	97
6.12	Warpage in the flange part of the L-shaped specimens	97
6.13	Force diagram of tool-part interaction	100
6.14	Model geometry and boundary conditions of the flat laminates	103
6.15	Relationship between the specimen length and its corresponding tool- part shear stress τ_s	104
6.16	Edge effect of tool-part shear stress τ	104
6.17	Determining shear term τ_s	105
6.18	Geometry and boundary conditions for the two-step analysis of the L-shaped laminates	107
6.19	Boundary conditions for tool-part interaction analysis of the L-shaped laminates	107
6.20	Definition of 'Spring-in' angle in numerical prediction	108
6.21	Experimental and numerical results for spring-in angle of L-shaped specimen with varying number of ply	109
6.22	Arc-to-thickness ratio versus spring-in angle	110
6.23	Experimental and numerical results for spring-in angle of L-shaped specimen with varying corner radius	111
6.24	Experimental and numerical results for spring-in angle of L-shaped specimen with varying flange length	111
6.25	TPI-induced spring-in angle for the labelled specimen configurations with varied geometric parameters	112

7.1	The resin-rich area and entrapped voids at ply drop-offs regions of UD laminates	117
7.2	Boundary conditions for the (a) autoclave cure (b) load release and (c) TPI analyses steps in ABAQUS modelling	118
7.3	Distortion of specimens without any ply drops	119
7.4	Determining tool-part shear stress through curve fitting to the experimental data	120
7.5	Design configuration of ply-drop from QI laminates to UD laminates .	120
7.6	Warpage measurement of a (a) 4-to-2 ply-drop and (b) a 8-to-4 ply-drop specimens from a top view	121
7.7	Experimental warpage along width direction at the drop-off zone . . .	121
7.8	Distortion prediction of the (a) 4-to-2 ply and (b) 8-to-4 ply laminates (unit = m)	122
7.9	Design configuration of specimens with dropped ply of (a) [0] orientation and (b) [90] orientation	123
7.10	Distortion of specimens dropping (a) [0]-oriented ply and (b) [90]-oriented ply (batch 1)	124
7.11	Distortion of specimens dropping (a) [0]-oriented ply and (b) [90]-oriented ply (batch 2)	124
7.12	Design configuration of specimens dropping (a) single [0°]-oriented ply and (b) double [0°]-oriented plies	125
7.13	Experimental distortion of specimens dropping (a) single [0°]-oriented ply and (b) double [0°]-oriented plies	126
7.14	Design configuration of specimens with (a) 1 drop-off (b) 2 drop-offs and (c) 4 drop-offs	128
7.15	Experimental distortions of three specimens (batch 1)	129
7.16	Warpage of specimens (a) along length and (b) along width at drop-off region (batch 1)	129

7.17 Experimental distortions of three specimens (batch 2) 130

7.18 Warpage of specimens (a) along length and (b) along width at drop-off
region (batch2) 130

7.19 Distortion prediction of specimens with (a) 1 drop-off (b) 2 drop-offs
and (c) 4 drop-offs without tool-part interaction effect (unit = m) . . 131

Chapter 1

Introduction

1.1 Background

The last few decades has witnessed the increasing application of composites in sectors including high performance vehicles, commercial aircraft, wind energy and etc. The manufacturing of composites involves the manipulation of two or more dissimilar materials into a designated structure, to achieve a new set of characteristics that none of the constituent materials could achieve on their own. The fabrication of composites in aerospace applications requires high dimensional fidelity from an assembly perspective. The increased demand for complex geometries has pushed the limit for designing a manufacturing procedure that is capable of delivering high-performance structural and non-structural components.

Composite materials are subjected to the distortions originated from anisotropic behaviours in material properties. These non-uniform material characteristics introduce variations in the micro and macro structural behaviours, hence, should be fully understood and accounted for at the design stage.

In the engineering practice, experience provides an initial guess for the control pa-

rameters and the cost of trials could vary significantly. Numerical tools provide an insight on the thermo-chemical and mechanical behaviour of the material, indicating the compensation to be adapted in the design of the tool. While engineers are seeking to optimise the manufacturing process, a suitable simulation tool would reduce costly iterative design-prototyping-testing process.

1.2 Autoclave Process

Autoclave processing commonly refers to the manufacturing of thermoset composites made of prepreg material. This process remains today the benchmark for high-performance structural components within the aerospace or defence industries (Hubert, 2023). What distinguishes the autoclave process is its capability to provide pressurised gases, enabling compaction pressures to reach 7 bar. This feature ensures high laminate quality and performance with assured repeatability. The autoclave used in this research is shown in Figure 1.1.



Figure 1.1: Autoclave in the composites manufacturing laboratory at University of Nottingham

1.3 Process-induced Distortions

While autoclaved laminates offer great flexibility in achieving purpose-oriented performance through optimised lay-up sequences, the inevitable cost of such freedom is process-induced distortions (PIDs) that arise during manufacturing. Identifying the contributing factors to the PIDs or residual stresses has long been the key motivation in the aerospace and other industries. Typical examples of distortions in the angled and flat laminates are illustrated in Figure 1.2.

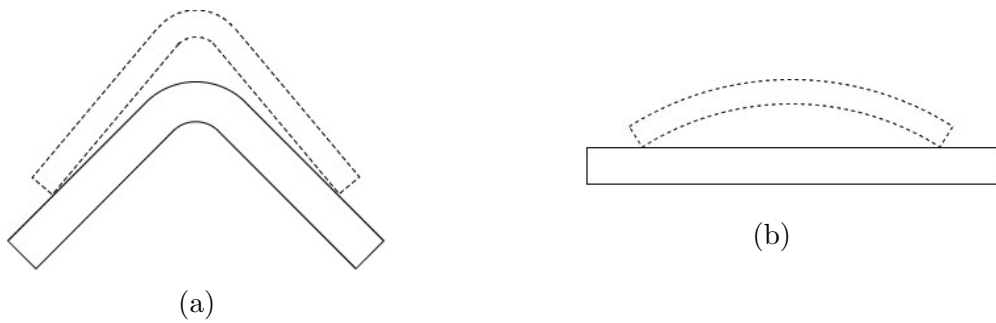


Figure 1.2: Illustration of (a) spring-in and (b) warpage distortions

In the manufacturing of a curved composite structure, the enclosed angle tends to reduce after demoulding. This phenomenon is referred as 'spring-in'. By nature fibre reinforced laminates exhibit anisotropic behaviour due to the significant differences between the coefficient of thermal expansion (CTE) in fibre direction and that in off-axis directions. During the cooling-down phase, thermal contraction occurs, contributing to the reduction in the enclosed angle. In a similar manner, prior to cooling down, resin shrinkage takes place, since resin is more dominant in the through-thickness direction compared with that in fibre direction, more shrinkage occurs in resin-rich areas. Figure 1.3 shows a comparison of isotropic and anisotropic shrinkage, as an illustration of spring-in mechanism.

Another form of distortion is referred as warpage, commonly observed in flat components when demoulded. As per industry standard, prepregs are symmetrically laminated to achieve quasi-static equilibrium, in rare case of asymmetrical lamina-

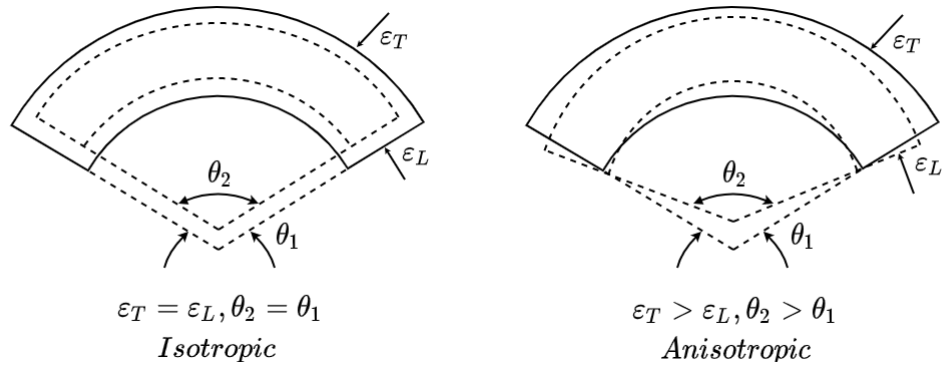


Figure 1.3: Mechanism of spring-in phenomenon

tion, warpage would be expected. Other case of inducing warpage is contributed from the CTE difference of the laminates and that of the mould. Typically an aluminium or steel tool would have larger CTE compared with laminated composites, causing friction at the interface. In real life scenario, distortions are often seen in a combined form of spring-in and warpage.

In the extensive literature, the origins of distortions are commonly distinguished into two categories, namely the intrinsic and extrinsic sources. The intrinsic sources of residual stresses are related to the geometric features and the inherent nature of composites, where the chemical and thermal shrinkage had a direct impact on the end product. In contrast, the extrinsic sources are related to the manufacturing conditions such as tool-part interaction and autoclave cure cycle control. A summary of the factors contributing to the residual stresses are presented in Table 1.1.

	Intrinsic	Extrinsic
Geometrical features	Material Anisotropy	Processing condition
Thickness	Thermal contraction	Tool-part interaction
Radius	Resin shrinkage	Cure temperature
Lay-ups	Fibre volume fraction	Cure pressure

Table 1.1: Factors contributing to distortion

1.4 Research Objectives

The primary objective is to develop and validate a predictive model for PIDs in composite structures, with particular emphasis on TPI effects that remains to be one of the major challenges to conquer in the relevant industries. This work built upon a sequentially coupled thermal-chemical and mechanical model using ABAQUS, the cure-kinetics model and material constitutive model are incorporated into user subroutines. The accuracy of the predictive model was measured by comparing predicted distortion against experimental data from specimens manufactured using IM7/8552 UD prepregs. This work aims to address the industry need for precise prediction of PID during composite manufacturing, aiming to optimise manufacturing processes and enhance the dimensional accuracy of produced composite parts.

1.5 Thesis Outline

This thesis unfolds as follows:

- Chapter 2: Provides a detailed discussion on the mechanisms of distortion, presenting a literature review on current studies focusing on factors contributing to PIDs, with a particular interest on the tool-part interaction effect.
- Chapter 3: Introduces the methodology, delineating the thermal-chemical-mechanical analysis framework. The Cure Hardening Instantaneously Linear Elastic (CHILE) constitutive model is introduced, and material characterisation for resin system 8552-based composite materials is discussed.
- Chapter 4: Presents a Classic Laminate Theory (CLT)-based numerical model that demonstrates the aforementioned methodology and discusses the distribution of residual stresses across a thick laminate.
- Chapter 5: Introduces a 3D modelling framework implemented in ABAQUS

assisted by user-subroutines. The relationship between the spring-in angle and the part geometric features is thoroughly discussed.

- Chapter 6: Introduces a novel Tool-Part Interaction (TPI) model added to the established framework to predict PIDs in L-shaped specimens. The validity of the developed model was again evaluated by the comparison to numerical prediction to the experimental findings.
- Chapter 7: Applies the established model to tapered laminates and evaluates its applicability and limitations.
- Chapter 8: Concluding the work.

Chapter 2

Literature Review

2.1 Introduction

This chapter began with a section of discussion on the mechanisms of PIDs. In this section, the author explored the topic from three perspectives, namely, the thermal, chemo-rheological and tool-part interaction effects on the formation of distortions. Following on that, the study presented a thorough literature review on analytical and numerical models of predicting PIDs. In particular, the author looked into the current studies on addressing tool-part interaction impact on PIDs. Lastly, the studies on ply-drops effects were presented.

2.2 Mechanisms of Distortion

2.2.1 Thermal Effect

The stress built-up due to the thermal expansion effects can be categorised into micro- and macro- scales. The micro-mechanical stresses exhibited within a lamina, i.e. between the fibre reinforcement and the host matrix, develop from the mismatch of thermal expansion coefficients between the fibre and the resin (Parlevliet et al.,

2007). Such stress development is more severe in the cooling phase during autoclave cure cycle (Zhao et al., 2006). The thermal expansion mismatch could initialise micro-cracking as resin contracts. Some studies (Wisnom et al., 2006) argue that micro-mechanical stresses are in self-equilibrium and do not cause large deformation, hence are generally neglected. However, residual stresses in the macro scale need to be carefully handled as they are originated from the global anisotropic behaviours, i.e. in-plane and out-of-plane variations in thermal expansion capacity. As has been mentioned in section 1.3, for a curved section, the CTE difference between the thickness direction and the circumferential direction results in a reduction in the enclosed angle of an L-shaped part, known as spring-in. Nelson and Cairns (1989) proposed the first estimation on the spring-in angle $\Delta\theta$, given by

$$\Delta\theta = \theta \frac{(\alpha_I - \alpha_T)\Delta T}{1 + \alpha_T\Delta T} \quad (2.1)$$

where θ is the included angle of the part, α_I is the circumferential coefficient of thermal expansion, α_T is the radial coefficient of thermal expansion and ΔT is the temperature difference. Eq.(2.1) formed the theoretical basis of many studies investigating the thermo-elastic contribution to the spring-in phenomenon (Johnston et al., 2001; Darrow Jr and Smith, 2002; Radford and Rennick, 2000).

In the through-thickness direction, variation in the CTE can still happen, mainly due to the gradient in fibre volume fraction (V_f). Due to the imperfection in processing when autoclave pressure or vacuum pressure are applied, the resin rich region generally forms near the tooling exhibiting higher CTE and the resin poor region forms near the vacuum bag exhibiting lower CTE. Such CTE gradient is also a source of warpage (Naji and Hoa, 1999).

2.2.2 Chemo-rheological Effect

The curing process of a thermoset resin is commonly distinguished into three phases, as summarised in Table 2.1. Prior to gelation, resin is uncured and behaves like viscous liquid. Once the resin reaches the onset of gelation, phase transition occurs from a viscous liquid state to a rubbery state exhibiting viscoelastic behaviour. Later on as the cure temperature reaches the glass transition temperature T_g , resin goes through a rubbery-to-glassy state transition, exhibiting elastic-solid behaviour, known as vitrification. Hence, the point of gelation, often denoted as the degree of cure at gelation (α_{gel}) and the glass transition temperature (T_g) are two critical properties in the chemo-rheological characterisation of resins.

Viscous-fluid State	Rubbery State	Glassy State
Low shear modulus, resin behaves as viscous fluid	Resin behaves as viscous elastic material	High shear modulus, resin behaves as elastic material
Part cannot sustain any stresses	Dominated by chemical shrinkage	Dominated by thermal contraction
No stresses contributing to spring-in	Shear lag and in-plane stresses are generated	In-plane stresses are generated

Table 2.1: Resin states during cure process

During the curing process, the monomer molecules go through chain formation and linearly grow through branching. Cross-linking then begins between the molecular chains to form a rigid 3D network. This process is irreversible and exothermic due to the reduction in the degrees of freedom to store thermal energy. Consequently, chemical hardening occurs through the stiffness development and chemical shrinkage is observed through the volumetric change of the system. The coefficient of thermal expansion of the resin decrease during vitrification, i.e. resin exhibits larger CTE in its rubbery state compared to that in its solid state.

The DoC at the gel point (α_{gel}) plays an important role in determining the chemical shrinkage of a resin. Various methods exist for determining α_{gel} as well as measuring

the volumetric shrinkage of the resin, such as dynamic mechanical analysis (DMA) or thermo mechanical analysis (TMA). It is commonly believed that resin exhibits a good viscous-liquid behaviour prior to the gelation, hence stress can not be built-up within the resin system (Ersoy et al., 2010b). The contribution of any resin shrinkage along with counter-effect from thermal expansion will only be taken into consideration after resin passing the DoC at the onset of gelation. Some studies further argued that load transfer between fibres and matrix is effective after the onset of gelation (Russell et al., 2000; Mulle et al., 2009). Since the onset of gelation varies at different degree of cure for different resin matrix system, the magnitude of chemical shrinkage contributing to the stress development varies. For instance, unsaturated polyester resins are known to gel earlier than epoxy resins (Kenny et al., 1989, 1990). Hence it is often found in the literature that the specific total volumetric shrinkage of epoxy is smaller than that of unsaturated polyester (Shah and Schubel, 2010).

The glass transition temperature (T_g) denotes a temperature range over which the mobility of the molecular chains changes significantly, e.g. resin transition from rubbery to solid state. The ultimate T_g is determined by many factors including the resin structure, the type of hardener and the degree of cure. Since the mechanical properties of the resin are highly sensitive to its rubbery-to-glassy transition, T_g should be carefully determined (Khoun et al., 2010). T_g is commonly measured by a step change in the heat flow from a Differential Scanning Calorimetry (DSC) test. Alternative methods such as TMA are also widely used. The evolution of T_g can be modelled using DiBenedetto equation (Khoun, 2009) correlated to the degree-of-cure (α), given by

$$\frac{T_g - T_g^0}{T_g^\infty - T_g^0} = \frac{\lambda\alpha}{1 - (1 - \lambda)\alpha}, \quad (2.2)$$

where T_g^0 and T_g^∞ are the glass transition temperatures of uncured and fully cured resin, and λ is a constant valued between 0 and 1.

2.2.3 Tool-Part Interaction Effect

It is a common observation that symmetrical and balanced laminates fabricated on a flat tool exhibit warpage after demoulding. Such deformation is the result of the CTE mismatch between tool and part. In most cases, this mechanism is invoked when a laminate with low CTE manufactured using a tool with a significantly higher CTE, such as aluminium and steel.

During an autoclave process, both tool and part are going through temperature ramps subjected to autoclave pressure, ensuring a close contact between the surfaces of the tool and the part. Prior to gelation, stresses build up primarily due to the friction between fibres and the tool surface (Wisnom et al., 2006). After gelation, the laminate is stretched due to tool expansion under elevated temperature. Layers close to the tool surface are exposed to higher strains than those further away, generating stress gradient through the thickness of the laminates. After the resin is cured, such stress gradient is locked in, and referred to as the residual stress due to TPI. When the part is demoulded from the tool, such residual stresses are released through a concave down warpage. The warpage deformation is associated with many factors, including tool material, tool surface finish, autoclave pressure, part thickness and length, the contribution of each factor varies from case to case, which are difficult to isolate.

Current manufacturing of high-performance composites uses Invar36 tool mainly due to its uniquely low coefficient of thermal expansion. Its CTE of $1.2E-6$ ($1/^\circ\text{C}$) at $20\text{-}100^\circ\text{C}$ is comparable to the CTEs of typical CFRP laminates (Kappel, 2016). However, the cost of Invar is more than 30 times the cost of steel or aluminium, which motivates the researcher to find an alternative. The use of aluminium or steel tools offers a substantial cost saving compared to Invar tools, though under the risk of possible distortion after the process. Therefore, understanding the mechanism of TPI provides a meaningful guideline to the relevant industries.

2.3 Current Studies on Predicting PIDs

Having explored the mechanisms of three major factors contributing to PIDs, it is important to establish the modelling procedures that accurately capture the chemical, thermal and TPI effects. In this section, analytical and numerical methods of predicting PIDs were discussed.

2.3.1 Analytical Model of Predicting PIDs

Analytical prediction can provide a good initial estimation of the magnitude of 'spring-in' or 'warpage', with less input data requirement, which is of great benefit to the early stage of manufacturing tool. It provides an initiative insight into the distortion mechanism, as well as acts as an auxiliary tool to the numerical solution. As previously mentioned in Section 2.2.1, Nelson and Cairns (1989) proposed the spring-in angle of a curved part with orthographic thermal properties, shown in Eq.(2.1). Radford and Diefendorf (1993) expanded the equation by introducing an additional term representing non-thermal component of spring-in angle, shown below. Their work highlighted the coefficient of thermal expansion and the temperature change can be substituted with other factors that accounting for manufacturing and more complex environmental effects.

$$\Delta\theta = \theta \frac{(\alpha_I - \alpha_T)\Delta T}{1 + \alpha_T\Delta T} + \theta \frac{\Phi_I - \Phi_T}{1 + \Phi_T} \quad (2.3)$$

where, Φ_I is the in-plane fabrication expansion and Φ_T is the through-thickness fabrication expansion.

Following the pioneering studies by Nelson and Cairns (1989) and Radford and Diefendorf (1993), numerous researchers have dedicated their efforts to enhancing Eq.(2.3), aiming for a more comprehensive analytical prediction of distortion. For instance, Wisnom et al. (2007) extended Radford's equation by introducing a novel

analytical approach based on shear-lag theory. This method accounted for thermal and chemical shrinkage occurring between gelation and vitrification. Building upon Wisnom's work, Ding et al. (2019) further expanded the analytical prediction to include the influence of flange warpage and its contribution to spring-in.

2.3.2 Numerical models of Predicting PIDs

The predicting of PIDs through numerical approaches were extensively investigated in the literature. An accurate model of PIDs requires a constitutive material model that best describes the effective mechanical and thermal properties of the composite material at each time increment of a cure cycle. A review on the material models of composite manufacturing process was conducted by Baran et al. (2017) and Wang et al. (2023). Such material models can be categorised into three types, namely, linear elastic models, viscoelastic models, and path-dependent models.

The linear elastic model proposed by Bogetti and Gillespie Jr (1992) assumed that the resin modulus is a function of the DoC. Their model does not include the temperature dependency of the resin. A modified elastic model proposed by Johnston et al. (2001) further improved Bogetti's model by proposing a Cure Hardening Instantaneous Linear Elastic (CHILE) model. Johnston et al. (2001) presented experimental findings of the relationship between DoC and the modulus of the resin that were isothermally cured at different temperatures. Their study found that the modulus of the resin is the function of both DoC and the temperature. The CHILE model has been extensively used and modified in many research (Moretti et al., 2020; Traiforos et al., 2021; Dai et al., 2019; Liu et al., 2021).

However, elastic models cannot demonstrate stress relaxation. Zocher et al. (1997) proposed a viscoelastic model which accurately described the viscoelastic behaviour of resin. The model is able to capture time-dependent properties of the resin. The cure dependent relaxation modulus of an epoxy resin was experimentally investi-

gated over the range of DoC by O'Brien et al. (2001). To fit experimental data, a Maxwell model which consists a number of spring-damper elements in series is a common choice to simulate the viscoelastic behaviour of resin. However, a single Maxwell model cannot accurately describe the stress relaxation phenomenon. Therefore, a generalised Maxwell model is typically used, which can be expressed in the Prony series form (Wang et al., 2023). Such model requires resin relaxation characterisation, i.e. to obtain the weight fitting factors and their corresponding relaxation time at different DoC. When compared to an elastic model, the additional memory resources needed for the allocation of internal state variables at each integration point also make this model computationally heavy to run. Despite the drawbacks, this model is so far the best approach given all required material data are available. This model has also been employed in many studies to predict PIDs (Ding et al., 2015; Chen and Zhang, 2019; Trofimov et al., 2021).

To simplify the viscoelastic modelling approach, Svanberg and Holmberg (2004) proposed a path-dependent model, in which it assumes that resin is completely relaxed in the rubbery state and no stress relaxation occurs in the glassy state. Svanberg et al. (2005) applied the model in predicting PIDs of curved composite C-spar. Ding et al. (2016b) employed the path-dependent model to predict PIDs in L-shaped composite structures.

The performances of different material model were also compared in the literature. Ding et al. (2016a) compared the accuracy of predicting spring-in angle of a C-shaped composite part, using viscoelastic model, path-dependent and CHILE model. Their work reported that there is insignificant difference in the results produced by the aforementioned constitutive models, when compared to the experimental results presented by Ersoy et al. (2010b). The viscoelastic model and the CHILE model both underestimated the spring-in angle of the UD parts. Zobeiry et al. (2010) evaluated the predicted residual stresses in thermoset polymer composites using pseudo-

viscoelastic and viscoelastic models. The pseudo-viscoelastic model is essentially a calibrated CHILE model where the modulus was defined as being the viscoelastic relaxation modulus at a specific time. Their work demonstrated that from a full viscoelastic model to the simplest CHILE model, the accuracy of the prediction is traded off for lower material characterisation cost and less run time. They also highlighted that when properly calibrated, the pseudo-viscoelastic approach is as valid as a fully viscoelastic approach. Dai et al. (2019) also compared the residual stress and distortion in thermosetting composites using a modified CHILE model and a viscoelastic model. Their work reported although the modified CHILE model has a lower accuracy than the viscoelastic model, the modified CHILE model was proved to be far more efficient. Within the margin of error, the viscoelastic model can be replaced by the modified CHILE model. Traiforos et al. (2023) compared the performance of these two constitutive models in predicting spring-in angle of L-shaped specimens. The predicted spring-in angle difference using viscoelastic model and CHILE model is insignificant when compared to the scattered data that were experimentally measured. It can be observed that both CHILE and viscoelastic model performs in the same trends but overall the spring-in angle predicted by CHILE model is higher than that by viscoelastic model. Traiforos et al. (2021) also compared the PIDs prediction of an aerospace composite frame by employing viscoelastic model and CHILE model. The study presented the deviation between the measured distortions and the predicted ones using viscoelastic model and CHILE model. It was found that both model produced very similar results while the distortion predicted by the viscoelastic model is more accurate.

Overall, as an alternative to viscoelastic model, CHILE model demonstrated a good accuracy with its advantage in low material characterisation cost and improved computational efficient. Therefore, in this work, CHILE model will be adopted in the material constitutive modelling framework.

2.4 Factors Contributing to PIDs

Extensive literature looked into different factors contributing to PIDs, through experimental, analytical or numerical approaches, with the objective to isolate each factor and evaluate their influence towards the final distortion. However, the conclusions driven from various studies are rather contradicting, leaving quite a room of discussion on this topic.

Albert and Fernlund (2002) were the first to point out the importance of spring-in measurement to be distinguished into two components: a corner component and a flange/web warpage component. Their work concluded the corner component of spring-in was primarily the product of thermal and cure shrinkage. The warpage component of spring-in was dominated by both extrinsic factors, including tool material, tool surface condition, cure cycle, and intrinsic factors, such as thickness and flange length. However, the effect of lay-up sequence and part angle were unclear. Svanberg and Holmberg (2001) demonstrated the cure cycle effects on spring-in angles. Darrow Jr and Smith (2002) found the tool radius had little effect on spring-in, while the through-thickness shrinkage, volume fraction gradient and tool material all contributed to spring-in. Fernlund et al. (2002) studied the effect of cure cycle, tool surface, specimen geometry and lay-ups on the dimensional fidelity of laminated part. They reported a U-shaped part exhibits 30% more spring-in than an L-shaped part due to the ‘geometric locking’ of the part on the tool. Kappel et al. (2013) examined the effect of tooling material, different lay-ups and the thickness. The maximum flange warpage presented from Kappel et al. (2013) was less than 1/10 of that presented from Fernlund et al. (2002), indicating that 50% reduction in flange length of the specimen results in 94% reduction in flange warpage. Therefore, it is recommended to use L-profile specimens with short flanges to minimise the superposition of both ‘spring-in’ and ‘warpage’ effects. Kappel et al. (2013) also reported for UD laminates fabricated on aluminum tool, no thickness dependency

of the spring-in angle was observed. However, for UD laminates fabricated on Invar tool, the spring-in of 8-ply specimen was 23% smaller compared to that of 4-ply specimen. Their study also found that the spring-in of specimens with different quasi-isotropic lay-ups were almost identical. The results presented by Takagaki et al. (2017) agrees well with the findings from Fernlund et al. (2002), where larger warpage and spring-in were generated in U-shaped specimens compared with that in L-shaped specimens. Their study further demonstrated that shear deformation was suppressed as thickness decreased and the flange length increased, through fibre-optic monitoring method.

To summarise, although many studies explored different methods to accurately predict the spring-in and warpage distortions, there are still areas that remains today not fully understood. One particular case is the tool-part interaction effect on PIDs. In the following section, analytical and numerical modellings of TPI effects will be discussed. Furthermore, many researchers investigated the spring-in or warpage of specimens with simple geometries, few studies demonstrated the validity of the modelling approach on predicting PIDs of composite structures with ply-drops. Therefore, the current studies on ply-drop effect will also be reviewed.

2.4.1 Current Studies on TPI Effects on PIDs

Many researcher investigated the TPIS effect on PIDs through numerical approaches. Twigg et al. (2004b) incorporated an elastic shear layer into the modelling, to permit the transfer of shear stresses between the tool and the part. Their work demonstrated the values of shear layer modulus and initial resin modulus play a crucial part in accurate modelling of TPI effect. Kaushik and Raghavan (2010) quantified the TPI by measuring the static and dynamic frictional coefficient between tool and prepregs, subjected to temperature and degree-of-cure changes. Their approach demonstrated a successful implementation in predicting distortions in a large aerodynamic struc-

ture (Zeng and Raghavan, 2010). In their work, the TPI during the processing was modelled using contact elements. The cure-dependent frictional coefficient was experimentally determined. Qiao and Yao (2020) extended the path-dependent material model to include TPI effect. A shear layer was modelled between the tool and the part. Ding et al. (2022) experimentally evaluated critical interfacial shear stresses in sticking condition and in sliding condition, the corresponding friction coefficient were input into the numerical model. Xiao et al. (2023) also presented a simulation work considering state-dependent tangential friction contact. At three resin stages, namely, viscous, rubbery and glassy states, different values of static and sliding coefficient of frictions were assigned to the tool-part interface.

Compared with numerical modelling of TPIs, fewer studies investigated the analytical model of quantifying TPI-induced distortions. Twigg et al. (2004a) proposed a simple analytical model illustrating the relationship between part aspect ratio and the part maximum warpage. Twigg et al. (2003) has also characterised the interfacial shear stress between the tool and the part during the autoclave process by using strain gauges. Their study found that the sliding shear increases significantly with the increase in DoC. To further expand the analytical model proposed by Twigg et al. (2004a), Yuan et al. (2016) included the inter-ply shear stress at each laminate. Their model is capable of predicting through-thickness stresses distribution and warpage due to TPI effect. However, their model did not consider the DoC related property changes. Arafath et al. (2008) derived the analytical expression of through-thickness variation of stresses, taking account of temperature history and DoC-dependent material properties. The distortion in unsymmetrical laminates considering TPI effect was also investigated in Yuan et al. (2018) and Sun et al. (2017).

2.4.2 Current Studies on Ply-drop Effects on PIDs

Tapered composite structures is formed by terminating some plies at designated locations. Such ply discontinuity created sources of PIDs and delamination. Earlier researchers working on tapered composite structures were mostly concerned about the failure mechanisms induced by ply drop-offs, or to seek optimal damage-resistant tapered composite structures by investigating the parameters affecting the structural integrity (He et al., 2000). Different manufacturing process encountered different challenges when producing tapered composite structures. Xin et al. (2011) investigated the resin flow and fibre compaction on tapered laminates. Their work presented the variation in fibre volume fractions of the tapered laminates processed under different bleeder schemes. Peeters et al. (2020) looked into the morphology of ply drops in thermoplastic composite materials manufactured using laser-assisted tape placement with in-situ consolidation. To the best of the author's knowledge, only one paper presented work concerning the PIDs of tapered laminates. Takagaki et al. (2017) performed in-situ strain monitoring and FE modelling of process-induced strains and distortion in curved laminates with ply-drops. Their study found that mechanical coupling between the the thick and thin parts is the major source of non-uniformly distributed residual stresses in longitudinal direction. Overall, studies on ply-drop effects on PIDs are very limited.

2.5 Summary

Although there exists an extensive literature on the topic of this thesis, an accurate prediction of PIDs remains to be a challenging task. Among all the factors contributing to PIDs, one need to identify the major sources, which can then be accurately replicated in the modelling procedure. TPI effect is one of the major sources of introducing PIDs, yet the mechanism of which is not fully understood. One objective of this thesis is to experimentally investigate the TPI effect in relat-

ing to warpage type of distortions. An accurate prediction of TPI could potentially reduce manufacturing costs for industries by enabling the adoption of cheaper tools as alternatives to Invar or composite tools.

The primary aim of this thesis is to develop a predictive modelling framework readily applicable to industries for predicting PIDs in large composite structures. This model should also quantify the contribution percentage of identified sources to the distortions. Additionally, the thesis seeks to experimentally investigate how geometric features such as part thickness, corner radius, flange length, and stacking sequence influence the spring-in angle of L-shaped specimens manufactured using IM7/8552 UD prepregs.

Furthermore, the thesis aims to validate the applicability of the proposed modelling framework to composite structures with ply-drops, particularly to verify the effectiveness of the novel TPI model. Despite the wide application of tapered laminates, the PIDs of which has attracted little attention. A better understanding and an accurate modelling of PIDs occurring at ply-drop zones could facilitate the design of tapered structures and promote the adoption of more cost-efficient design methods.

Chapter 3

Modelling Framework

The autoclave cure process of laminated composites is a multi-physics problem and should be tackled with a coupled modelling approach. The computation of the temperature domain requires thermal analysis, in which the internal heat sources generated by chemical reaction should be treated. The distortion or residual stresses distribution requires one to perform mechanical analysis, where the material properties are temperature-dependent. This chapter summarises the theoretical basis on the sequentially coupled thermal-mechanical modelling approach.

Section 3.1 begins with the governing equation of the fully-coupled thermal-chemical analysis, followed by an introduction of various types of boundary conditions. The internal heat generation requires the quantification of the exothermic chemical reaction of resin, for which purpose a variety of cure kinetics models are explored. Following this, the mechanical analysis requires the formulation of the stiffness matrix. Each stiffness component can be determined using self-consistent field micromechanics model given the temperature-dependent properties of resin and fibre. Furthermore, the material constitutive models is also detailed, describing the stress-strain behaviour of resin. Due to the complexity in characterising the viscous-elastic prop-

erties of the resin, the computational cost and the level of accuracy should be balanced to obtain reliable results. Section 3.2 details the derivation of process-induced strains, illustrated through Classic Laminate Theory. Lastly, Section 3.3 presented the material characterisation including the cure-kinetic properties of the resin, followed by the effective mechanical properties and the thermal-chemical shrinkage of the composite materials.

3.1 Thermal-Chemical-Mechanical Analysis

3.1.1 Thermal-Chemical Analysis

3.1.1.1 Governing Equation

The governing equation of the fully coupled thermal-chemical model requires the understanding of the heat transfer equation, which was derived from Fourier's law and conservation of energy. The Fourier's law, also known as the law of heat conduction, describes the rate of heat transfer through a material is proportional to the negative gradient in the temperature and the area at right angles to that gradient, through which the heat flows (Advani and Sozer, 2002). Such rate of heat transfer, or conduction heat flux, can then be computed from the following:

$$\mathbf{q} = -\mathbf{k} \cdot \nabla T \quad (3.1)$$

where

- \mathbf{q} is the local heat flux density [Wm^{-2}]
- \mathbf{k} is the material's conductivity tensor, [$Wm^{-1}K^{-1}$]
- ∇T is the temperature gradient [Km^{-1}]

A change in internal energy per unit volume in the material, ΔQ , is proportional to the change in temperature, ΔT , expressed as the following:

$$\Delta Q = \rho C_p \Delta T \quad (3.2)$$

where

- ρ is the material density [kgm^{-3}]
- C_p is the specific heat capacity [$Jkg^{-1}K^{-1}$]

Combining Eq.3.1 and Eq.3.2 yields the governing equation, shown in Eq.3.3. The internal thermal energy is justified by introducing an heat generation term \dot{Q}_r , representing the exothermic chemical reaction of resins during the cure process, given in Eq.(3.3).

$$\rho C_p \frac{\partial T}{\partial t} = k_x \frac{\partial^2 T}{\partial x^2} + k_y \frac{\partial^2 T}{\partial y^2} + k_z \frac{\partial^2 T}{\partial z^2} + \dot{Q} \quad (3.3)$$

The internal heat generation per unit volume of the material is expressed by:

$$\dot{Q} = \rho H_T \frac{d\alpha}{dt} \quad (3.4)$$

where

- H_T is the total reaction enthalpy
- α is the degree of cure

The rate of cure term $d\alpha/dt$ can be expressed using various cure kinetics models, detailed in Section 3.1.1.3.

Empirically, the degree of cure α is determined as the ratio of the cumulative heat

generated during polymerization at the time of interest with respect to the total heat generation or reaction enthalpy H_T , given by:

$$\alpha(t) = \frac{H(t)}{H_T} \quad (3.5)$$

The value of H_T for thermosetting resin is commonly measured by a Differential Scanning Calorimetry (DSC) test (Hardis et al., 2013).

3.1.1.2 Boundary Conditions

To capture the temperature distribution across a laminated part, it is crucial to capture precisely the heat transfer at its boundary. In the case of a heat transfer analysis, three boundary conditions are traditionally employed. Each boundary condition has its applicable scenarios, it is up to the researcher to decide which condition is the most appropriate choice. The general form of the boundary condition is expressed as:

$$k_{eff} \frac{\partial T_s}{\partial \hat{n}} + h_{eff} [T_s - T(t)] = 0 \quad T \in \partial\Omega \quad (3.6)$$

where $\partial\Omega$ is the boundary of the domain, T_s is the surface temperature and $\partial T_s / \partial \hat{n}$ is the normal derivative of the surface temperature (Bogetti and Gillespie Jr, 1992). The coefficient k_{eff} and h_{eff} represent the effective thermal conductivity and convection respectively. Adjusting k_{eff} and h_{eff} gives three types of boundary conditions, namely

- Dirichlet (prescribed) boundary condition ($k_{eff} = 0, h_{eff} = 1$)
- Neumann (insulated) boundary condition ($k_{eff} = 1, h_{eff} = 0$)
- Robin (convective) boundary condition

The insulated and prescribed boundary conditions are essentially two limiting cases

of the convective boundary condition. In fact, the thermal convection is the dominant heat transfer mode at laminates surface. The convection coefficient should be experimentally determined (Johnston, 1997).

3.1.1.3 Cure-kinetics Models

There have been many attempts in developing cure kinetic models in the literature, classified into two categories, namely phenomenological models and mechanistic models (Um et al., 2002). Due to the natural complexity of cure reaction, the phenomenological models or empirical models are preferred in the study of cure kinetics. Such models are expressed as the rate of reaction formulated by two separable principal functions, i.e., $k(T)$ and $f(\alpha)$ (Gillham, 1986), so that

$$\frac{d\alpha}{dt} = k(T) \cdot f(\alpha), \quad (3.7)$$

where the conversion function $f(\alpha)$ depends on the chemical reaction of the thermoset resin system. The Arrhenius form rate constant $k(T)$ accounts for the temperature dependency, given as:

$$k(T) = A \cdot \exp \left[\frac{-E_a}{RT} \right], \quad (3.8)$$

where A is a pre-exponential factor, E_a is the activation energy and R is the universal gas constant.

Different types of conversion functions exist, depending on the shape of the heat flow envelope. They are commonly distinguished into a n^{th} order model, an autocatalytic model or a combined form, summarised in Table 3.1.

Eq. (3.11) corresponds to one of the widely used autocatalytic models for an epoxy resin system proposed by Kamal and Sourour (1973), where k_1 and k_2 are derived on the basis of the Arrhenius expression shown in Eq. (3.8). Furthermore, m and n

Cure kinetic models	Equations	
n^{th} order	$k(T) \cdot (1 - \alpha)^n$	(3.9)
autocatalytic	$k(T) \cdot (1 - \alpha)^n \cdot \alpha^m$	(3.10)
n^{th} order autocatalytic	$(k_1 + k_2\alpha^m)(1 - \alpha)^n$	(3.11)

Table 3.1: Phenomenological cure kinetics models

are constants determined by fitting the data obtained from the DSC measurements to the model.

It is worth noting that the heat flow profile in an autocatalytic reaction usually exhibits a bell shape indicating the exothermic curing reaction starts with a curing rate of zero and reaches a peak heat generating point around the middle path. Conversely, a non-autocatalytic models, taking $m = 0$, indicates that the curing rate starts from a peak value at an earlier stage and reaches zero at the end (Um et al., 2002).

The epoxide-amine reaction is a common type of autocatalytic reaction since alcohol is produced as the catalyst, providing the autocatalytic nature of the curing. Sometimes there are cases where the heat flow exhibits more than one dominant reaction during curing, as in the case of the 3501-6 epoxy resin (Kim et al., 2002).

As resin goes through vitrification, the reaction becomes diffusion-controlled. Thus, many studies calibrated Eq. (3.11) to account for the shift from a kinetics-controlled reaction to a diffusion-controlled reaction (Karkanis et al., 1996; Hubert et al., 2001; Garschke et al., 2013; Javdanitehran et al., 2016). A diffusion factor $f_d(\alpha)$ was introduced by Garschke et al. (2013) to improve the performance of the cure

kinetic model at higher degree of curing, expressed as:

$$f_d(\alpha) = \frac{1}{1 + \exp[C(\alpha - \alpha_c)]} \quad (3.12)$$

Thus the complete cure kinetics equation writes as:

$$\frac{d\alpha}{dt} = \frac{(k_1 + k_2\alpha^m)(1 - \alpha)^n}{1 + \exp[C(\alpha - \alpha_c)]} \quad (3.13)$$

where C is a constant and α_c represents the critical degree of conversion at which point the reaction becomes diffusion controlled.

3.1.2 Mechanical Analysis

3.1.2.1 Stiffness Matrix

Understanding a laminated composites structure requires an appreciation of the stiffness or compliance matrix of an orthotropic material. The elasticity equation in full expression (Berthelot and Ling, 1999) is given as the following:

$$\begin{bmatrix} \sigma_1 \\ \sigma_2 \\ \sigma_3 \\ \sigma_4 \\ \sigma_5 \\ \sigma_6 \end{bmatrix} = \begin{bmatrix} C_{11} & C_{12} & C_{13} & 0 & 0 & 0 \\ C_{12} & C_{22} & C_{23} & 0 & 0 & 0 \\ C_{13} & C_{23} & C_{33} & 0 & 0 & 0 \\ 0 & 0 & 0 & C_{44} & 0 & 0 \\ 0 & 0 & 0 & 0 & C_{55} & 0 \\ 0 & 0 & 0 & 0 & 0 & C_{66} \end{bmatrix} \begin{bmatrix} \varepsilon_1 \\ \varepsilon_2 \\ \varepsilon_3 \\ \varepsilon_4 \\ \varepsilon_5 \\ \varepsilon_6 \end{bmatrix} \quad (3.14)$$

The stiffness constants are expressed as functions of the engineering constants, summarised below:

$$C_{11} = \frac{1 - \nu_{23}\nu_{32}}{E_2 E_3 \Delta} \quad C_{12} = \frac{\nu_{21} + \nu_{31}\nu_{23}}{E_2 E_3 \Delta} \quad C_{13} = \frac{\nu_{31} + \nu_{21}\nu_{32}}{E_2 E_3 \Delta} \quad (3.15)$$

$$C_{22} = \frac{1 - v_{13}v_{31}}{E_1 E_3 \Delta} \quad C_{33} = \frac{1 - v_{12}v_{21}}{E_1 E_2 \Delta} \quad C_{23} = \frac{v_{32} + v_{12}v_{31}}{E_1 E_3 \Delta} \quad (3.16)$$

$$C_{44} = G_{23} \quad C_{55} = G_{13} \quad C_{66} = G_{12} \quad (3.17)$$

where

$$\Delta = \frac{1 - v_{12}v_{21} - v_{23}v_{32} - v_{31}v_{13} - 2v_{21}v_{32}v_{13}}{E_1 E_2 E_3} \quad (3.18)$$

In addition to the above, the relation between Young's moduli and Poisson's ratio is expressed as the following:

$$\frac{E_i}{v_{ij}} = \frac{E_j}{v_{ji}}, \quad i, j = 1, 2, 3 \quad (3.19)$$

In the case of unidirectional laminated composites, material exhibits transverse isotropic behaviour, the stiffness matrix can therefore, be simplified.

$$C_{13} = C_{12} \quad C_{33} = C_{22} \quad C_{55} = C_{66} \quad C_{44} = \frac{1}{2}(C_{22} - C_{23}) \quad (3.20)$$

3.1.2.2 Micromechanics Model

There has been an evolving development in describing the effective mechanical properties of composite structures in a micro level, i.e. looking into a greater detail of fibre-matrix constitution and work out a homogenised properties for a representative fraction of the composites. The micro-mechanics modelling can be divided into two main categories: FE based models and analytical models. By adopting an FE-based micromechanical modelling approach, researchers identify a representative volume element (RVE) or so-called unit cell, where fibres and the surrounding matrix are modelled (Ersoy et al., 2010a). While in the early days the effective mechanical properties of a composite structure were concerned with individual material moduli and volume fraction, i.e. rule-of-mixtures, which are otherwise independent of

the geometry so long as the assumption of homogenisation and transverse isotropy holds. One leap forward is the self-consistent micromechanics model deduced by Hill (1965), following which, the doubly embedded self-consistent field micromechanics (SCFM) model was proposed by Bogetti and Gillespie Jr (1992) and has been widely accepted since then. The transversely isotropic engineering constants of the lamina using SCFM are expressed as the follows:

The longitudinal Young's modulus:

$$E_{11} = E_{11f}V_f + E_r(1 - V_f) + \frac{4(v_r - v_{12f}^2)k_f k_r G_r (1 - V_f)V_f}{(k_f + G_r)k_r + (k_f - k_r)G_r V_f} \quad (3.21)$$

The transverse Young's modulus:

$$E_{22} = E_{33} = \frac{1}{1/(4k_T) + 1/(4G_{23}) + v_{12}^2/E_{11}} \quad (3.22)$$

The major Poisson's ratio:

$$v_{12} = v_{13} = v_{12f}V_f + v_r(1 - V_f) + \frac{(v_r - v_{12f})(k_r - k_f)G_r(1 - V_f)V_f}{(k_f + G_r)k_r + (k_f - k_r)G_r V_f} \quad (3.23)$$

The in-plane shear modulus:

$$G_{12} = G_{13} = G_r \frac{(G_{12f} + G_r) + (G_{12f} - G_r)V_f}{(G_{12f} + G_r) - (G_{12f} - G_r)V_f} \quad (3.24)$$

The transverse shear modulus:

$$G_{23} = \frac{G_r(k_r(G_r + G_{23f}) + 2G_{23f}G_r + k_r(G_{23f} - G_r)V_f)}{k_r(G_r + G_{23f}) + 2G_{23f}G_r - (k_r + 2G_r)(G_{23f} - G_r)V_f} \quad (3.25)$$

The transverse Poisson's ratio:

$$v_{23} = \frac{2E_{11}k_t - E_{11}E_{22} - 4v_{12}^2 k_t E_{22}}{2E_{11}k_t} \quad (3.26)$$

where the plane-strain bulk modulus of the composite for lateral dilatation without fibre extension, are shown below:

$$k_f = \frac{E_{22f}}{2(1 - \nu_{12f} - 2\nu_{12f}^2)} \quad (3.27)$$

$$k_r = \frac{E_r}{2(1 - \nu_r - 2\nu_r^2)} \quad (3.28)$$

$$k_t = \frac{(k_f + G_r)k_r + (k_f - k_r)G_rV_f}{(k_f + G_r) - (k_f - k_r)V_f} \quad (3.29)$$

The effective chemical shrinkage strains (ε^{ch}) and the effective coefficients of thermal expansion (α^{cte}) can be expressed in the same manner as shown in Eq. (3.30) and Eq. (3.31). In the case of chemical shrinkage, since the effective chemical strain is only contributed by resin matrix, α_{1f} and α_{2f} are taken to be zero.

In the longitudinal direction,

$$\alpha_1 = \frac{\alpha_{1f}E_{1f}V_f + \alpha_m E_m(1 - V_f)}{E_{1f}V_f + E_m(1 - V_f)} \quad (3.30)$$

In the transverse direction,

$$\begin{aligned} \alpha_2 = \alpha_3 = & (\alpha_{2f} + \nu_{12f}\alpha_{1f})V_f + (\alpha_m + \nu_{12m}\alpha_m)(1 - V_f) \\ & - [\nu_{12f}V_f + \nu_{12m}(1 - V_f)]\alpha_1, \end{aligned} \quad (3.31)$$

where V_f is fibre volume fraction, E_f and E_m are the Young's modulus of fibre and resin matrix.

3.1.3 Resin Property Modelling

3.1.3.1 Linear Elastic Model

Though physically resin exhibits viscoelastic behaviour, the characterisation of such behaviour requires substantial experimental efforts. To simplify the problem, pseudo-viscoelastic constitutive models are developed based on a modified linear elastic modelling approach. Bogetti and Gillespie Jr (1992) proposed a cure-dependent instantaneous isotropic resin model which is expressed in a convenient α -mixing rule, shown in Eq.(3.32).

$$E_m = (1 - \alpha_{mod})E_m^0 + \alpha E_m^\infty + \gamma \alpha_{mod}(1 - \alpha_{mod})(E_m^\infty - E_m^0) \quad (3.32)$$

where

$$\alpha_{mod} = \frac{\alpha - \alpha_{gel}^{mod}}{\alpha_{diff}^{mod} - \alpha_{gel}^{mod}} \quad (3.33)$$

In the above expression, E_m^0 and E_m^∞ represents the fully uncured and fully cured resin moduli respectively. α_{gel}^{mod} and α_{diff}^{mod} are two bounds on the degree of cure, between which resin is assumed to develop. The former bound (α_{gel}^{mod}) indicates the initialisation of gelation and the latter bound (α_{diff}^{mod}) indicates the completion of vitrification. A parameter γ is introduced to control the competing mechanisms between stress relaxation and chemical hardening, the value of which is bounded between -1 and 1. One may note that the uncured resin modulus (E_m^0) is generally taken as an arbitrary small value or in most cases, as $E_m^\infty/1000$.

3.1.3.2 CHILE Model

However, Bogetti's model has its limited use and does not account for the temperature-dependent phenomena. For instance, as resin reaches glass transition temperature, the increase in the resin modulus is exaggerated. Johnston et al. (2001) revised Bogetti's model by introducing temperature dependency in his Cure Hardening In-

stantaneous Linear Elastic (CHILE) constitutive model, expressed as the followings:

$$E_m = \begin{cases} E_m^0 & T^* \leq T_{C1}^* \\ E_m^0 + \frac{T^* - T_{C1}^*}{T_{C2}^* - T_{C1}^*} (E_m^\infty - E_m^0) & \text{for } T_{C1}^* < T^* < T_{C2}^* \\ E_m^\infty & T_{C2}^* \leq T^*, \end{cases} \quad (3.34)$$

$$T^* = T_g(\alpha) - T \quad (3.35)$$

$$T_{C1}^* = T_{C1a}^* + T_{C1b}^* \cdot T \quad (3.36)$$

where T^* represents the difference between the resin temperature (T) and the resin glass transition temperature ($T_g(\alpha)$). T_{C1}^* and T_{C2}^* are fitting constants derived from experiments, denoting two bounds where in-between the glass transition takes place. In the CHILE model, an accurate relation between the degree of cure and the glass transition temperature is crucial. Table 3.2 summarised parameters that are experimentally fitted by Johnston (1997). The DiBenedetto equation Eq.(2.2) can be used. In the case of characterising the $T_g(\alpha)$ of resin 8552, Johnston (1997) assumed a linear relationship as shown in Eq.(3.37),

$$T^* = (T_g^0 + \alpha_{T_g} \cdot \alpha) - T \quad (3.37)$$

where T_g^0 is the glass transition temperature for uncured resin and α_{T_g} is a constant. Ersoy et al. (2005a) implemented a cure quench method to obtain the T_g development for resin 8552. A polynomial fitting to the experimental data between α and T_g is expressed as:

$$T_g = 164.6\alpha^2 + 51.0\alpha + 2.67 \quad (3.38)$$

where T_g is in Celsius.

3.1. THERMAL-CHEMICAL-MECHANICAL ANALYSIS

Parameters	Value	Unit	Comments
E_r^∞	4670	[MPa]	Unrelaxed resin modulus
E_r^0	4.67	[MPa]	Fully relaxed resin modulus
T_{C1a}	-45.7	[K]	Lower critical value for T^* at 0K
T_{C1b}	0.0	[K]	Variation of lower critical value for T^* with increase in temperature
T_{C2}	-12	[K]	Upper critical value for T^*
T_g^0	268	[K]	Glass transition temperature at DoC=0
α_{T_g}	220	[K]	Variation of glass transition temperature at DoC=0

Table 3.2: Parameters used for 8552 resin modulus development using CHILE model (Johnston, 1997)

The modulus development of 8552 resin as a function of temperature and DoC using the CHILE approach are shown in Figure 3.1 (a) and (b). Figure 3.1(a) can be interpreted as under isothermal conditions, increasing the temperature shifts the development of E_r to occur at a higher DoC. Equivalently presented in Figure 3.1(b), the DoC can be regarded as a 'shift factor', for a given DoC which indicates a corresponding T_g , reducing the temperature increases the T^* and once it falls in-between the bounds T_{C1}^* and T_{C2}^* , the glass transition or vitrification occurs.

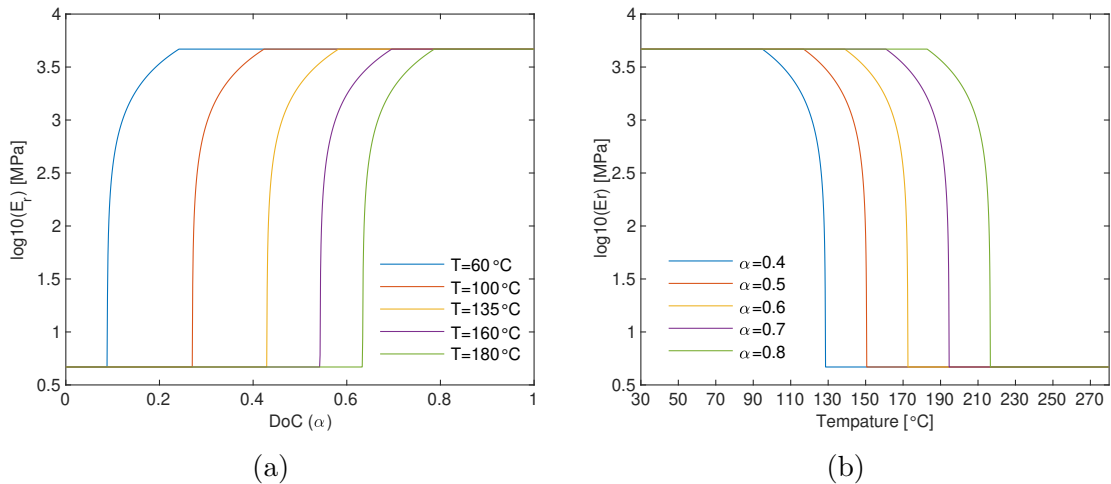


Figure 3.1: The modulus development of 8552 resin as a function of (a) DoC and (b) temperature using the CHILE approach

3.2 Effective Laminate Distortion using CLT

3.2.1 Classic Laminate Theory

The stress analyses of laminate plates is either based on the equivalent single layer (ESL) theories (2D) or elasticity theory (3D). Among the ESL approaches, classical laminate theory (CLT) and the shear deformation theory (SDT) are the most commonly used (Reddy, 2004). The CLT approach is based on the Kirchhoff's plate theory, assuming that any plane normal to the mid-surface remains plane and normal to the deformed mid-surface. The SDT approach is extended on the Mindlin plate theory which includes transverse shear deformation. In this section, the CLT will be revised and extended to calculate effective laminates behaviours taking thermal and chemical strains into consideration.

The stress-strain relation for a single ply with transverse isotropic material, assuming plane-stress condition holds, is given as:

$$\begin{bmatrix} \varepsilon_1 \\ \varepsilon_2 \\ \gamma_{12} \end{bmatrix} = \begin{bmatrix} S_{11} & S_{12} & 0 \\ S_{12} & S_{22} & 0 \\ 0 & 0 & S_{66} \end{bmatrix} \begin{bmatrix} \sigma_1 \\ \sigma_2 \\ \tau_{12} \end{bmatrix} \quad (3.39)$$

where

$$S_{11} = \frac{1}{E_1}, \quad S_{22} = \frac{1}{E_2}, \quad S_{66} = \frac{1}{G_{12}} \quad (3.40)$$

$$S_{12} = \frac{-\nu_{21}}{E_1} = \frac{-\nu_{12}}{E_2}, \quad S_{13} = \frac{-\nu_{31}}{E_1}, \quad S_{23} = \frac{-\nu_{32}}{E_2} \quad (3.41)$$

Rewrite Eq. (3.39) gives

$$\begin{bmatrix} \sigma_1 \\ \sigma_2 \\ \tau_{12} \end{bmatrix} = \begin{bmatrix} Q_{11} & Q_{12} & 0 \\ Q_{12} & Q_{22} & 0 \\ 0 & 0 & Q_{66} \end{bmatrix} \begin{bmatrix} \varepsilon_1 \\ \varepsilon_2 \\ \gamma_{12} \end{bmatrix} \quad (3.42)$$

where

$$Q_{11} = \frac{S_{22}}{S_{11}S_{22} - S_{12}^2} = \frac{E_1}{1 - \nu_{12}\nu_{21}}, \quad Q_{22} = \frac{S_{11}}{S_{11}S_{22} - S_{12}^2} = \frac{E_2}{1 - \nu_{12}\nu_{21}} \quad (3.43)$$

$$Q_{12} = \frac{-S_{12}}{S_{11}S_{22} - S_{12}^2} = \frac{\nu_{21}E_2}{1 - \nu_{12}\nu_{21}}, \quad Q_{66} = \frac{1}{S_{66}} = G_{12} \quad (3.44)$$

To account for fibre orientations at individual layer, a transformation matrix is introduced to transfer the stiffness matrix from its principal axes (1 – 2) to off-axis ($x - y$). This transformation matrix is written as

$$[\mathbf{T}] = \begin{bmatrix} c^2 & s^2 & 2cs \\ s^2 & c^2 & -2cs \\ -cs & cs & c^2 - s^2 \end{bmatrix}, \quad (3.45)$$

where c denotes $\cos \theta$ and s denotes $\sin \theta$. θ is the orientation angle of the fibre reinforcement.

The stress-strain relationship for a unidirectional or orthotropic composite, off its principal directions, i.e. under coordinate system $x - y$, is shown in Eq. (3.46).

$$\begin{bmatrix} \sigma_x \\ \sigma_y \\ \tau_{xy} \end{bmatrix} = \begin{bmatrix} \bar{Q}_{11} & \bar{Q}_{12} & \bar{Q}_{16} \\ \bar{Q}_{12} & \bar{Q}_{22} & \bar{Q}_{26} \\ \bar{Q}_{16} & \bar{Q}_{26} & \bar{Q}_{66} \end{bmatrix} \begin{bmatrix} \varepsilon_x \\ \varepsilon_y \\ \gamma_{xy} \end{bmatrix} \quad (3.46)$$

where, the reduced stiffness constants $[\bar{Q}_{ij}]$ are calculated as follows:

$$\bar{Q}_{11} = Q_{11} \cos^4 \theta + Q_{22} \sin^4 \theta + 2(Q_{12} + 2Q_{66}) \sin^2 \theta \cos^2 \theta \quad (3.47)$$

$$\bar{Q}_{12} = (Q_{11} + Q_{22} - 4Q_{66}) \sin^2 \theta \cos^2 \theta + Q_{12}(\cos^4 \theta + \sin^4 \theta) \quad (3.48)$$

$$\bar{Q}_{16} = (Q_{11} - Q_{12} - 2Q_{66}) \sin \theta \cos^3 \theta + (Q_{12} - Q_{22} + 2Q_{66}) \cos \theta \sin^3 \theta \quad (3.49)$$

$$\bar{Q}_{22} = Q_{11} \sin^4 \theta + Q_{22} \cos^4 \theta + 2(Q_{12} + 2Q_{66}) \sin^2 \theta \cos^2 \theta \quad (3.50)$$

$$\bar{Q}_{26} = (Q_{11} - Q_{12} - 2Q_{66}) \sin^3 \theta \cos \theta + (Q_{12} - Q_{22} + 2Q_{66}) \sin \theta \cos^3 \theta \quad (3.51)$$

$$\bar{Q}_{66} = [Q_{11} + Q_{22} - 2(Q_{12} + Q_{66})] \sin^2 \theta \cos^2 \theta + Q_{66}(\sin^4 \theta + \cos^4 \theta) \quad (3.52)$$

From single ply behaviour to macroscopic behaviour of a laminate, one apply Kirchhoff's hypothesis, i.e. the transverse shear strains in the through-thickness direction are assumed to be zero. The strain field is the superposition of:

- the in-plane strain (or mid-plane strains):

$$\varepsilon_x^0 = \frac{\partial u_0}{\partial x} \quad \varepsilon_y^0 = \frac{\partial v_0}{\partial y} \quad \tau_{xy}^0 = \frac{\partial u_0}{\partial x} + \frac{\partial v_0}{\partial y} \quad (3.53)$$

- the flexural strains (bending and twisting strains):

$$\varepsilon_x^f = -z \frac{\partial^2 w_0}{\partial x^2} \quad \varepsilon_y^f = -z \frac{\partial^2 w_0}{\partial y^2} \quad \tau_{xy}^f = -2z \frac{\partial^2 w_0}{\partial x \partial y} \quad (3.54)$$

Combining Eq. (3.53) and Eq. (3.54) gives:

$$\begin{bmatrix} \varepsilon_x \\ \varepsilon_y \\ \tau_{xy} \end{bmatrix} = \begin{bmatrix} \varepsilon_x^0 \\ \varepsilon_y^0 \\ \tau_{xy}^0 \end{bmatrix} + z \begin{bmatrix} \kappa_x \\ \kappa_y \\ \kappa_{xy} \end{bmatrix} \quad (3.55)$$

where matrix κ is the curvature matrix of the plate subjected to bending and twist-

ing.

Taking Eq. (3.55) and Eq. (3.46) into account, the stresses in the k^{th} layer are expressed as follows:

$$\begin{bmatrix} \varepsilon_x \\ \varepsilon_y \\ \tau_{xy} \end{bmatrix}_k = \begin{bmatrix} \bar{Q}_{11} & \bar{Q}_{12} & \bar{Q}_{16} \\ \bar{Q}_{12} & \bar{Q}_{22} & \bar{Q}_{26} \\ \bar{Q}_{16} & \bar{Q}_{26} & \bar{Q}_{66} \end{bmatrix}_k \begin{bmatrix} \varepsilon_x^0 \\ \varepsilon_y^0 \\ \tau_{xy}^0 \end{bmatrix} + z \begin{bmatrix} \bar{Q}_{11} & \bar{Q}_{12} & \bar{Q}_{16} \\ \bar{Q}_{12} & \bar{Q}_{22} & \bar{Q}_{26} \\ \bar{Q}_{16} & \bar{Q}_{26} & \bar{Q}_{66} \end{bmatrix}_k \begin{bmatrix} \kappa_x \\ \kappa_y \\ \kappa_{xy} \end{bmatrix} \quad (3.56)$$

Hence, one can then deduct the in-plane resultants and moments, which leads to the expression of classical laminate theory, as written below:

$$[\mathbf{N}] = \sum_{k=1}^n \int_{z_{k-1}}^{z_k} [\boldsymbol{\sigma}]_k dz = \sum_{k=1}^n [\bar{\mathbf{Q}}]_k \int_{z_{k-1}}^{z_k} ([\boldsymbol{\varepsilon}_0] + z[\boldsymbol{\kappa}]) dz \quad (3.57)$$

$$[\mathbf{M}] = \sum_{k=1}^n \int_{z_{k-1}}^{z_k} [\boldsymbol{\sigma}]_k z dz = \sum_{k=1}^n [\bar{\mathbf{Q}}]_k \int_{z_{k-1}}^{z_k} z([\boldsymbol{\varepsilon}_0] + z[\boldsymbol{\kappa}]) dz \quad (3.58)$$

Introducing matrix $[\mathbf{A}]$

$$[\mathbf{A}] = \sum_{k=1}^n [\bar{\mathbf{Q}}]_k (z_k - z_{k-1}) \quad (3.59)$$

and matrix $[\mathbf{B}]$

$$[\mathbf{B}] = \sum_{k=1}^n \frac{1}{2} [\bar{\mathbf{Q}}]_k (z_k^2 - z_{k-1}^2) \quad (3.60)$$

gives:

$$\begin{bmatrix} N_x \\ N_y \\ N_{xy} \end{bmatrix} = \begin{bmatrix} A_{11} & A_{12} & A_{16} \\ A_{12} & A_{22} & A_{26} \\ A_{16} & A_{26} & A_{66} \end{bmatrix} \begin{bmatrix} \varepsilon_x^0 \\ \varepsilon_y^0 \\ \gamma_{xy}^0 \end{bmatrix} + \begin{bmatrix} B_{11} & B_{12} & B_{16} \\ B_{12} & B_{22} & B_{26} \\ B_{16} & B_{26} & B_{66} \end{bmatrix} \begin{bmatrix} \kappa_x \\ \kappa_y \\ \kappa_{xy} \end{bmatrix} \quad (3.61)$$

Introducing another matrix $[\mathbf{D}]$

$$[\mathbf{D}] = \sum_{k=1}^n \frac{1}{3} [\bar{\mathbf{Q}}]_k (z_k^3 - z_{k-1}^3) \quad (3.62)$$

gives:

$$\begin{bmatrix} N_x \\ N_y \\ N_{xy} \end{bmatrix} = \begin{bmatrix} B_{11} & B_{12} & B_{16} \\ B_{12} & B_{22} & B_{26} \\ B_{16} & B_{26} & B_{66} \end{bmatrix} \begin{bmatrix} \varepsilon_x^0 \\ \varepsilon_y^0 \\ \gamma_{xy}^0 \end{bmatrix} + \begin{bmatrix} D_{11} & D_{12} & D_{16} \\ D_{12} & D_{22} & D_{26} \\ D_{16} & D_{26} & D_{66} \end{bmatrix} \begin{bmatrix} \kappa_x \\ \kappa_y \\ \kappa_{xy} \end{bmatrix} \quad (3.63)$$

Combining Eq. (3.63) and Eq. (3.61) yields:

$$\begin{bmatrix} \mathbf{N} \\ \mathbf{M} \end{bmatrix} = \begin{bmatrix} \mathbf{A} & \mathbf{B} \\ \mathbf{B} & \mathbf{D} \end{bmatrix} \begin{bmatrix} \boldsymbol{\varepsilon}_0 \\ \boldsymbol{\kappa} \end{bmatrix} \quad (3.64)$$

where

$$[\mathbf{A}, \mathbf{B}, \mathbf{D}] = \sum_{k=1}^n [\bar{\mathbf{Q}}]_k \left((z_k - z_{k-1}), \frac{1}{2}(z_k^2 - z_{k-1}^2), \frac{1}{3}(z_k^3 - z_{k-1}^3) \right) \quad (3.65)$$

$[\mathbf{A}]$ is the extensional stiffness matrix, $[\mathbf{B}]$ is the coupling stiffness matrix and $[\mathbf{D}]$ is the bending stiffness matrix.

3.2.2 Process-Induced Strains

There are two major sources of process-induced strains during the autoclave cure process, namely, chemical shrinkage and thermal effect. The effective elastic strains can therefore be expressed as the following:

$$[\boldsymbol{\varepsilon}^e] = [\boldsymbol{\varepsilon}^T] - [\boldsymbol{\varepsilon}^{Pr}] \quad (3.66)$$

where,

- $[\boldsymbol{\varepsilon}^T]$ is total strain
- $[\boldsymbol{\varepsilon}^{Pr}]$ is process-induced strain

Typically the incremental process-induced strains are in relation to the increment in DoC and temperature, as expressed below.

$$\Delta\varepsilon^{Pr} = \begin{cases} 0 & \alpha \leq \alpha_{gel} \\ \alpha^{cte}\Delta T + \beta\Delta\alpha & \alpha > \alpha_{gel} \end{cases} \quad (3.67)$$

where

- α^{cte} is the coefficient of thermal expansion
- β is the coefficient chemical shrinkage

Two common methods were widely employed in calculating chemical shrinkage, one is based on volumetric shrinkage of a unit resin cube and another is based on coefficient measurement of laminates, as an analogy to the measurement of CTE. One should be reminded that the chemical shrinkage is induced from resin only under isothermal condition.

Assuming a resin sample has a dimension of l_1 , l_2 and l_3 , the corresponding chemical shrinkage in each principal direction are Δl_1 , Δl_2 , Δl_3 . The total volumetric shrinkage is:

$$\Delta V = l_1 l_2 \Delta l_3 + l_1 \Delta l_2 l_3 + l_1 \Delta l_2 l_3 + \Delta l_1 \Delta l_2 l_3 + l_1 \Delta l_2 \Delta l_3 + \Delta l_1 l_2 \Delta l_3 + \Delta l_1 \Delta l_2 \Delta l_3 \quad (3.68)$$

The incremental specific volumetric change of the resin ΔV_{sh} is

$$\Delta V_{sh} = \frac{\Delta V}{l_1 l_2 l_3} = \varepsilon_1 + \varepsilon_2 + \varepsilon_3 + \varepsilon_1 \varepsilon_2 + \varepsilon_1 \varepsilon_3 + \varepsilon_2 \varepsilon_3 + \varepsilon_1 \varepsilon_2 \varepsilon_3 \quad (3.69)$$

In an isotropic resin matrix sample, $\varepsilon_m = \varepsilon_1 = \varepsilon_2 = \varepsilon_3$, the incremental normal strain is given by

$$\varepsilon_m = \sqrt[3]{1 + \Delta V_{sh}} - 1 \quad (3.70)$$

Bogetti and Gillespie Jr (1992) assumes that ΔV_m is proportional to the incremental curing degree, given by

$$\Delta V_{sh} = \Delta\alpha \cdot V_{sh}^T \quad (3.71)$$

where V_{sh}^T is the specific total volumetric shrinkage of resin determined experimentally.

Given the fact that resin shrinkage is primarily undertaken in between gelation and vitrification, Johnston (1997) replaced the term V_{sh}^T in Eq. (3.71) as the following:

$$V_{sh} = \begin{cases} 0 & \alpha < \alpha_{c1} \\ A_{sh} \cdot \alpha_s + (V_{sh}^T - A_{sh}) \cdot \alpha_s^2 & \text{for } \alpha_{c1} \leq \alpha \leq \alpha_{c2} \\ V_{sh}^T & \alpha \geq \alpha_{c2}, \end{cases} \quad (3.72)$$

where

$$\alpha_s = \frac{\alpha - \alpha_{c1}}{\alpha_{c2} - \alpha_{c1}}, \quad (3.73)$$

and α_{c1} , α_{c2} are two critical curing degrees that specify the bounds of the $V_{sh} - \alpha$ relationship, typically denotes DoC at the gelation and vitrification points. A_{sh} is a user-defined constant.

The incremental thermal strain is given by the expression of the coefficient of thermal expansion (α^{cte}).

$$[\epsilon^{th}] = \begin{bmatrix} \alpha_1^{cte} \\ \alpha_2^{cte} \\ \alpha_3^{cte} \end{bmatrix} \Delta T. \quad (3.74)$$

The CTE in the fibre direction is practically zero and usually neglected ($\alpha_1^{cte} = 0$). In the case a unidirectional laminate, one may assume that $\alpha_2^{cte} = \alpha_3^{cte}$.

3.2.3 Effective Laminate Residual Stresses

Now considering an isotropic material for example, the stress-strain relationship is expressed as:

$$\begin{bmatrix} \sigma_1 \\ \sigma_2 \\ \tau_{12} \end{bmatrix} = \frac{E}{1-\nu^2} \begin{bmatrix} 1 & \nu & 0 \\ \nu & 1 & 0 \\ 0 & 0 & (1-\nu)/2 \end{bmatrix} \begin{bmatrix} \varepsilon_1 \\ \varepsilon_2 \\ \gamma_{12} \end{bmatrix} \quad \text{or} \quad [\boldsymbol{\sigma}] = [\mathbf{Q}][\boldsymbol{\varepsilon}]. \quad (3.75)$$

Recall that the process-induced chemical and thermal strains are also contributing to the total strains, the effective plane stresses can be obtained by subtracting in-elastic strains from the total strains.

$$[\boldsymbol{\sigma}]_k = [\bar{\mathbf{Q}}]_k([\boldsymbol{\varepsilon}_0] + z[\boldsymbol{\kappa}] - [\boldsymbol{\varepsilon}^{Pr}]) \quad (3.76)$$

The process-induced strain ($[\boldsymbol{\varepsilon}^{Pr}]$) is written as

$$[\boldsymbol{\varepsilon}^{Pr}] = \begin{bmatrix} \varepsilon_1^{ch} \\ \varepsilon_2^{ch} \\ \varepsilon_3^{ch} \end{bmatrix} + \begin{bmatrix} \varepsilon_1^{th} \\ \varepsilon_2^{th} \\ \varepsilon_3^{th} \end{bmatrix}, \quad (3.77)$$

Therefore, the effective plate force and moment acting on a laminate are written as

$$[\mathbf{N}] = \sum_{k=1}^n \int_{z_{k-1}}^{z_k} [\boldsymbol{\sigma}]_k dz = \sum_{k=1}^n [\bar{\mathbf{Q}}]_k \int_{z_{k-1}}^{z_k} ([\boldsymbol{\varepsilon}_0] + z[\boldsymbol{\kappa}] - [\boldsymbol{\varepsilon}^{Pr}]) dz \quad (3.78)$$

$$[\mathbf{M}] = \sum_{k=1}^n \int_{z_{k-1}}^{z_k} [\boldsymbol{\sigma}]_k z dz = \sum_{k=1}^n [\bar{\mathbf{Q}}]_k \int_{z_{k-1}}^{z_k} z([\boldsymbol{\varepsilon}_0] + z[\boldsymbol{\kappa}] - [\boldsymbol{\varepsilon}^{Pr}]) dz \quad (3.79)$$

3.3 Material Characterisations

This section looks into the characterisation of high performance prepregs with epoxy resin matrix system. Such matrix system are formulated to achieve higher toughness, better damage resistance, better performance in compression after impact, so that they act ideally towards industrial standards for primary aircraft structures. Hereby, a well-studied epoxy resin matrix systems 3501-6, 8552 and M21 were selected for illustration and comparison purposes.

3.3.1 Cure-Kinetic Properties of the Resin

Epoxy 3501-6 has been and remains today, one of the most studied resin system in the form of prepregs. Lee et al. (1982) first systematically examined the cure kinetic behaviour of epoxy resin 3501-6. Their study employed autocatalytic model to describe the heat generation rate, or equivalently, degree of cure rate. A slight modification was made based on the original expression so that the heat release could be characterised into two distinct phases, capturing two major reactions occurred during cure. The expression is written in forms of

$$\begin{cases} \frac{d\alpha}{dt} = (K_1 + K_2\alpha)(1 - \alpha)(0.47 - \alpha) & \alpha \leq 0.3 \\ \frac{d\alpha}{dt} = K_3(1 - \alpha) & \alpha > 0.3. \end{cases} \quad (3.80)$$

where

$$\begin{cases} K_1 = A_1 \cdot \exp(-\Delta E_1/RT) \\ K_2 = A_2 \cdot \exp(-\Delta E_2/RT) \\ K_3 = A_3 \cdot \exp(-\Delta E_3/RT) \end{cases} \quad (3.81)$$

The value of constants in Eq.(3.80) are given below.

Hubert et al. (2001) presented the cure kinetics model for 8552 epoxy resin, using a modified autocatalytic equation given in Eq.(3.82). This model takes into account

3.3. MATERIAL CHARACTERISATIONS

A_1	$[min^{-1}]$	2.101e9	ΔE_1	$[J/mol]$	8.07e4
A_2	$[min^{-1}]$	-2.014e9	ΔE_2	$[J/mol]$	7.78e4
A_3	$[min^{-1}]$	1.960e5	ΔE_3	$[J/mol]$	5.66e4

Table 3.3: Value of constants in Eq.(3.80)

the shift from a kinetics-controlled reaction to a diffusion-controlled reaction as resin reaches vitrification status. Their model is in a good agreement with the work done by Ersoy et al. (2005a).

$$\frac{d\alpha}{dt} = \frac{K\alpha^m(1-\alpha)^n}{1 + \exp[C(\alpha - \alpha_C)]} \quad (3.82)$$

where,

$$\alpha_C = \alpha_{C0} + \alpha_{CT}T \quad (3.83)$$

$$K = A \exp\left[\frac{-\Delta E_a}{RT}\right] \quad (3.84)$$

The experimentally determined constants in Eq.(3.82) are shown in Table 3.4.

Constants	[Unit]	Value	Comments
H_T	$[J/kg]$	574000	Total heat of reaction
E_a	$[J/mol]$	65000	Activation energy
A	$[s^{-1}]$	70000	Pre-exponential cure rate coefficient
m	$[/]$	0.5	First exponential constant
n	$[/]$	1.5	Second exponential constant
R	$[J/mol/K]$	8.314	Gas constant
C	$[/]$	30	Diffusion constant
α_{C0}	$[K^{-1}]$	-1.5148	Critical DoC at T=0K
α_{CT}	$[/]$	5.171×10^{-3}	Constant accounting for temperature dependence

Table 3.4: Constants for 8552 cure kinetics model (Ersoy et al., 2005a)

3.3.2 DoC-dependent Mechanical Properties

The characterisation of mechanical properties requires a large set of experimental work, which are usually time consuming and sometimes, even challenging as in the case of uncured prepregs. The fibre and fully cured resin properties are relatively easy to measure, as the example shown in Table 3.5.

Properties	[Unit]	AS4 fibre	3501-6	Comments
E_{11}	[GPa]	207.0	3.2	Longitudinal Young's modulus
$E_{22} = E_{33}$	[GPa]	20.7	3.2	Transverse Young's modulus
$G_{12} = G_{13}$	[GPa]	27.6	1.19	In-plane shear modulus
G_{23}	[MPa]	6.89	1.19	Transverse shear modulus
$\nu_{12} = \nu_{13}$	[-]	0.2	0.35	In-plane Poisson's ratio
ν_{23}	[-]	0.3	0.35	Transverse Poisson's ratio

Table 3.5: Material properties of AS4/3501-6 prepregs (White and Kim, 1998)

However, recall the resin development in the process of cure, as detailed in section 2.2.2, resin begins to contribute to the residual stresses once it goes into a rubbery state, the properties of which therefore need to be identified. The characterisation of such properties would usually requires some valid assumptions. The Young's modulus of uncured resin is usually assumed to be 1/1000 of fully cured resin (Bogetti and Gillespie Jr, 1992). Since rubber exhibits nearly incompressible behaviour, the Poisson's ratio of which would hence be close to 0.5.

Taking AS4/8552 for example, the properties of uncured and cured resin matrix 8552 are shown in Table 3.6.

The effective mechanical properties of AS4/8552 unidirectional laminates using micromechanical models are shown in Table 3.7, where the effective properties calculated using SCFM in this study were compared to the FE-based model presented in Ersoy et al. (2010a). The fibre volume fraction of the AS4/8552 is 57%. It shows a good agreement between the results using Eq.3.21 to Eq.3.29 and the results given by Ersoy et al. (2010a). For the calculation of plane strain bulk modulus to be valid, the in-plane Poisson's ratio of resin is chosen to be 0.499.

3.3. MATERIAL CHARACTERISATIONS

Properties	[Unit]	AS4	8552		Comments
			Uncured	Cured	
E_{11}	[MPa]	228000	4.67	4670	Longitudinal Young's modulus
$E_{22} = E_{33}$	[MPa]	17200	4.67	4670	Transverse Young's modulus
$G_{12} = G_{13}$	[MPa]	27600	11	1704	In-plane shear modulus
G_{23}	[MPa]	5730	11	1704	Transverse shear modulus
$\nu_{12} = \nu_{13}$	[-]	0.2	0.5	0.37	In-plane Poisson's ratio
ν_{23}	[-]	0.5	0.5	0.37	Transverse Poisson's ratio
V_f	[%]	57.42			Fibre volume fraction

Table 3.6: Mechanical properties of AS4 fibre and 8552 uncured and cured resin (Ersoy et al., 2010a)

Properties	[Unit]	SCFM		FEBM (Ersoy et al., 2010a)	
		Uncured	Cured	Uncured	Cured
E_{11}	[MPa]	130000	132400	132200	134000
$E_{22} = E_{33}$	[MPa]	154	9224	165	9480
$G_{12} = G_{13}$	[MPa]	40.1	5163	44.3	5490
G_{23}	[MPa]	39.5	3127	41.6	3272
$\nu_{12} = \nu_{13}$	[-]	0.328	0.268	0.346	0.271
ν_{23}	[-]	0.954	0.475	0.982	0.448

Table 3.7: Effective mechanical properties of AS4/8552 unidirectional laminates using SCFM and FEBM

3.3.3 Thermal-Chemical Shrinkage

The thermal-chemical strain developed during the cure process can be traced back to the intrinsic properties of the chemical shrinkage and thermal expansion of the resin. Equivalent to the coefficient of thermal expansion (CTE) in describing the thermally induced behaviour, researchers have also introduced the coefficient of chemical shrinkage (CCS) in characterising the chemical induced residual strains. As for CTE is a temperature dependent measure of strains, CCS is usually expressed in a similar manner, as a function of the DoC.

There exists a variety of techniques characterising the chemical shrinkage of a resin, systematically reviewed by Nawab et al. (2013). His work distinguished these methods into two categories, namely non-volumetric dilatometry including rheometer, FBGs, TMA and DMA; and volumetric dilatometry, such as capillary type, plunger

type and gravimetric methods. Among these techniques, thermomechanical analysis (TMA) is insofar one of the most widely adopted techniques for characterising chemical shrinkage. In terms of structural health monitoring, Optical fibre Bragg gratings sensors (FBGs) have also been one of the favoured choices to continuously monitoring the global stress build-up at various designated locations in-between composites plies (Mulle et al., 2009). Other studies also derived the resin shrinkage through uncured and cured net resin shrinkage using the gravimetric method (Li et al., 2004; Khoun and Hubert, 2010).

White and Kim (1998) presented the CTE and CCS of fully cured AS4/3501-6 prepregs in the principal material directions, shown in Table 3.8. It is common to assume that for unidirectional laminated composites, the chemical and thermal shrinkage percentage in transverse in-plane direction (ϵ_2^c) and through-thickness direction (ϵ_3^c) are identical. Since fibres do not exhibit noticeable shrinkage as temperature varies, it is reasonable to assume the shrinkage in longitudinal direction (ϵ_1^c) is close to zero.

Properties	[Unit]	Value	Comments
α_{11}^t	$[\mu\epsilon/^\circ\text{C}]$	0.5	Longitudinal CTE
α_{22}^t	$[\mu\epsilon/^\circ\text{C}]$	35.3	Transverse CTE
α_{33}^t	$[\mu\epsilon/^\circ\text{C}]$	35.3	Transverse CTE
ϵ_{11}^c	$[\mu\epsilon]$	-167.0	Longitudinal chemical shrinkage
ϵ_{22}^c	$[\mu\epsilon]$	-8810.0	Transverse chemical shrinkage
ϵ_{33}^c	$[\mu\epsilon]$	-8810.0	Transverse chemical shrinkage

Table 3.8: CTE and CCS of fully cured AS4/3501-6 prepregs in principle directions

Garstka et al. (2007) investigated the relationship between cure shrinkage and the DoC. A third order polynomial was fitted to the shrinkage data of AS4/8552 cross-ply laminates after gelation ($\alpha > \alpha_{gel}$) under 150°C , 160°C and 170°C isothermal cure conditions, expressed as in Eq. 3.85. For a fully cured laminates with 57% fibre

3.3. MATERIAL CHARACTERISATIONS

volume fraction, the cure shrinkage after gelation equals to 1.23%.

$$\epsilon_{cure} = 2.16\alpha^3 - 1.62\alpha^2 - 2.7\alpha + 0.93[\%] \quad (3.85)$$

The study found that the total through-thickness chemical shrinkage strain in cross-ply laminates is approximately twice the value of that in unidirectional laminates. Such experimental results can be intuitively explained as resin shrinkage is constrained in fibre direction, the in-plane transverse and through-thickness strains for UD laminates are free to adopt any shrinkage. While in the case of cross-ply laminates, the cure shrinkage measured is equivalent to the volumetric cure shrinkage since the strains are restrained in both in-plane fibre directions. The average shrinkage for UD specimen was found to be 0.48% and the average shrinkage for cross-ply specimen was found to be 0.98% respectively. Since gelation took place during the second temperature ramp, and vitrification was reached during the second temperature dwell, the previously measured shrinkage has included the counter-effect from thermal expansion.

Treating the chemical and thermal effect separately, the thermal and chemical shrinkage of UD and cross-ply AS4/8552 prepregs are summarised in Table 3.9. Such measurement was based on the experimental observation that chemical shrinkage is dominant in the rubbery state, while thermal shrinkage took place as resin surpass the glass transition temperature (T_g), i.e. in the glassy state.

Properties [Unit]	Unidirectional		Cross-ply		Comments
	Rubbery	Glassy	Rubbery	Glassy	
α_{11}^t [$\mu\epsilon/^\circ\text{C}$]	-	0	-	0	Longitudinal CTE
α_{22}^t [$\mu\epsilon/^\circ\text{C}$]	-	32.6	-	0	Transverse CTE
α_{33}^t [$\mu\epsilon/^\circ\text{C}$]	-	32.6	-	42.5	Through-thickness CTE
ϵ_{11}^c [%]	0	-	0	-	Longitudinal CCS
ϵ_{22}^c [%]	0.48	-	0	-	Transverse CCS
ϵ_{33}^c [%]	0.48	-	0.98	-	Through-thickness CCS

Table 3.9: Thermal and chemical shrinkage measurements for unidirectional and cross-ply AS4/8552 prepregs

Although many studies developed the models based on the transverse isotropic assumption, the CTE and CCS of M21/IMA prepregs measured by Zbed et al. (2022) clearly showed an anisotropic behaviour, which may be explained by the interleaved thermoplastic layer added to the M21 resin system. Their study designed a particular autoclave cure cycle so that counter-acting mechanisms, namely compaction, chemical shrinkage and thermal effect, were separated into four individually dominant phases. As the result, the thermal expansion coefficient for uncured state and that for fully cured state was derived from individual phase. In the isothermal dwell, since thermal effect was eliminated, chemical shrinkage can be easily estimated in dependent of DoC, together with the CTEs, shown in Table 3.10.

		Uncured	Fully cured	
α_{11}^t	$[\mu K^{-1}]$	0	0	Longitudinal CTE
α_{22}^t	$[\mu K^{-1}]$	110±11	39±4	Transverse CTE
α_{33}^t	$[\mu K^{-1}]$	178±9	55±4	Through-thickness CTE
		Before gelation	After gelation	
ϵ_{11}^c	$[\%]$	0	0	Longitudinal CCS
ϵ_{22}^c	$[\%]$	-0.27±0.04	-1.4±0.09	Transverse CCS
ϵ_{33}^c	$[\%]$	-3.83±0.3	-2.07±0.1	Through-thickness CCS

Table 3.10: CTE and CCS measurements of M21/IMA prepregs

3.4 Summary

In this chapter, the effective laminate residual stresses were illustrated based on CLT. The equations of process-induced strains and stresses presented here will be implemented in the Matlab model presented in Chapter 4. In the following-up chapters, the CHILE constitutive model and the properties of the 8552 embedded epoxy resin system will also be adopted in ABAQUS modelling framework.

Chapter 4

1D Modelling of Residual Stresses in Laminates

4.1 Overview

In this chapter, the residual stress distributions through the thickness of laminates were investigated. The autoclave cure process of flat laminates was numerically implemented in Matlab using the forward Euler discretisation method. CLT was employed taking account of process-induced strains, i.e. thermal and chemical strains. Parametric analyses were performed looking into the effect of laminate thickness and cure cycle on the residual stresses distribution in the thickness direction. This chapter revealed the limitation of manufacturing recommended cure cycle (MRCC) on thick laminates, and an MRCC optimisation is suggested to improve the manufacturing efficiency.

4.2 Numerical Implementation in Matlab

4.2.1 Forward Euler Discretisation Method

The governing equation of the coupled thermal and chemical heat transfer problem has been discussed earlier in section 3.1.1. The heat transfer equation in the through-thickness direction is written as

$$\rho_r C_p \frac{\partial T}{\partial t} = k_z \frac{\partial^2 T}{\partial z^2} + \dot{Q}_r \quad (4.1)$$

Discretising Eq.(4.1) through the thickness and through the time domain gives

$$\frac{T_i^{n+1} - T_i^n}{\Delta t} = \left(\frac{k_z}{\rho_r C_p} \right) \frac{T_{i+1}^n - 2T_i^n + T_{i-1}^n}{(\Delta z)^2} + \frac{\dot{Q}}{\rho_r C_p} \quad (4.2)$$

where, the subscript i denotes the i^{th} lamina and the subscript n denotes the n^{th} time step.

The spatial derivative is approximated by the central finite difference method and the time derivative is approximated by the forward difference approach. Such method is stable only if

$$\frac{k_z \Delta t}{(\Delta z)^2} < \frac{1}{2}. \quad (4.3)$$

The temperature at the next time step t^{n+1} can then be expressed as

$$T_i^{n+1} = rT_i^n + (1 - 2r)T_i^n + rT_{i-1}^n + q_i^n, \quad (4.4)$$

where

$$r = \left(\frac{k_z}{\rho_r C_p} \right) \left(\frac{\Delta t}{(\Delta z)^2} \right) \quad (4.5)$$

and

$$q_i^n = \frac{\dot{Q}_i^n \Delta t}{\rho_r C_p}. \quad (4.6)$$

The temperature at the top and bottom of the laminates were assumed to be equal to the cure cycle profile. The initial temperature condition at the first time step was assumed to be the room temperature.

Given the expression of the curing rate $d\alpha/dt$, for a small time increment (Δt), the Degree-of-Cure at the next time step α_i^{n+1} can then be approximated by

$$\alpha_i^{n+1} = \alpha_i^n + \frac{d\alpha_i^n}{dt} \Delta t. \quad (4.7)$$

4.2.2 Computational Framework

This section presented the computational framework, which built upon the forward Euler democratisation method, to calculate the process-induced residual stresses in the through-thickness direction of a flat laminates. The workflow of the described computational framework was illustrated in Algorithm 1.

In the initialisation step, an appropriate incremental time step Δt was determined so that the method is stable. The temperature and DoC evolution through the thickness were then computed using the finite difference method discussed in the previous section 4.2.1. The SCFM model detailed in section 3.1.2.2 was used to compute the instantaneous transverse mechanical properties of the lamina. Given the incremental DoC and the incremental temperature at each time step, the incremental chemical and thermal strains were then calculated. Hence, the process-induced normal force and bending moment were determined. The effective ply stresses or the so-called residual stresses are updated at each time increment until the cure cycle was completed.

Algorithm 1: Pseudocode of the computational framework

Data: Geometry, initial material properties, processing parameters

Initialisation;

for each time step $t = 1, 2, \dots, N_{steps}$ **do**

for each ply $i = 1, 2, \dots, N_{plies}$ **do**

$[\Delta\alpha_i^t] = \text{Cure_kinetics_model}(\alpha_i^t, T_i^t);$

$[\alpha_i^{t+1}, \Delta\alpha_i^{t+1}, T_i^{t+1}] = \text{Cure_process}(\Delta\alpha_i^t, \alpha_i^t, T_i^t, T_{i-1}^t, T_{i+1}^t)$ [Eq. (4.7)];

$[E_{r_i}^{t+1}, G_{r_i}^{t+1}, \nu_{r_i}^{t+1}] = \text{Constitutive_model}(\alpha_i^{t+1}, T_i^{t+1});$

$[[K]_i^{t+1}] = \text{Build_stiffness_matrix}(\text{fibre_orient}(i), E_{r_i}^{t+1}, G_{r_i}^{t+1}, \nu_{r_i}^{t+1});$

$[\Delta\varepsilon_i^{ch,t+1}] = \text{Chemical_strain_increment}(\Delta\alpha^t);$

$[\Delta\varepsilon_i^{th,t+1}] = \text{Thermal_strain_increment}(\Delta T_i^t);$

$[\Delta\varepsilon_i^{Pr,t+1}] = \text{Process-induced_strain_incr}(\Delta\varepsilon_i^{th,t+1}, \Delta\varepsilon_i^{ch,t+1});$

$[\Delta\sigma_i^{Pr,t+1}] = \text{Process-induced_stress_incr}(\Delta\varepsilon_i^{Pr,t+1}, [K]_i^{t+1})$ [Eq. (3.75)];

$[\Delta N_i^{t+1}, \Delta M_i^{t+1}] = \text{Effective_load_incr}(\Delta\sigma_i^{Pr,t+1}, z_i)$ [Eq. (3.78-3.79)];

end

$[\varepsilon_0^{t+1}, \kappa^{t+1}] = \text{Laminate_deformation}(\Delta N_i^{t+1}, \Delta M_i^{t+1}, [K]_i^{t+1})$ [Eq. (3.64)];

$[\Delta\sigma^{t+1}] = \text{Ply_stress_increments}(\varepsilon_0^{t+1}, \kappa^{t+1}, \Delta\sigma_i^{Pr,t+1})$ [Eq. (3.76)];

 Compute residual stress $\sigma^{t+1} = \sigma^t + \Delta\sigma^{t+1};$

end

In the following section, this framework was verified through a case study on an UD laminates, the through-thickness residual stresses of which were investigated and compared with the results presented by Bogetti and Gillespie Jr (1992).

4.3 Framework Verification

4.3.1 Model Description

The laminate lay-up and fibre orientation were illustrated in Figure 4.1. The specimen was unidirectional laminated, consisting of CYCOM 4102 polyester resin and E-glass fibre reinforcement with a 54% fibre volume fraction. The nominal thickness of a single ply is 0.85mm. The thermal and mechanical properties of the polyester and glass fibre were taken from Bogetti and Gillespie Jr (1992), summarised in Table 4.1.

In this study, stress relaxation was neglected, the Young's modulus of the resin was

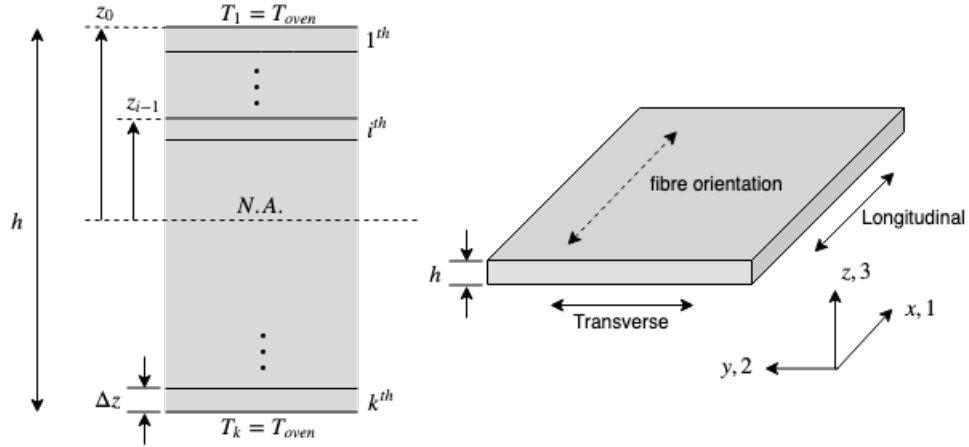


Figure 4.1: Schematic of the unidirectional-reinforced laminate

Properties	[Unit]	E-glass fibre	Polyester
ρ	[kg/m ³]	1890	
C_p	[J/(W°C)]	1260	
k_z	[W/(m°C)]	0.2163	
ν		0.22	0.4
E	[MPa]	73100	Eq. (4.8)
G	[MPa]	29900	Eq. (4.9)
α^{cte}	[1/°C]	5.04×10^{-6}	72.0×10^{-6}

Table 4.1: Material properties of E-glass fibre and polyester resin

proportional to the Degree-of-Cure, hence can be linear expressed in-between the uncured resin $E_r^0=2.757$ MPa and fully cured resin $E_r^\infty =2757$ MPa, given by

$$E_r = (1 - \alpha)E_r^0 + \alpha E_r^\infty. \quad (4.8)$$

The shear modulus of the resin was expressed as

$$G_r = \frac{E_r}{2(1 + \nu_v)}. \quad (4.9)$$

The chemical shrinkage was determined by applying Eq. (3.70) and Eq. (3.71), where the specific total volumetric shrinkage of resin V_{sh}^T was 6%.

The autocatalytic cure kinetic model used in this analysis was given in Eq. (3.10), rewritten here as

$$\frac{d\alpha}{dt} = A \cdot \exp\left[\frac{-E_a}{RT}\right] \alpha^m \cdot (1 - \alpha)^n, \quad (4.10)$$

where the cure kinetics parameters were given in Table 4.2.

Parameters	[Unit]	Polyester
m		0.524
n		1.476
A	[s ⁻¹]	6.167E20
E_a	[J/mol]	1.674E5
H_r	[J/kg]	7.75E4

Table 4.2: Cure kinetics parameters

This model is valid based on the following assumptions:

1. The dominant heat flow is assumed in the through-thickness direction so that in-plane heat diffusion is neglected
2. The viscosity of the resin is assumed to be constant so that any viscosity-related effects, such as viscous dissipation, are neglected
3. The Kirchhoff's plate theory is applied in describing the mechanical behaviour of the laminate plate, so that the through-thickness shear strain is neglected

4.3.2 Resin Modulus and Chemical Shrinkage

The development of the resin modulus and the chemical shrinkage were evaluated under an isothermal cure at 100°C. Figure 4.2a shows the isotropic stiffness of the resin and the effective transverse modulus under an isothermal cure.

The chemical shrinkage strain under the isothermal cure is presented in Figure 4.2b. It was observed that the longitudinal shrinkage strain was negligible due to fibre constraints. While in the transverse direction, the chemical shrinkage cannot be

4.3. FRAMEWORK VERIFICATION

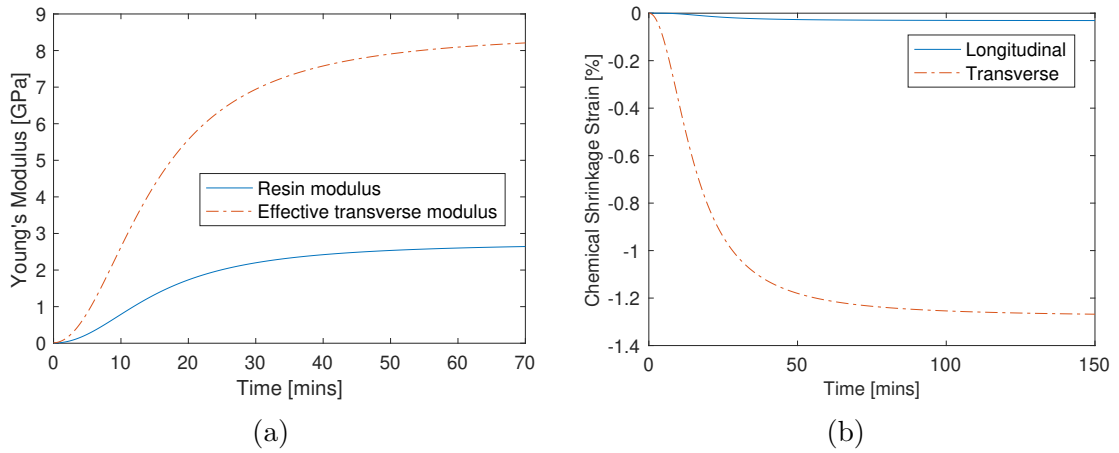


Figure 4.2: Prediction of the (a) resin modulus and (b) chemical shrinkage under an isothermal cure at 100°C

neglected. The specific total volumetric shrinkage (V_{sh}^T) of 6% leads to a transverse resin shrinkage of 1.2%.

4.3.3 Temperature and DoC Evolution

As the laminates going through an autoclave cure cycle, the evolution of the temperature and the degree of cure through the thickness of the laminates were investigated.

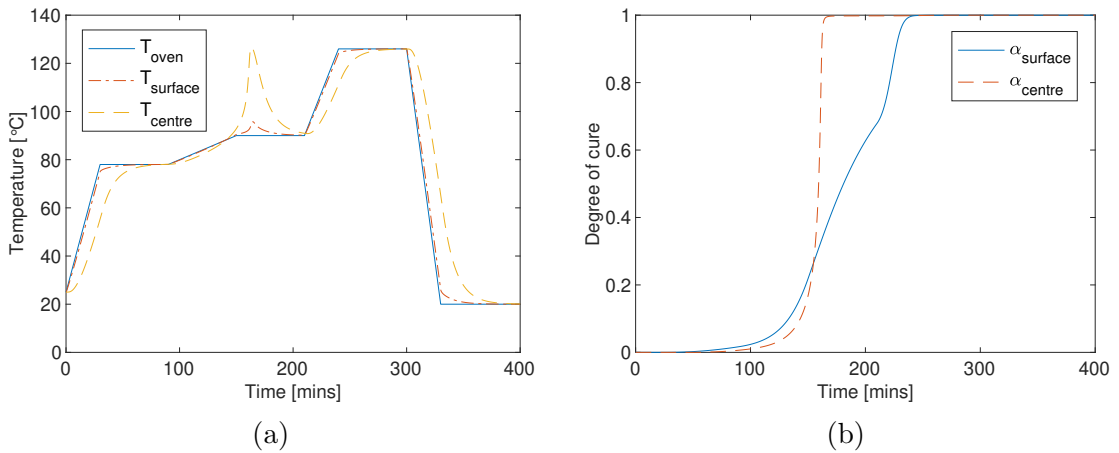


Figure 4.3: (a) The temperature and (b) the curing evolution under the autoclave cure cycle for the laminates with 25.4 mm thickness

Figure 4.3 shows the temperature and DoC evolution at the mid and surface layers of the laminate with a thickness of 25.4mm. A clear overshoot in temperature at the centre of the laminates was observed at the time=164 mins, shown in Figure

4.3a. The sudden rise in the temperature came from the exothermic reaction of the cross-linking during polymerisation. Due to poor thermal conductivity of polyester, excessive heat was generated and trapped within the central zone. Such temperature variation through the thickness of the laminate caused variation in the Degree-of-Cure. Consequently, residual stresses was developed within the laminated structure, which is undesirable in the engineering practice.

4.3.4 Thickness Effect on Residual Stresses

As mentioned in the previous section, a temperature overshoot was observed at time = 164 mins during the autoclave cure cycle. In this section, the investigation expanded to the temperature gradients of laminates with various thickness. The temperature and DoC distributions of laminates with thin to thick thickness are shown in Figure 4.4.

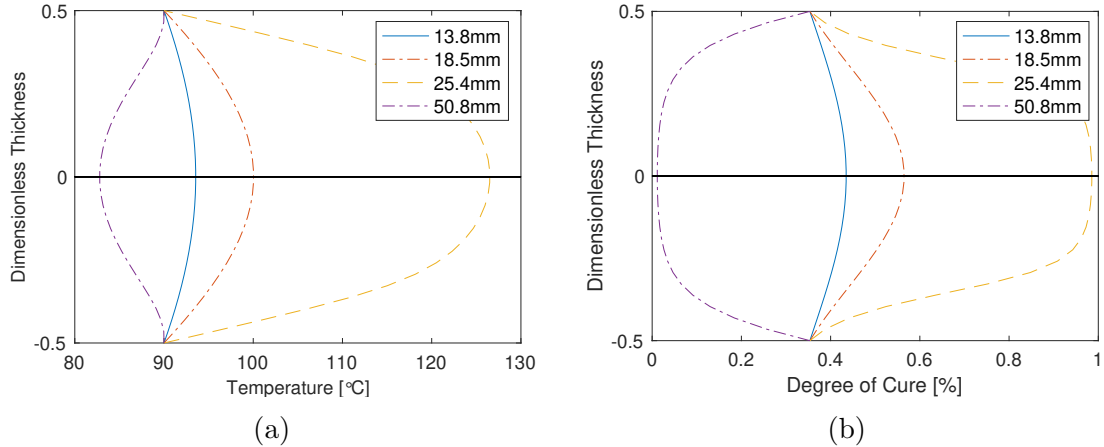


Figure 4.4: The through-thickness distribution of (a) the temperature and (b) the DoC in the laminate at curing time=164 mins

Figure 4.4a shows that for thin laminates, i.e. $t=13.8$ mm, the variation in the temperature distribution is negligible. As thickness increases, the effect of the internal heat generation is more pronounced. For the laminates with thickness $t=25.4$ mm, the temperature gradient from the surface to the centre of the laminate is substantial. Such temperature gradient also corresponds to the DoC gradient, as shown in

Figure 4.4b. For the case of $t=25.4$ mm, the DoC gradient is also the most severe. At this time step, while the surface DoC was around 0.36, the interior of the laminate was essentially fully cured.

Conversely, for the extra thick laminates, i.e. $t=50.8$ mm, the curing of the resin was delayed in the centre compared with that at surfaces. In fact, the curing has not yet started in the central zone of the laminate at curing time = 164 mins. As time advances, the interior of the 50.8 mm laminate began to cure and a reversed cure gradient was developed.

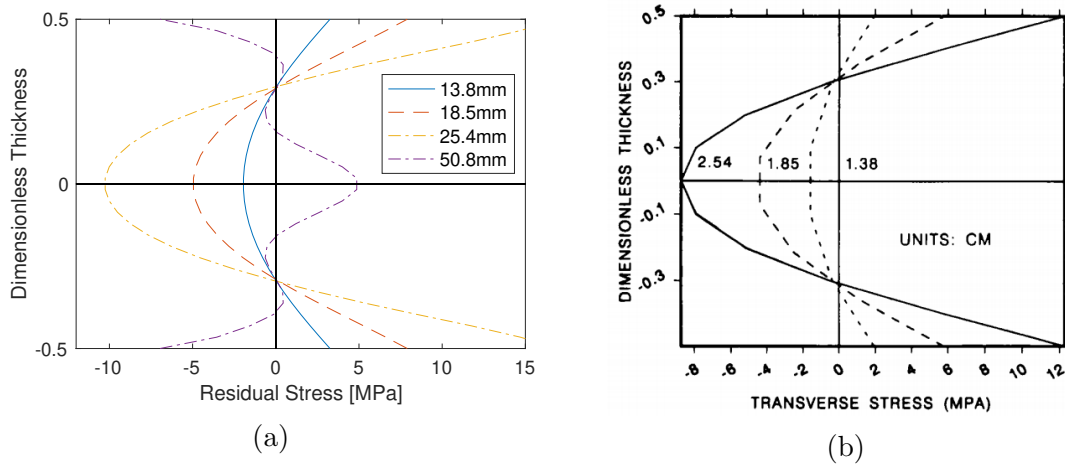


Figure 4.5: The transverse residual stresses distribution from (a) the Matlab model prediction and from (b) Bogetti and Gillespie Jr (1992)

The in-plane transverse residual stresses distributions for various laminate thicknesses are shown in Figure 4.5a. The results obtained using the computational framework are in good agreement with the results presented in Bogetti and Gillespie Jr (1992), shown in 4.5b. The residual stresses distributions for the laminate with 13.8 mm, 18.5 mm and 25.4 mm thickness exhibit a parabolic shape. This is a typical envelope for laminates cured from interior to exterior. As the central zone cures first, the resin is able to contract due to the chemical shrinkage effect. While the resin in the exterior regions are less able to contract due to the presence of cured part with higher stiffness at the middle zone, thus the compressive stresses are developed in the interior regions and the tensile stresses are developed at the

exterior regions. In contrast, the transverse stress distribution for 50.8mm thick laminate exhibits a reversed parabola at the central zone, which indicates that the resin cures from outside to the inside. The residual stresses are in self-equilibrium due to no boundary constraints applied in the model.

4.3.5 Cure Cycle Effect on Residual Stresses

The influence of autoclave cure cycle on the residual stresses development was also investigated here. A range of heating-up ramps of $0.25^{\circ}\text{C}/\text{min}$, $0.5^{\circ}\text{C}/\text{min}$ and $1.0^{\circ}\text{C}/\text{min}$ were chosen. In this particular case of glass fibre reinforced polyester composites, a fast heating-up ramp of $1.0^{\circ}\text{C}/\text{min}$ resulted in a reverse through-thickness residual stresses compared with that under slower heating-up ramp, as illustrated in Figure 4.6b. This is due to reverse temperature gradients in the through-thickness direction. Under fast heat-up cure cycle, the thermal load passing from the boundary to the middle of the laminate was delayed due to the low thermal conductivity of the resin. It is also worth noticing that a stress-free state could be obtained in-between these two bounds. This study also indicates that for thick laminate, minimum residual stresses could be achieved through careful design of cure cycle, particular with a precise control of ramp ratio.

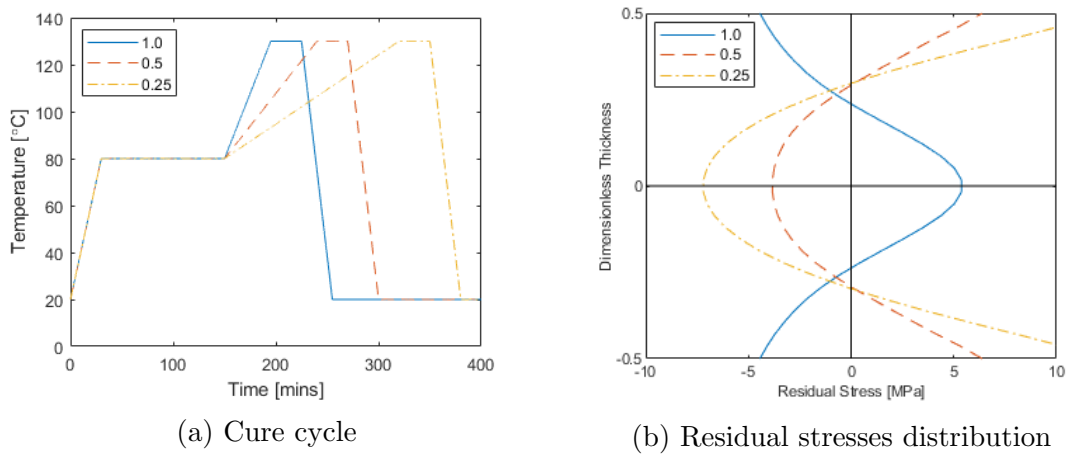


Figure 4.6: Residual stresses distribution of the 25.4 mm thick laminates under heating-up ramps of 0.25 , 0.5 and $1.0^{\circ}\text{C}/\text{minute}$

4.4 1D Modelling of IM7/8552 Laminates

In the following chapters, epoxy resin system 8552 will be employed both numerically and experimentally. Therefore, in this section, the temperature profiles in the through-thickness direction of 8552-based laminates under different cure cycle were investigated. The laminate lay-up and fibre orientation has been presented earlier in Figure 4.1. The single ply thickness is 0.19 mm. The fibre volume fraction was 57.7% and the laminate density was 1570 kg/m³. The aim of this study is to reveal under certain scenarios that the MRCC might not be sufficient. Furthermore, the MRCC is a rather conservative cure cycle, MRCC optimisation could be achieved at the design stage to improve manufacture efficiency, particular for thin laminates.

4.4.1 Material Properties of IM7/8552 Laminates

The cure kinetics of resin 8552 has been mentioned in Section 3.3.1. The cure kinetics model used in this study can be found in Eq.(3.82). A summary for the cure kinetics parameters used in this analysis were repeated below in Table 4.3.

Constants	[Unit]	Value	Comments
H_T	[J/kg]	574000	Total heat of reaction
E_a	[J/mol]	65000	Activation energy
A	[s ⁻¹]	70000	Pre-exponential cure rate coefficient
m	[/]	0.5	First exponential constant
n	[/]	1.5	Second exponential constant
R	[J/mol/K]	8.314	Gas constant
C	[/]	30	Diffusion constant
α_{C0}	[K ⁻¹]	-1.5148	Critical DoC at T=0K
α_{CT}	[/]	5.171×10^{-3}	Constant accounting for temperature dependence

Table 4.3: Constants for 8552 cure kinetics model (Ersoy et al., 2005a)

The thermal properties, namely, the specific heat capacity and the through-thickness thermal conductivity were summarised in Table 4.4, where Saad et al. (2014) presented a linear relationship between the thermal properties and the temperature.

In the mechanical analysis, the expression of the CHILE constitutive model has

Temperature	Specific heat capacity (C_p)	Thermal conductivity (k_z)
25	857.41	0.84126
50	919.81	0.88184
75	986.83	0.92572
100	1058.35	0.97286
125	1130.99	1.02034
150	1203.78	1.06764
175	1289.75	1.12186

Table 4.4: Thermal properties of UD IM7/8552 laminates (Saad et al., 2014)

been discussed in section 3.1.3.2, the parameters used in which were listed in Table 3.2. The effective mechanical properties of IM7/8552 unidirectional laminates were calculated using self-consistent micromechanical field model (SCFM). The properties derived using SCFM were compared against the FE-based model (FEBM), given in Table 4.5.

Properties	[Unit]	SCFM		FEBM ^a	Measured ^b
		Rubbery	Glassy	Glassy	Glassy
E_{11}	[MPa]	159,258	161,634	161,000	164,000
$E_{22} = E_{33}$	[MPa]	162.9	10,542	11,380	12,000
$G_{12} = G_{13}$	[MPa]	41.0	5,229	5,170	
G_{23}	[MPa]	40.8	3,542	3,980	
$\nu_{12} = \nu_{13}$	[-]	0.373	0.32	0.32	
ν_{23}	[-]	0.996	0.48	0.436	

^a OBrien and Krueger (2001)

^b Provided in Hexcel data sheet

Table 4.5: Effective mechanical properties of IM7/8552 unidirectional laminates using SCFM

The individual properties of fibre IM7 and resin 8552 are given in Table 4.6.

The coefficient of thermal expansion (CTE) and chemical shrinkage for IM7/8552 laminates are given in Table 4.7.

4.4.2 Boundary Conditions

The MRCC for 8552-based prepregs can be found in Hexcel datasheet (Hex, 2023). At the beginning of the process, 7 bar gauge autoclave pressure and full vacuum

4.4. 1D MODELLING OF IM7/8552 LAMINATES

Properties	[Unit]	IM7 ^a	8552 ^b		Comments
			Uncured	Cured	
E_{11}	[MPa]	27,6000	4.67	4,670	Longitudinal Young's modulus
$E_{22} = E_{33}$	[MPa]	19,500	4.67	4,670	Transverse Young's modulus
$G_{12} = G_{13}$	[MPa]	27,000	11	1,704	In-plane shear modulus
G_{23}	[MPa]	7,800	11	1,704	Transverse shear modulus
$\nu_{12} = \nu_{13}$	[-]	0.28	0.5	0.37	In-plane Poisson's ratio
ν_{23}	[-]	-	0.5	0.37	Transverse Poisson's ratio

^a Kaddour and Hinton (2012)

^b Ersoy et al. (2010a)

Table 4.6: Mechanical properties of IM7 fibre and 8552 resin

Properties	[Unit]	Rubbery	Glassy	Comments
α_{11}^t	$[\mu\epsilon/^\circ\text{C}]$	-	-0.1	Longitudinal CTE
α_{22}^t	$[\mu\epsilon/^\circ\text{C}]$	-	31.0	Transverse CTE
α_{33}^t	$[\mu\epsilon/^\circ\text{C}]$	-	31.0	Through-thickness CTE
ϵ_{11}^c	[%]	0	-	Longitudinal CCS
ϵ_{22}^c	[%]	0.48	-	Transverse CCS
ϵ_{33}^c	[%]	0.48	-	Through-thickness CCS

Table 4.7: Thermal and chemical shrinkage for IM7/8552 laminates (Ratcliffe et al., 2013)

were applied. A temperature ramp of $1 - 3^\circ\text{C}/\text{min}$ were applied until the ambient temperature reaches $110^\circ\text{C} \pm 5^\circ\text{C}$, following which, the specimens dwell for 60 ± 5 minutes. A second temperature ramp and dwell were applied afterwards, where the specimens were heated up at a rate of $1 - 3^\circ\text{C}/\text{min}$ to $180^\circ\text{C} \pm 5^\circ\text{C}$, and held for 120 ± 5 minutes. The specimens were then cooled down at a rate of $2 - 5^\circ\text{C}/\text{min}$, until a target temperature of 60°C was reached. The pressure was then vented while the vacuum was still in place. At the end of the cure cycle, specimens were left to cool down to the room temperature.

4.4.3 Residual Stresses of IM7/8552 Laminates

Section 4.3 presented a study on E-glass/polyester laminates, which indicates that for thick laminates, there may exhibit temperature gradient in the through-thickness direction under MRCC. In this section, initial investigation was conducted on the

IM7/8552 laminates consisting 100 layers. A minimum heating up ramp of $1^{\circ}\text{C}/\text{min}$ and a cooling down rate of $5^{\circ}\text{C}/\text{min}$ were selected. The development of the temperature and DoC at the centre and the surface of the laminates under the selected MRCC were plotted in Figure 4.7. During the second temperature ramp, there is a continuous temperature gap between the surface and the centre of the laminates, resulting DoC gap so that the inner laminates vitrified earlier. The maximum temperature difference is approximately 5°C .

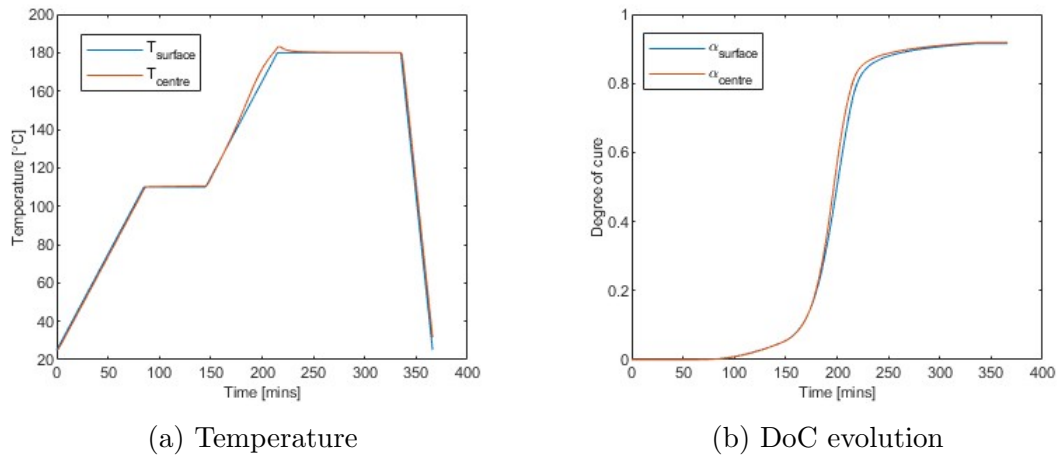


Figure 4.7: (a) Temperature and (b) DoC evolution at the centre and the surface of the laminates under MRCC

Furthermore, the temperature and DoC profile for thin laminates were also investigated. For a laminates consisting 16 plies, the study found that the MRCC is a rather conservative cure profile. The heat-up ramp can be designed higher than the manufacture recommended ramp value without incurring temperature gradient. Therefore, a cure cycle optimisation could potentially be applied when manufacturing thin laminates. A comparison of the transverse residual stresses of both thick (100 layers) and thin (16 layers) laminates were presented in Figure 4.8.

For the thin laminates, there exists little DoC gradient in the through-thickness direction, resulting in maximum residual stresses less than 0.5kPa. While for the thick laminates, the residual stresses caused by DoC gradient is non-negligible. The maximum tensile residual stresses at the laminate surfaces was up to 23.9 kPa and

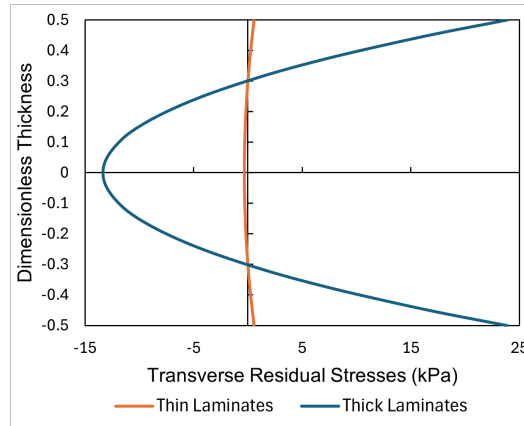


Figure 4.8: The transverse residual stresses distributions of thick and thin laminates

the maximum compressive residual stresses at the centre of the laminates was 13.4 kPa. Unlike temperature and chemical shrinkage induced residual stresses, those cure cycle induced residual stresses can and should be avoided in the manufacturing process. In the following chapters, the cure cycle for manufacturing specimens was carefully chosen so that no DoC gradient was observed in the modelling stage.

4.5 Summary

This chapter introduced a Matlab model of predicting process-induced residual stresses of flat laminates. The presented model was validated by comparing to the results presented by Bogetti and Gillespie Jr (1992). Parametric investigation was undertaken to explore the effects of thickness and autoclave cure cycle on the formation of temperature and DoC gradient, which subsequently resulting in residual stresses. The study highlighted that for either thin or thicker laminates, the effectiveness of the MRCC should be evaluated before implementing.

The study looked into the temperature and DoC distributions across the thickness of IM7/8552 laminates. Notably, the study found that the manufacturing recommended cure cycle may not be valid for thick laminates. Furthermore, an optimised cure cycle could be designed for thin laminates to improve manufacturing efficiency.

This Matlab model served as a verification of subroutines in the ABAQUS model, which will be discussed in the next chapter. It also serves as a good tool to quickly predict the effectiveness of the designed autoclave cure cycle for relatively simple laminated structures.

Chapter 5

3D Modelling of Spring-in in Curved Laminates

5.1 Overview

In the previous chapter, a 1D thermal-chemical-mechanical modelling of cure process based on CLT was presented. Although such model offers a good estimation in the residual stresses distribution across the through-thickness direction of laminates, it soon reaches its limitation when more complex geometry or boundary conditions are imposed, as would be expected in real engineering practice. In this chapter, a curved part was selected as a starting point to develop a modelling framework for any given composite structure.

The simulation of composite structures with complex geometries requires a CAE tool that is computationally powerful enough to tackle such challenges. In this chapter, 3D modelling using ABAQUS/Standard was presented. ABAQUS offers rigorous finite element analysis as well as allowing users to implement their own functions and parameters that fit to individual's purpose. A detailed workflow of

coupled thermal-chemical-mechanical analysis in ABAQUS is introduced in Section 5.2. Having exploited the necessary simulation tools, a model description of the curved laminates is presented in Section 5.3. The process-induced distortion predicted by the current model was validated against the experimental findings from the literature. Following that, the spring-in angle with respect to the geometric features including thickness, radius and various lay-ups, are investigated in Section 5.4.

5.2 Numerical Implementation in ABAQUS

In this study, the thermal-chemical analysis and mechanical analysis were sequentially coupled. In the thermal-chemical analysis, an internal heat generation term was incorporated to account for exothermic chemical reaction. Temperature and Degree-of-Cure (DoC) fields were updated at each time increment until the analysis reached the end of the Manufacturing Recommended Cure Cycle (MRCC). In the mechanical analysis, process-induced thermal and chemical strains were to be determined from the temperature and DoC history field. At each time increment, the effective laminate mechanical properties were updated to compute the residual stress and displacement field at the end of analysis. In this study, a CHILE constitutive model was employed. The workflow of the thermal-chemical and mechanical analysis was illustrated in Figure 5.1.

ABAQUS provides a variety of functions powered by its non-linear computational ability. It allows great flexibility in introducing customised functions, such as material constitutive behaviours or non-uniform boundary conditions, through so-called user-subroutines. Currently ABAQUS/Standard provides 64 user subroutines, in the simulation of cure process, four of them will be implemented, namely USDFLD, HETVAL, UEXPAN and UMAT. A framework of modelling procedure with participation of each user subroutine is illustrated in Figure 5.2. USDFLD allows the

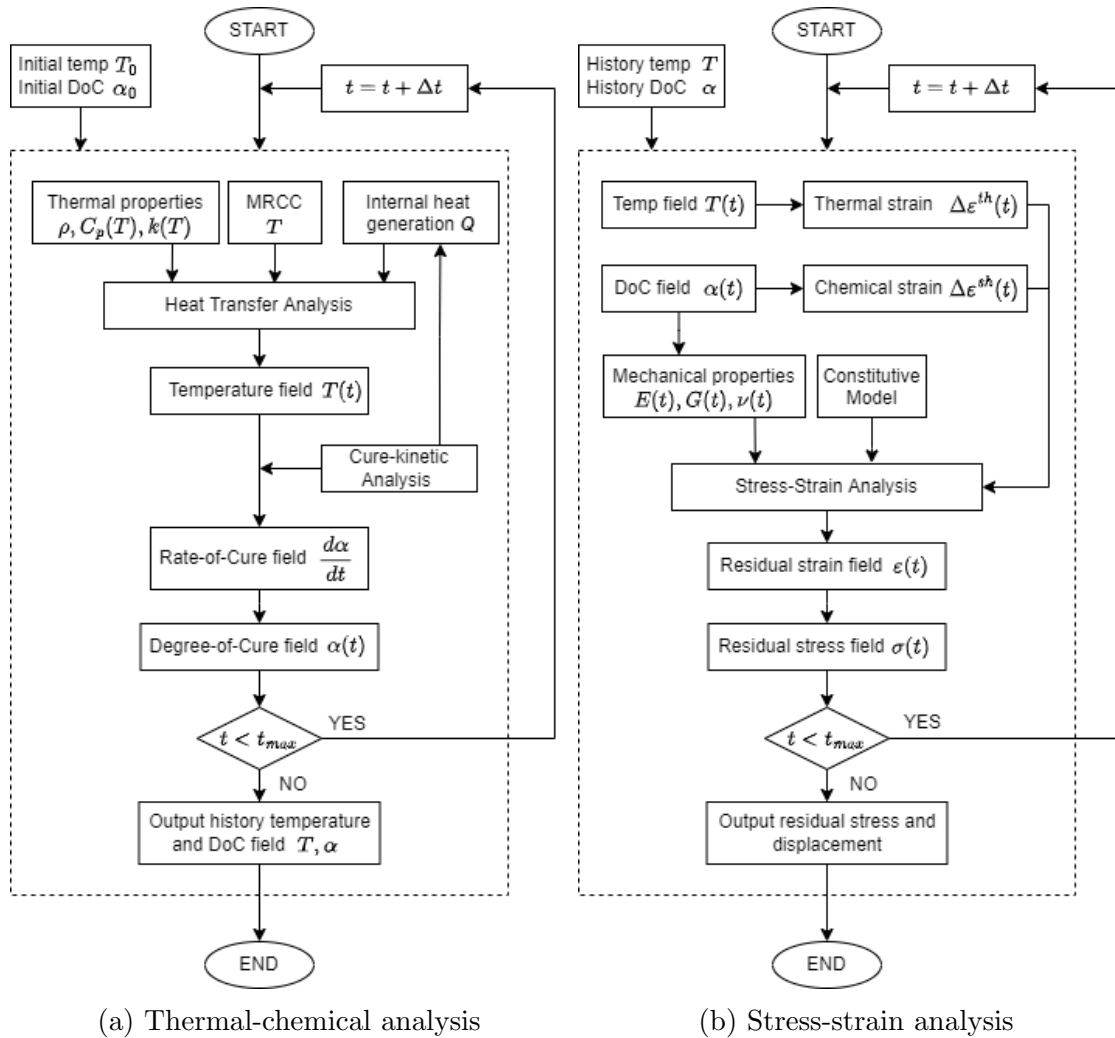


Figure 5.1: Computation flowchart for sequentially coupled thermal-chemical-mechanical analysis in ABAQUS

users to define field variables at a material point, it also provides the users with solution-dependent state variables through which information could be passed and updated in-between different subroutines. User is also allowed to access material point data through a utility routine GETVRM, where in the case of cure-kinetics analysis, the temperature degree-of-freedom at each material point are obtained. A fully-coupled thermal-chemical analysis using USDFLD in conjunction with HETVAL is illustrated in Figure 5.3, where heat generation from exothermic chemical reaction is implemented in HETVAL.

The incremental thermal and chemical strains are defined in user-subroutine UEX-

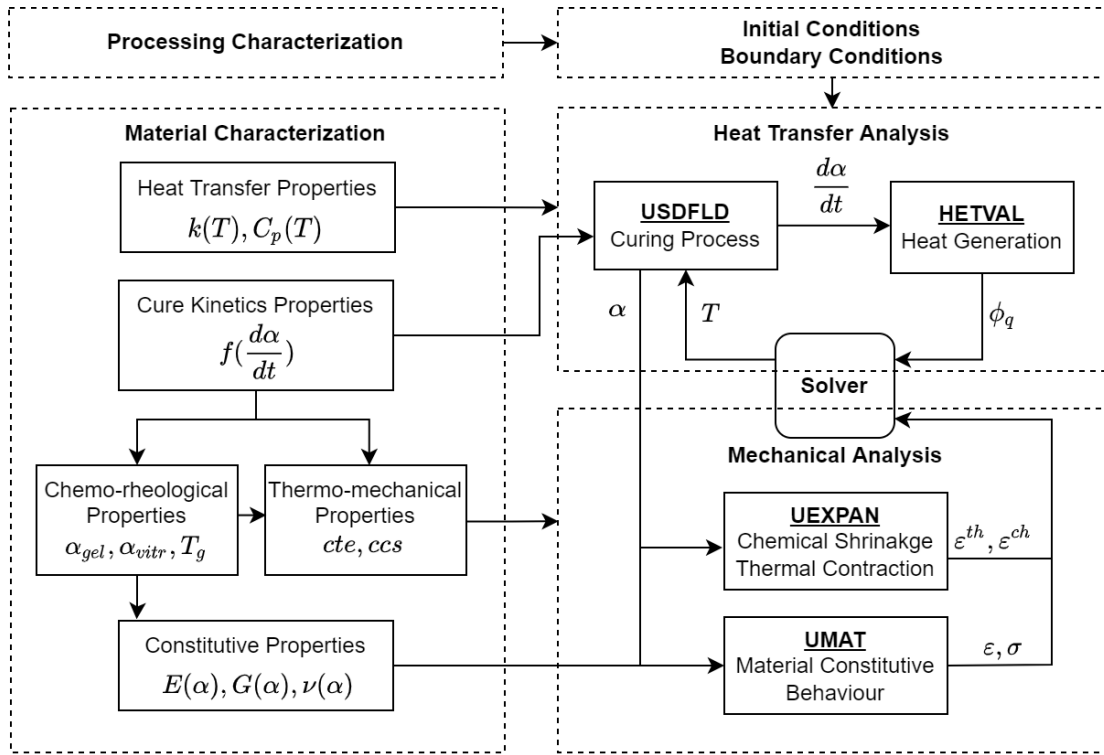


Figure 5.2: Modelling framework including user-subroutines

PAN, where the incremental thermal strains are expressed as the function of temperature and similarly, the incremental chemical strains are expressed as the function of DoC.

The UMAT subroutine allows the users to define any specific material constitutive behaviour by expressing the stress σ and Jacobian matrix $\frac{\partial \sigma}{\partial \epsilon}$ at each integration point at each time increment. In this simulation practice, the Jacobian stiffness matrix is derived using the pseudo-viscoelastic constitutive model (CHILE), detailed in Section 3.1.3.2. The effective engineering properties for uncured and fully cured laminates are computed using the SCFM model, details see Section 3.1.2.2.

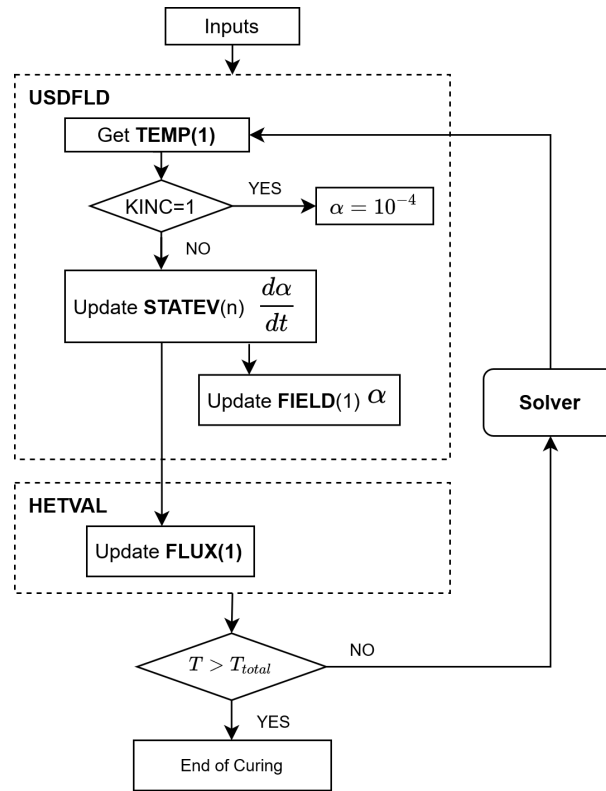


Figure 5.3: Framework of thermal-chemical analysis with user-subroutines USDFLD and HETVAL

5.3 3D Modelling of Curved Laminates

5.3.1 Model Description

In this section, curing of a 270° curved AS4/8552 laminates with unidirectional and cross-ply lay-up on the inner surface of a carbon-epoxy tube tool was modelled, the inner diameter of which is 50 mm, as depicted in Figure 5.4. Taking advantage of the symmetry, a 135° segment was analysed in ABAQUS. The spring-in angle derived from the simulation is half of the total spring-in. Certain assumptions are imposed such as the tool-part interaction is neglected given that the tool was made of carbon-epoxy, there is little difference in CTEs between the tool and the part. The part is assumed to be perfectly uniform without any voids or gradient of fibre volume fraction. The simulation is performed in two analyses steps, namely a coupled temperature-displacement analysis, corresponding to the autoclave cure process, and

a static analysis, representing the tool release. One element per ply is assigned in the through-thickness direction. An 8-node coupled-temperature-displacement solid element C3D8T was selected.

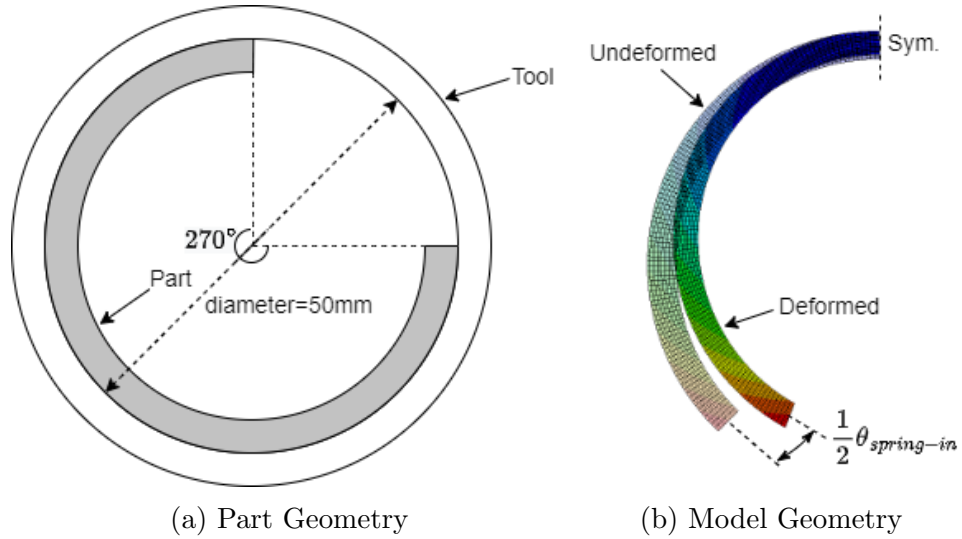


Figure 5.4: The geometry description of the curved part

The cure kinetics properties of resin 8552 have been mentioned in the previous chapter and the AS4/8552 laminate properties have been discussed in great details in Section 3.3.2. A summary for all the necessary parameters used in this analysis are listed below in Table 5.1, Table 5.2 and Table 5.3.

Constants	[Unit]	Value	Comments
H_T	[J/kg]	574000	Total heat of reaction
E_a	[J/mol]	65000	Activation energy
A	[s^{-1}]	70000	Pre-exponential cure rate coefficient
m	[/]	0.5	First exponential constant
n	[/]	1.5	Second exponential constant
R	[J/mol/K]	8.314	Gas constant
C	[/]	30	Diffusion constant
α_{C0}	[K^{-1}]	-1.5148	Critical DoC at T=0K
α_{CT}	[/]	5.171×10^{-3}	Constant accounting for temperature dependence

Table 5.1: Constants for 8552 cure kinetics model (Ersoy et al., 2005a)

Properties	[Unit]	Uncured	Cured
E_{11}	[MPa]	130000	132400
$E_{22} = E_{33}$	[MPa]	154	9224
$G_{12} = G_{13}$	[MPa]	40.1	5163
G_{23}	[MPa]	39.5	3127
$\nu_{12} = \nu_{13}$	[-]	0.328	0.268
ν_{23}	[-]	0.954	0.475

Table 5.2: Effective mechanical properties of AS4/8552 unidirectional laminates using SCFM

Properties	[Unit]	Rubbery	Glassy	Comments
α_{11}^t	$[\mu\epsilon/^{\circ}\text{C}]$	-	0	Longitudinal CTE
α_{22}^t	$[\mu\epsilon/^{\circ}\text{C}]$	-	32.6	Transverse CTE
α_{33}^t	$[\mu\epsilon/^{\circ}\text{C}]$	-	32.6	Through-thickness CTE
ϵ_{11}^c	[%]	0	-	Longitudinal CCS
ϵ_{22}^c	[%]	0.48	-	Transverse CCS
ϵ_{33}^c	[%]	0.48	-	Through-thickness CCS

Table 5.3: Thermal and chemical shrinkage for unidirectional AS4/8552 prepregs

5.3.2 Boundary Conditions

The thermal boundary conditions follow the MRCC, which consists of a first ramp of 2°C/min up to 120°C, the first dwell at 120°C for 1 hour, the second ramp of 2°C/min up to 180°C and the second dwell at 180°C for 2 hours. A pressure of 0.7 MPa was applied throughout the cure process. The ambient temperature was assumed to be 20°C. Surface film conditions were applied at the tool side and vacuum bag side of the laminates, to account for the heat transfer from autoclave temperature to part surface through convection. The effective film coefficients (Johnston, 1997) for an aluminium tool side and a vacuum bag side are given below:

$$h_{\text{tool-side}} = 15.9 + 5.94 \times 10^{-5} \times P \quad (5.1)$$

$$h_{\text{vacuum-side}} = 45.6 + 1.31 \times 10^{-4} \times P \quad (5.2)$$

where P is the autoclave pressure of 0.7MPa, modelled as a surface pressure on the

vacuum bag side.

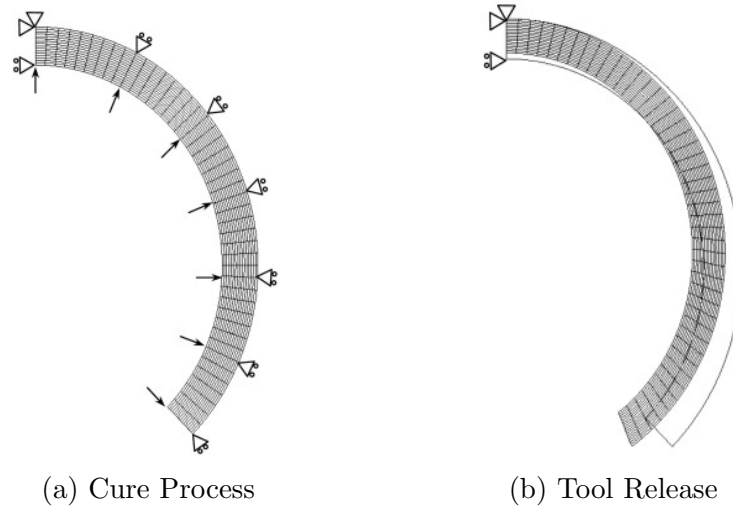


Figure 5.5: Boundary conditions for the two-step analysis of the curved part (Ersoy et al., 2010b)

Taking advantage of the symmetric geometry, displacement normal to the symmetric plane is restrained to reduce computational efforts. As shown in Figure 5.5, sliding boundary condition was applied at the outer surface (tool side) of the curved part, i.e. tool-part interaction is neglected. Once the cure process is complete, the sliding constraints are released, so are the residual stresses in the curved part, causing spring-in deformation.

5.3.3 Temperature and DoC Distribution Prediction

A reliable prediction on the final deformation requires firstly, an accurate distribution prediction on temperature or DoC field under MRCC. Figure 5.6 shows the development of temperature at the mid-layer, the glass transition temperature of the resin, and the DoC evolution under MRCC. This example is a cross-ply laminates consisting a total of 16 plies. Temperature overshooting up to 192°C was observed at the end of the second temperature ramp, during which, the cure rate reaches its maximum, generating excessive heat. Such thermal energy was temporarily trapped within the laminates due to the poor thermal conductivity of the epoxy

itself. Looking at the laminate with relatively thin thickness, results show that a curved part consisting of 4 plies does not have noticeable temperature overshooting. The maximum temperature observed was 182.5°C . Although temperature gradient is not significant even in the case of 16-ply, the thicker laminate would require further adjustment on the MRCC without provoking severe stress gradients in the final product.

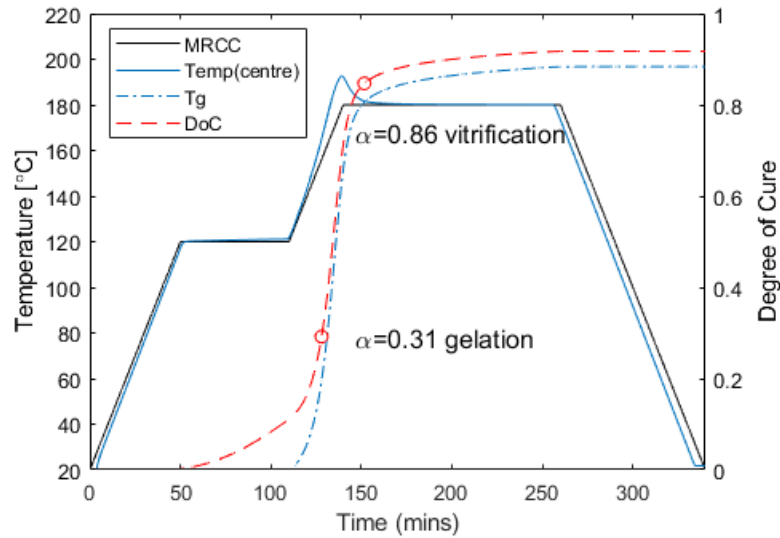


Figure 5.6: DoC and temperature evolution of resin 8552 under MRCC

Recognising the status change of the resin as it goes through cure cycle is equivalently as important as predicting the DoC. Initially, resin behaves as viscous fluid and cannot sustain any stresses. As resin undergoes cure cycle, the viscosity of the resin increases, until it reaches a point of gelation where the resin transforms from a liquid state to a rubbery state. Determining the DoC of the gelation point is therefore crucial for modelling the resin status evolution.

Hubert et al. (2001) reported a DoC at gelation of resin 8552 to be 0.47, which was estimated from viscosity tests using parallel plate rheometer. However, Garstka et al. (2007) reported a lower DoC of 0.31 for resin 8552 at gelation, employing a ply pull-out technique developed by (Ersoy et al., 2005b). Their experiment found that from DoC=0.31, the inter-ply shear modulus of AS4/8552 laminates increased

dramatically. Their study has also found that the DoC at gelation is independent of curing temperature. In this work, the gelation DoC of 0.31 was chosen as the pull-out test better represent the real autoclave situation when compared to parallel plate rheometry apparatus.

As the temperature reaches glass transition temperature, resin is vitrified at $\alpha_{vitri} = 0.86$ and behave as stiff elastic material (Ersoy et al., 2005b).

5.3.4 Residual Stresses Prediction

Accumulating the stress increments from the point where resin passed its gelation point, the transverse in-plane stress distribution through thickness is presented in Figure 5.7, where the residual stresses at the resin vitrification point and at the end of the cure process were compared for the case of unidirectional and cross-ply laminates.

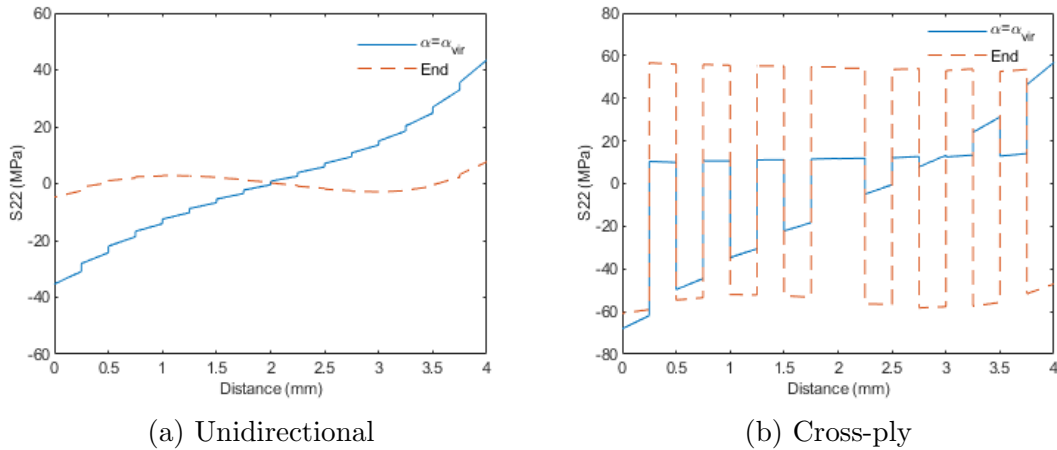


Figure 5.7: Transverse in-plane stress distribution through thickness of (a) UD and (b) cross-ply laminated C-section

The residual stress distribution from the modelling agrees well with the numerical results presented in Ersoy et al. (2010b), giving a good indication that the CHILE constitutive model works well in predicting distortion in a curved part. As shown in Figure 5.7a, before tool release, the in-plane tensile stress reached 43.5MPa on

the tool side and in-plane compression stress reached 35.3MPa on the vacuum bag side. The stresses were rearranged once the curved part was removed from the tool, leaving the maximum residual stress of 7.7MPa. In the case of the cross-ply laminates, shown in Figure 5.7b, the simulation predicted that as shear accumulated in $[0^\circ]$ orientation plies, no significant stresses developed perpendicular to the fibre direction. The stress distribution in $[0^\circ]$ orientation plies are very similar to that in the unidirectional laminates. However, once the constraints were lifted, the plies in both directions share a relatively equal residual stresses, a maximum tensile stress of 56.6 MPa was observed in the $[90^\circ]$ oriented plies and compressive stress of 60.8 MPa was observed in the $[0^\circ]$ oriented plies.

5.3.5 Spring-in Predictions

Table 5.4 and Table 5.5 give the spring-in angle comparison from the modelling and experimental validation, for the case of unidirectional laminated and cross-ply laminated composites respectively. The results, together with the illustrations given in Figure 5.8 and Figure 5.9, reveal a clear tendency in decreased spring-in angle with increasing laminate thickness. The results from modelling showed a good agreement with that from experiments published in Ersoy et al. (2010b). The discrepancy varying from 0 to 10%, with an average discrepancy of 4.1%, further demonstrating the successful implementation of the pseudo-viscoelastic constitutive material model and the overall predictive modelling framework for the curing process.

Thickness [mm]	No. of plies	Modelling	Experimental (Ersoy et al., 2010b)
1	4	1.05°	1.03°
2	8	0.85°	0.95°
3	12	0.74°	0.78°
4	16	0.68°	0.66°

Table 5.4: Comparison of the modelling and experimental results of the spring-in angle for UD laminated curved part

5.3. 3D MODELLING OF CURVED LAMINATES

Thickness [mm]	No. of plies	Modelling	Experimental (Ersoy et al., 2010b)
1	4	1.28°	1.28°
2	8	1.16°	1.18°
3	12	1.07°	1.09°
4	16	1.01°	0.93°

Table 5.5: Comparison of the modelling and experimental results of the spring-in angle for cross-ply laminated curved part

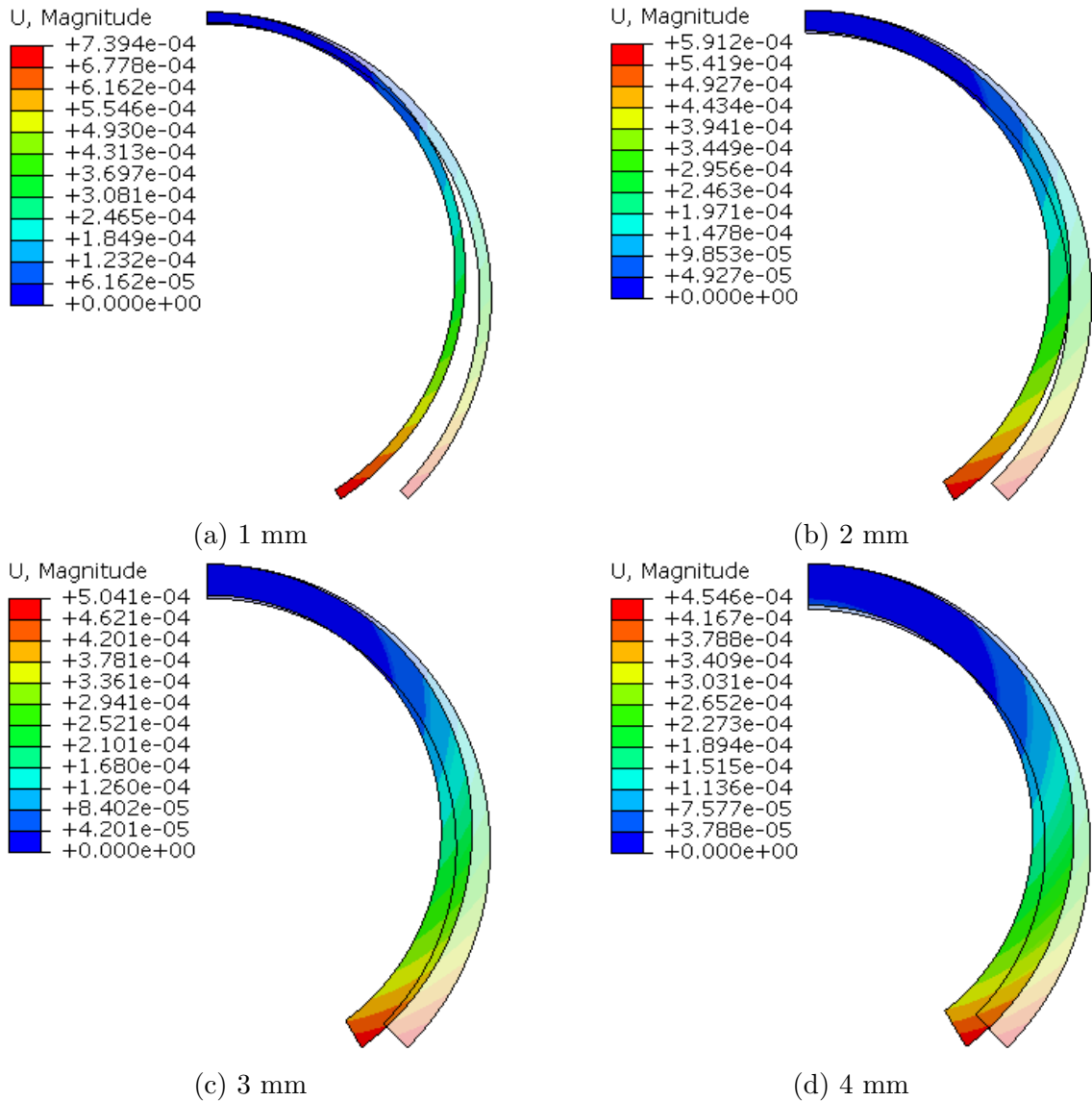


Figure 5.8: Spring-in deformation for UD laminated curved part with various thickness (unit=m, scale factor=8)

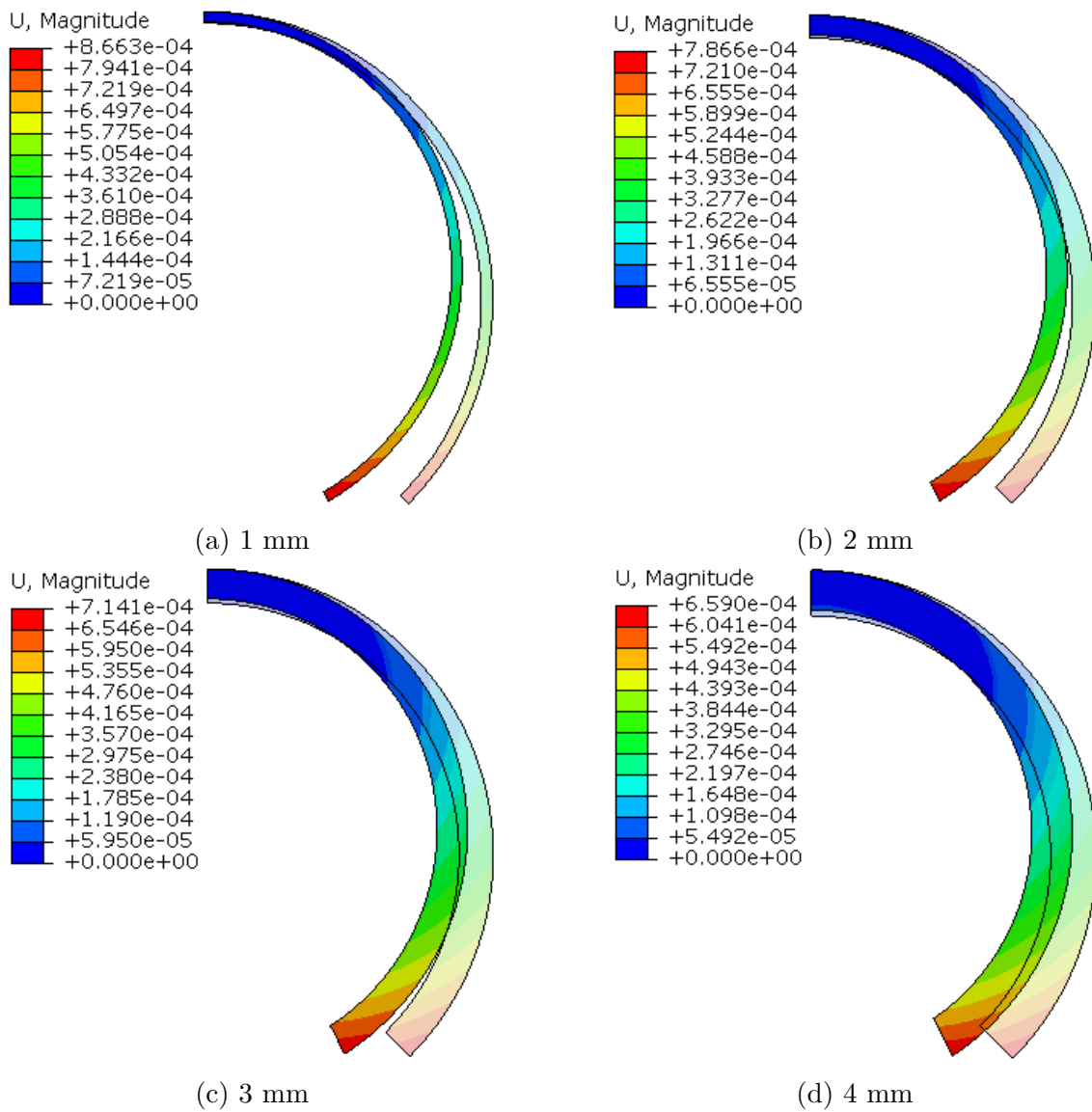


Figure 5.9: Spring-in deformation for cross-ply laminated curved part with various thickness (unit=m, scale factor=8)

5.4 Investigation of Geometry Effect on Spring-in

So far, one of the geometric features, i.e. thickness, has shown a clear impact on the spring-in angle of a curved part. To further explore the relevant factors contributing to the spring-in phenomenon, a parametric analysis was carried out to examine the effects of thickness, tool radius and lay-up sequence on the final deformation, as summarised in Table 5.6.

Thickness [mm]	Ply	Lay-ups	Radius [mm]	Stiffness D_{11} [Nmm]	U_{max} [mm]	Spring-in [θ°]
Effect of laminate thickness						
1	4	$[0/90]_s$	25	9,867	0.866	1.28°
2	8	$[0/90]_{2s}$	25	63,350	0.787	1.16°
3	12	$[0/90]_{3s}$	25	196,273	0.714	1.07°
4	16	$[0/90]_{4s}$	25	444,461	0.659	1.01°
Effect of tool radius						
2	8	$[0/90]_{2s}$	6	63,350	0.141	0.95°
2	8	$[0/90]_{2s}$	9	63,350	0.224	0.98°
2	8	$[0/90]_{2s}$	12	63,350	0.318	1.02°
2	8	$[0/90]_{2s}$	25	63,350	0.787	1.16°
Effect of lay-up sequence						
2	8	$[0/90]_{2s}$	25	63,350	0.787	1.16°
2	8	$[0/45/-45/90]_s$	25	63,190	0.787	1.16°
2	8	$[0/90/45/-45]_s$	25	57,007	0.790	1.20°
2	8	$[45/-45/90/0]_s$	25	26,741	0.645	0.93°

Table 5.6: Parametric analysis of different factors contributing to spring-in

With increasing tool radius varying from 6mm to 25mm, a clear increase in spring-in angle was observed for curved part with the same thickness (2 mm) and the same cross-ply lay-ups, illustrated in Figure 5.10. This phenomenon was further examined to see if the spring-in angle is linearly proportional to the ratio of arc length to the part thickness, regardless the thickness or radius of the laminate. Table 5.7 summarised the relationship between the arc-to-thickness ratio of the laminates and their corresponding spring-in angle. A clear tendency in increased spring-in angle was observed in Figure 5.11 with increased arc-to-thickness ratio.

In particular, this study found that laminates with nearly identical arc-to-thickness

ratio produce nearly equal spring-in angles. By comparing the 4mm thick laminates with 25 mm radius and the 2 mm thick laminates with 12 mm radius, their arc-to-thickness ratio is very close to each other. The spring-in angles predicted from these two configurations are also very close to each other, with a difference only up to 0.01°.

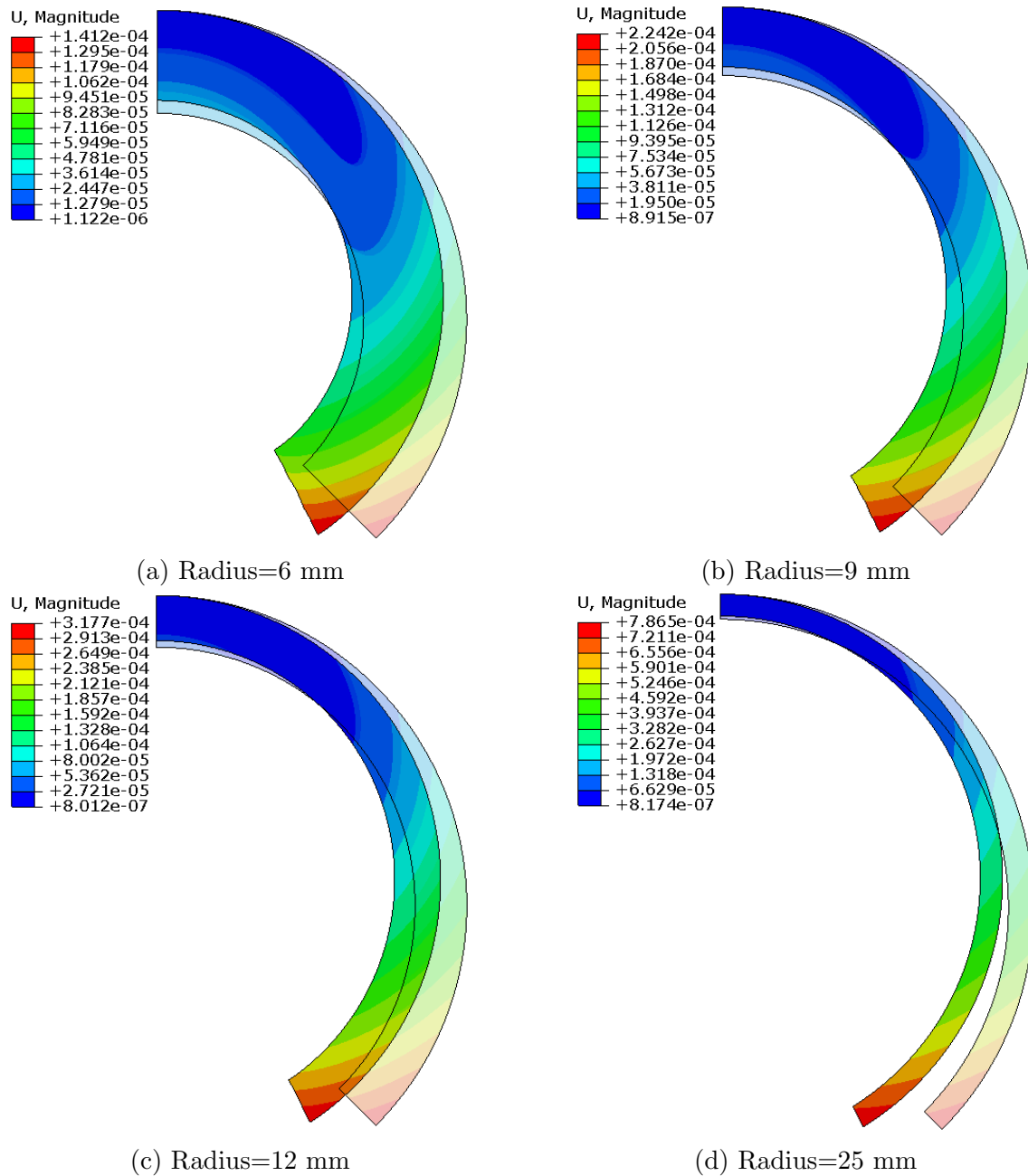


Figure 5.10: Spring-in deformation for cross-ply laminated curved part with various tool radius (unit=m, scale factor=8)

Thickness [<i>mm</i>]	Radius [<i>mm</i>]	Arc-to-thickness ratio	Spring-in [θ°]
Effect of laminate thickness			
1	25	58.9	1.28°
2	25	29.5	1.16°
3	25	19.6	1.07°
4	25	14.7	1.01°
Effect of tool radius			
2	6	7.1	0.95°
2	9	10.6	0.98°
2	12	14.1	1.02°
2	25	29.5	1.16°

Table 5.7: Arc-to-thickness ratio effect on spring-in angle

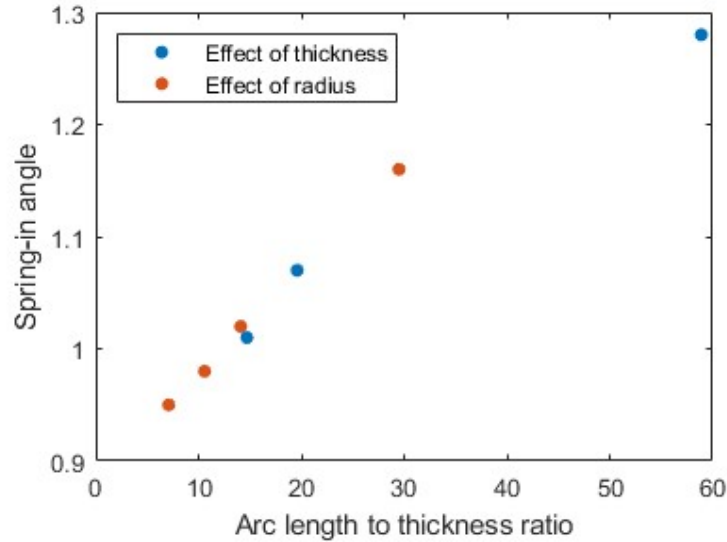


Figure 5.11: Arc-to-thickness ratio versus spring-in angle

Up to this point, it is reasonable to believe that spring-in deformation is linearly related to the longitudinal and transversal geometric features, namely, arc length and thickness. However, the underlying mechanism behind this phenomenon remains unclear. Additionally, the discussion has not yet covered the effects stemming from different lay-up sequences or bending stiffness. To gain further insight into the mechanism governing spring-in, shear-lag effect was investigated in the following section.

5.5 Investigation of Shear-lag Effect on Spring-in

Considering two limiting cases of spring-in of a curved part: 1) a material that is stiff in shear, would spring-in as residual stresses are released; 2) a material that is flexible in shear, no spring-in would occur as deformation is accommodated only by shear. The true behaviour of a resin between gelation and vitrification lies in-between. The shear deformation is illustrated in Figure 5.12, where shear-lag angle was denoted.

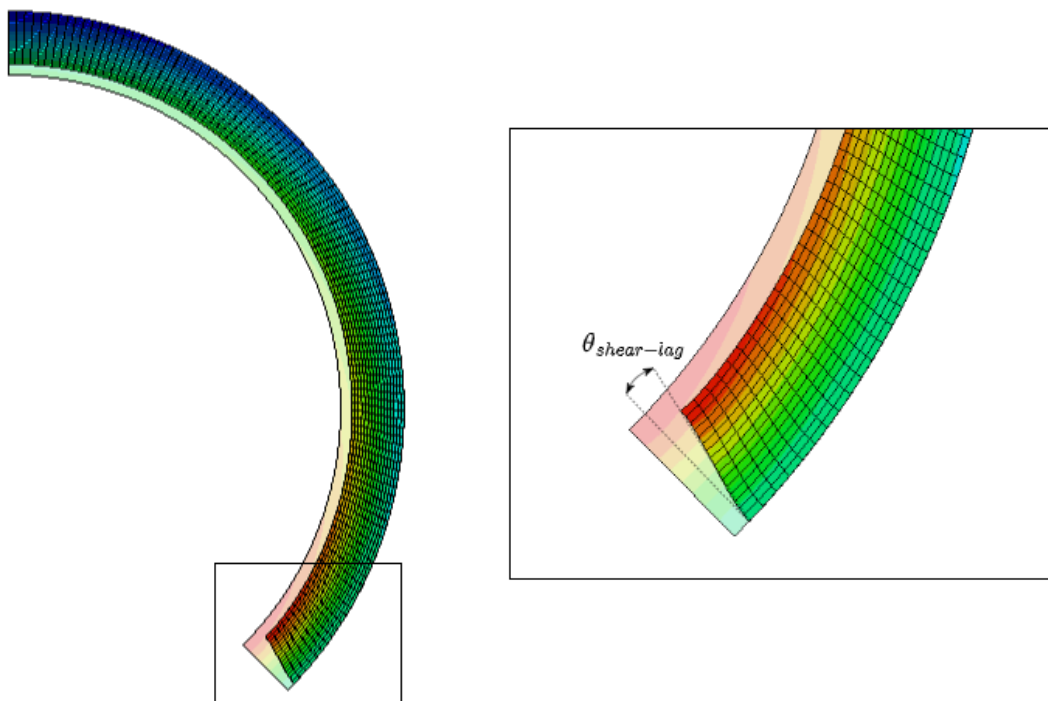


Figure 5.12: Shear-lag at resin vitrification point

This study has found that the shear-lag can have a significant impact on reducing spring-in angle. Spring-in angle was found to be smaller as the part arc length reduces or as the part thickness increases. Before resin reaches the glass transition temperature, shear modulus is relatively small, hence inter-ply slip occurred. Later on, shear modulus increases significantly while the resin still exhibits rubbery properties. As resin reaches its vitrification point, shear modulus reaches its maximum and can no longer accommodate inter-ply slip.

It was observed that shear-lag angle reached its maximum as resin reached its vitrification point. The maximum shear-lag angle for laminates with various geometric parameters are summarised in Table 5.8. As depicted in Figure 5.13, an increase in the shear-lag angle corresponded to a decrease in spring-in angle, regardless of factors such as part thickness, radius, unidirectional (UD) or cross-ply (XP) lamination.

Thickness [mm]	Ply	Lay-ups	Radius [mm]	Shear-lag angle [$\theta_{shear-lag}^\circ$]	Spring-in angle [$\theta_{spring-in}^\circ$]
Effect of laminate thickness (UD)					
1	4	[0] ₄	25	0.23°	1.05°
2	8	[0] ₈	25	0.41°	0.85°
3	12	[0] ₁₂	25	0.50°	0.74°
4	16	[0] ₁₆	25	0.55°	0.68°
Effect of laminate thickness (XP)					
1	4	[0/90] _s	25	0.17°	1.28°
2	8	[0/90] _{2s}	25	0.33°	1.16°
3	12	[0/90] _{3s}	25	0.47°	1.07°
4	16	[0/90] _{4s}	25	0.58°	1.01°
Effect of tool radius					
2	8	[0/90] _{2s}	6	0.70°	0.95°
2	8	[0/90] _{2s}	9	0.63°	0.98°
2	8	[0/90] _{2s}	12	0.56°	1.02°
2	8	[0/90] _{2s}	25	0.33°	1.16°
Effect of lay-up sequence					
2	8	[0/90] _{2s}	25	0.33°	1.16°
2	8	[0/45/ - 45/90] _s	25	0.31°	1.16°
2	8	[0/90/45/ - 45] _s	25	0.30°	1.20°
2	8	[45/ - 45/90/0] _s	25	0.05°	0.93°

Table 5.8: Parametric analysis of shear-lag effect on spring-in

When examining variations in lay-up sequence, and taking into account the individual effective stiffness values presented in Table 5.6, it was observed that laminates with relatively similar effective bending stiffness (varying from 57007 to 63350 Nmm), exhibited closely matching spring-in (1.16° to 1.20°) and shear-lag angles (0.33° to 0.30°). A noteworthy exception was the [45/ - 45/90/0]_s laminate, which displayed minimal shear-lag angle despite still exhibiting a spring-in angle of 0.93°. This anomaly may be attributed to its notably low stiffness, which contributed minimally to the shear-lag phenomenon.

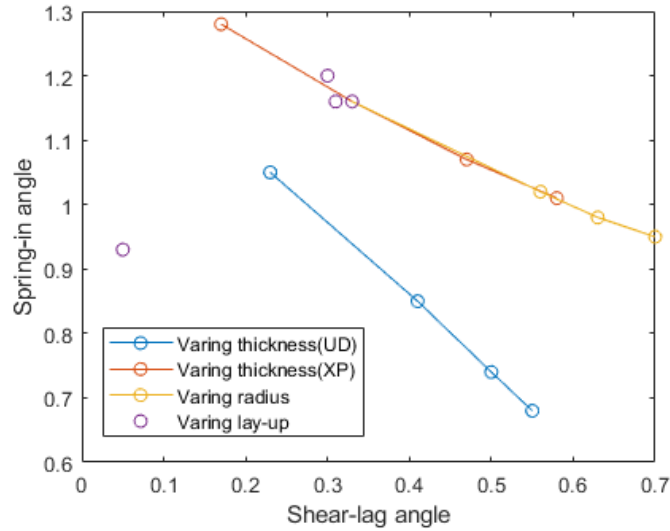


Figure 5.13: Shear-lag angle versus spring-in angle of the curved part

5.6 Summary

This chapter presented the development of a thermal-chemical-mechanical model that is capable of predicting process-induced residual stresses and distortions of a curved laminates. The model is validated against the experimental results presented in Ersoy et al. (2010b), with an average discrepancy of 4.1%.

This chapter provided a novel insight into the formation of distortions in relating to geometric features. The study found that the spring-in angle increases as the ratio of arc-length to part thickness increases. In particular, this study found that laminates with nearly identical arc-to-thickness ratio produce nearly equal spring-in angles. It also discussed the key role of shear-lag effect in governing spring-in angle of a curved laminates from a numerical perspective. Increasing shear-lag angle decreased the spring-in angle, regardless of factors such as part thickness, radius and lay-up sequence.

The current model provides a framework for addressing the process-induced thermal and chemical residual strains of laminated structures. Based on that, other factors contributing to distortions could be integrated into this modelling framework if

necessary. In the next chapter, this model will be further modified to take TPI effects into consideration when aluminium tool was used.

Chapter 6

Investigation on Spring-in of L-shaped Laminates

6.1 Overview

Following the work conducted in the previous chapter, the next step is to investigate the process-induced distortion in L-shaped laminates. An L-shaped laminates consists of a curved region and two adjacent flanges, the distortion prediction of the former has been thoroughly discussed in the previous chapter, while the combined form will be investigated here. In this chapter, an experimental investigation was carried out, focusing on four factors affecting the spring-in angle, namely, the thickness, the corner radius, the flange length and the lay-up sequence of the part. Following on the warpage observed in flat specimens, tool-part interaction effect was also investigated. A semi-empirical approach was proposed by the author to estimate the equivalent residual stresses induced at the tool-part interface, which was then incorporated into the modelling procedure described in the previous chapter. To evaluate the validity of the developed model, the predicted spring-in angles of L-shaped specimens were compared to the experimental findings.

6.2 Experimental Investigation on Factors Contributing to Spring-in

6.2.1 Tool Preparation

Three aluminium tools were manufactured, with 6.35 mm (0.25 inch), 12.7 mm (0.5 inch) and 25.4 mm (1 inch) radius at the corner, shown in Figure 6.1. All the tools originally came with extruded L-section with 90° sharp corner, which were then CNC machined into round corner with designated radius. The surface were then hand polished to the best achievable smoothness. Prior to use, the tool was cleaned with acetone. A mould release agent Loctite Frekote 700NC was then applied at least 5 times with 5 minutes interval for the applied layer to settle.

It can be observed from Figure 6.1 that the thickness of the tool at the curvature is non-uniform, while a minimum thickness of 10.5mm is maintained at the corner. At an elevated temperature, the enclosed angle of the L-shaped tool is expected to increase due to thermal expansion. However, the thermal expansion and contraction of the tool during autoclave cure process is neglected in this study.



Figure 6.1: Aluminium tools with 0.25/0.5/1.0 inch radius at the curvature

6.2.2 Prepregs Description

Hexcel IM7/8552 unidirectional prepregs were used to conduct an experimental investigation of spring-in phenomenon exhibited in L-shaped laminates. The IM7 carbon fibre is a continuous, high performance, intermediate modulus, PAN-based fibre in 12K filament count tows, while the resin 8552 is a high performance, amine cured, toughened epoxy matrix system. The average cured ply thickness for the supplied batch is 0.19 mm.

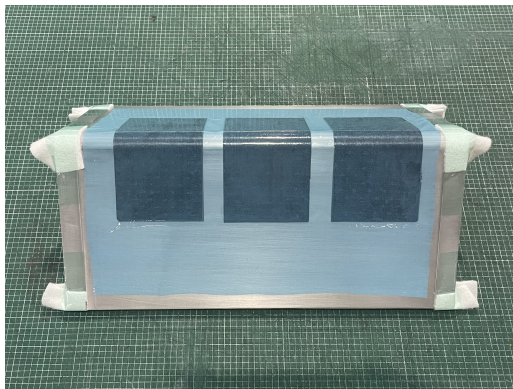
6.2.3 Manufacturing Procedures

Before hand lay-up, prepregs were taken from the freezer and allowed to defrost for at least an hour. An automatic ply cutter was used to cut the prepreg to the desired specification. Each ply was then carefully laid by hand onto aluminium tools. Figure 6.2 illustrates the procedure of preparing an L-shaped specimen. The sharp corners of the aluminium tool were protected by a piece of breather. The lay-up were covered by a peel ply, followed with a breather. The whole part was then placed into the vacuum bag, with two valves secured, sealed with heat resisting tacky tapes. A vacuum test was run for each bag with a pressure gauge and a vacuum generator. For fabricating laminates consisting more than 4 layers, the laminates were debulked at room temperature for every four plies to mitigate interlaminar voids.

6.2.4 Autoclave Cure Process

All the specimens were manufactured in the autoclave following manufacture recommended cure cycle (MRCC). At the beginning of the process, 7 bar gauge autoclave pressure and full vacuum were applied. A temperature ramp of $2^{\circ}\text{C}/\text{min}$ were applied until the ambient temperature reaches 110°C , following which, the specimens dwell at 110°C for 60 minutes. A second temperature ramp and dwell were applied afterwards, where the specimens were heated up at a rate of $2^{\circ}\text{C}/\text{min}$ to 180°C , and

6.2. EXPERIMENTAL INVESTIGATION ON FACTORS CONTRIBUTING TO SPRING-IN



(a)



(b)



(c)



(d)

Figure 6.2: Experimental procedure of preparing L-shaped specimen from step (a) to step (d)

6.2. EXPERIMENTAL INVESTIGATION ON FACTORS CONTRIBUTING TO SPRING-IN

held at 180°C for 120 minutes. The specimens were then cooled down at a rate of $3^{\circ}\text{C}/\text{min}$, until a target temperature of 60°C was reached. The pressure was then vented while the vacuum was still in place. At the end of the cure cycle, specimens were taken out of the autoclave and left to cool down to the room temperature. The designated MRCC and the monitored real-time cure cycle are depicted in Figure 6.3.

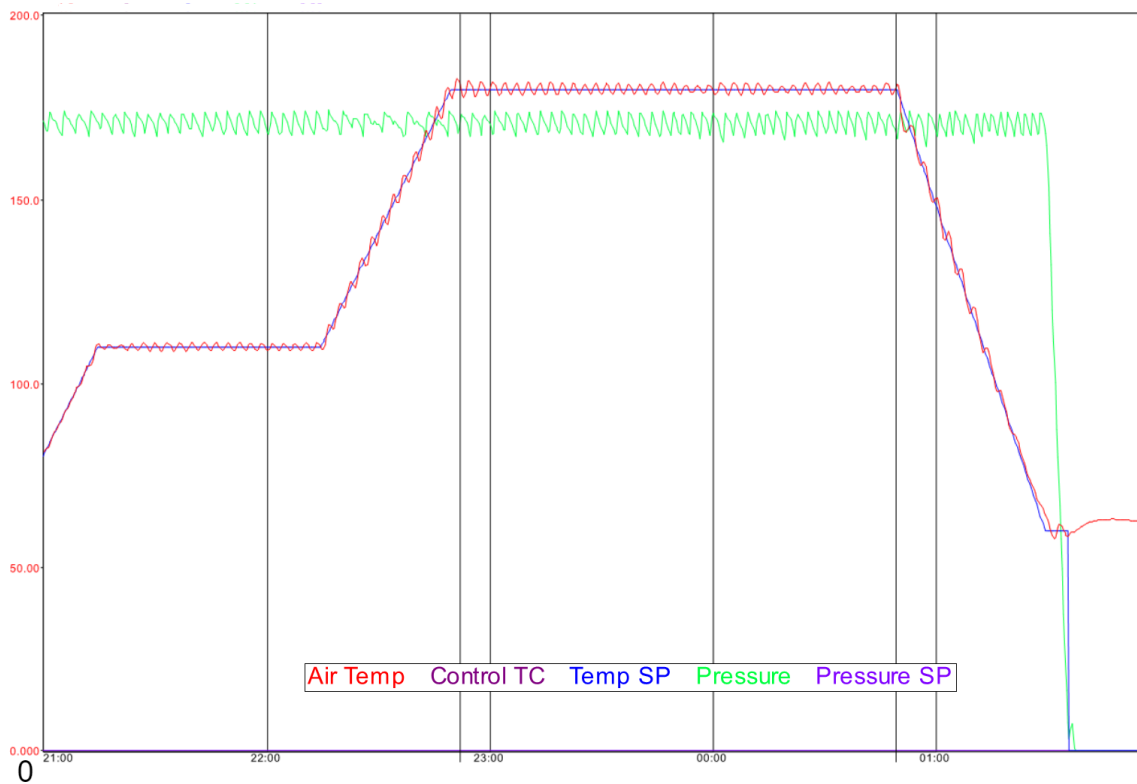


Figure 6.3: Monitored and target autoclave cure cycles

A heat up rate of $2^{\circ}\text{C}/\text{min}$ was chosen to avoid any possible temperature gradient through the thickness of the specimen, as discussed in Chapter 4. In this investigation, the specimen were relatively thin (with maximum thickness of 2.28mm) hence temperature variation in the thickness direction is not seen to be a concern.

After curing in the autoclave, specimens were then trimmed to the designated size. In particular, the excessive resin at the edges of the specimens was removed.

6.2.5 Manufacturing of Specimens

In this work, 30 L-shaped specimens were manufactured. Each L-shaped specimen has a width of 60mm and each configuration was repeated three times to mitigate scattering effects such as dimensional discrepancy from hand lay-up. The L-shaped specimens were categorised into four groups investigating the effect of varying geometrical features, including thickness, radius, flange length, and lay-up sequence, summarised in Table 6.1.

Color Label	Specimen No.	Lay-ups	No. of ply	radius (inch)	flange length (mm)
■	1	$[0/90]_s$	4	0.25	60
■	2	$[0/90]_{2s}$	8	0.25	60
■	3	$[0/90]_{3s}$	12	0.25	60
■	4	$[0/90]_s$	4	0.25	90
■	5	$[0/90]_s$	4	0.25	120
■	6	$[0/90]_s$	4	0.5	60
■	7	$[0/90]_s$	4	1	60
■	8	$[0/45/-45/90]_s$	8	0.25	60
■	9	$[0/90/45/-45]_s$	8	0.25	60
■	10	$[45/-45/90/0]_s$	8	0.25	60

Table 6.1: Configuration of L-shaped specimens

All the L-shaped specimens fabricated in this study are shown in Figure 6.4. All the specimens were colour labelled indicating the groups of interests. The yellow labelled group corresponds to the different number of plies, with a close-up image shown in Figure 6.5a. The red labelled group includes specimens with a corner radius of 0.5 and 1 inches, a side view of which were given in Figure 6.5b. Figure 6.5c shows the specimens with flange length of 60mm, 90mm and 120mm. Lastly, the green labelled specimens were made with different lay-up sequences.

In addition to the L-shaped specimens, 6 flat specimens with $[0/90]_s$ lay-up were fabricated to investigate the effect of tool-part interaction, shown in Figure 6.6. The length of the specimens measures 120 mm, 180 mm and 240 mm, with a consistent width of 40 mm. Two repeated specimens for each configuration were manufactured.

6.2. EXPERIMENTAL INVESTIGATION ON FACTORS CONTRIBUTING TO SPRING-IN

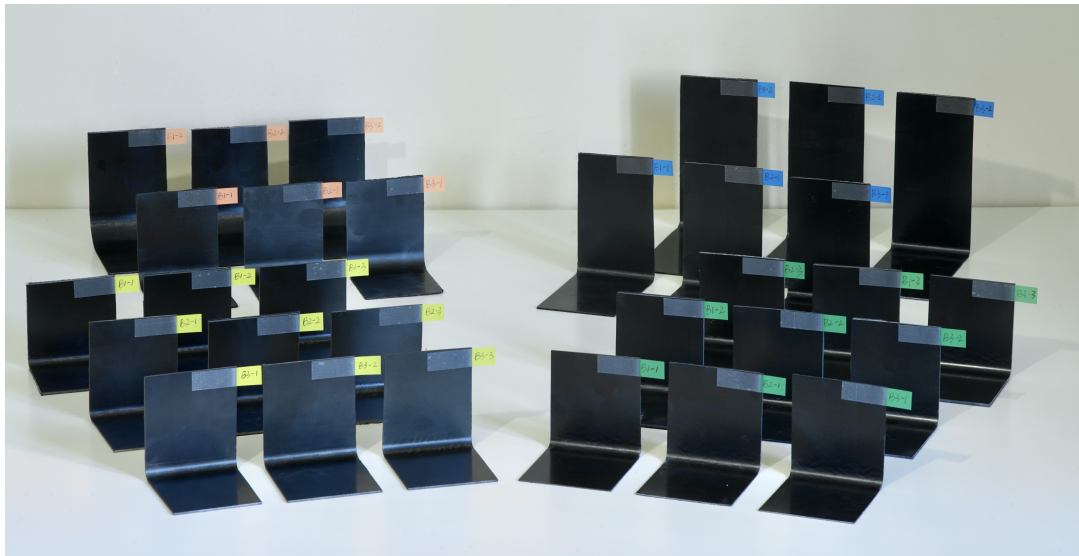


Figure 6.4: All the L-shaped specimens manufactured in this work



(a) ■ thickness



(b) ■ radius



(c) ■ flange length

Figure 6.5: L-shaped specimens with varying (a) thickness (b) radius (c) flange length

6.2. EXPERIMENTAL INVESTIGATION ON FACTORS CONTRIBUTING TO SPRING-IN

All the specimens were laid on the side surface of the aluminium angled tools. This was to ensure the consistent tool surface conditions, e.g. surface smoothness, to that used to manufacture L-shaped specimens.



Figure 6.6: All the flat specimens manufactured in this work

6.2.6 Measurement of Spring-in

The surface geometry of all the specimens and aluminium tools were measured using Creaform HandySCAN, a 3D non-contact laser scanner, with a scanning precision of up to 0.2 mm. An example of scanning an L-shaped specimen is depicted in Figure 6.7. A white powder coating spray was applied to give a matt finish on the surface of the specimens.

Finding the enclosed angle of the L-shaped specimens requires post-processing of the scanned image using GOM Inspect suite. As illustrated in Figure 6.8, two planes were fitted to the flange parts of the scanned specimen using Gaussian best fit algorithm. The fitted planes were transparent red, overlapped with the grey coloured flange parts. The included angle was then determined by taking the angle

6.2. EXPERIMENTAL INVESTIGATION ON FACTORS CONTRIBUTING TO SPRING-IN

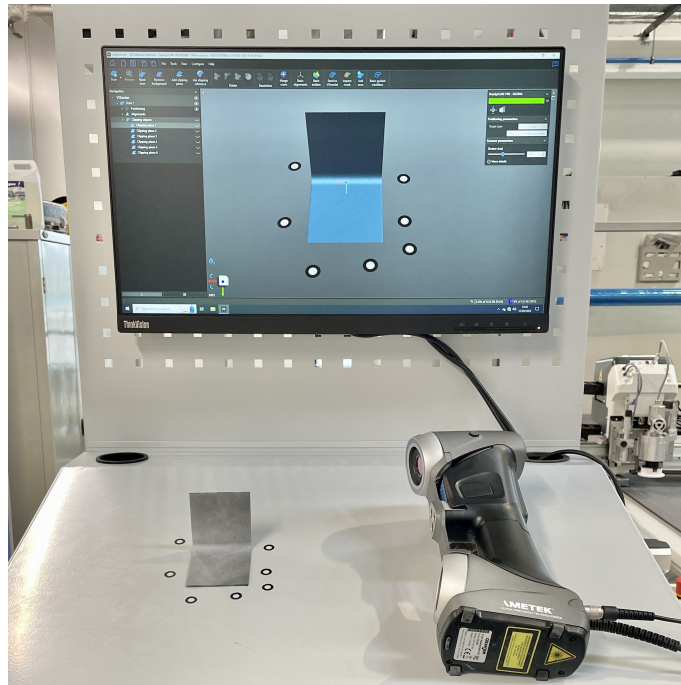


Figure 6.7: Measurements of L-shaped specimen using Creaform 3D HandySCAN of the normal vectors of the two fitted planes. The quality of the two planes fitted to the specimen was also evaluated. A representative example of the plane fitting quality of a L-shaped specimen with a 120 mm flange length was shown in Table 6.2.

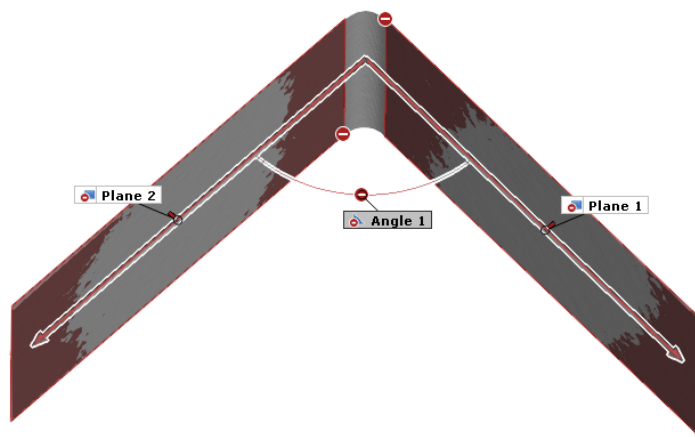


Figure 6.8: Measurements of enclosed angle in GOM Inspect with fitting planes in transparent red and scanned image in grey

The same method was applied to the measurement of aluminium tools. The enclosed angle of each tool was listed in Table 6.3. In the present work, one 1-inch radius,

6.2. EXPERIMENTAL INVESTIGATION ON FACTORS CONTRIBUTING TO SPRING-IN

	Plane 1	Plane 2
Minimum deviation d_{min}	-0.09	-0.12
Maximum deviation d_{max}	0.20	0.20
Standard deviation σ	0.07	0.07
Residual R	0.06	0.06

Table 6.2: The evaluation of the plane fitting quality

one 0.5-inch radius and two 0.25-inch radius tools were used. The surfaces of the tools were hand polished, hence, subjected to small variations in the enclosed angle. Therefore, the scanned geometry of the tool was analysed at different locations to obtain an average measure of the enclosed angle. Measurement indicates that the maximum discrepancy in terms of tool angle is 0.03° .

tool no.	1	2	3	4
radius [inch]	0.25	0.25	0.5	1.0
radius [mm]	6.35	6.35	12.7	25.4
angle [degrees]	90.10 ± 0.01	90.05 ± 0.02	90.03 ± 0.01	90.07 ± 0.03

Table 6.3: Angle profile of tools with different corner radius

Having the angle profile of the L-shaped specimens and that of the aluminium tools, subtracting the angle of the measured specimen from the angle of its corresponding tool gives the spring-in angle of interest. A summary of the calculated spring-in angles of all the manufactured L-shaped specimens was listed in Table 6.4. Overall, the batch-to-batch variation is relatively small. The maximum discrepancy in the measured spring-in angle is 0.44° , the minimum of which is 0.02° . These experimental results will be discussed further when plotted against the numerical predictions in Section 6.4.3.

6.2.7 Measurement of Warpage

6.2.7.1 Warpage in flat specimens

Given the extremely small deflection observed in the specimens, the sample self-weight effect cannot be ignored. Therefore, during the deflection measurement, the

6.2. EXPERIMENTAL INVESTIGATION ON FACTORS CONTRIBUTING TO SPRING-IN

lay-ups	ply	radius [inch]	flange length [mm]	sample 1 [degrees]	sample 2 [degrees]	sample 3 [degrees]
$[0/90]_s$	4	0.25	60	1.91	1.67	1.88
$[0/90]_{2s}$	8	0.25	60	1.70	1.62	1.68
$[0/90]_{3s}$	12	0.25	60	1.44	1.56	1.50
$[0/90]_s$	4	0.25	90	2.08	2.05	1.95
$[0/90]_s$	4	0.25	120	2.41	2.10	2.54
$[0/90]_s$	4	0.5	60	1.88	2.08	2.05
$[0/90]_s$	4	1	60	2.52	2.62	2.27
$[0/45/-45/90]_s$	8	0.25	60	1.57	1.68	1.66
$[0/90/45/-45]_s$	8	0.25	60	1.60	1.55	1.68
$[45/-45/90/0]_s$	8	0.25	60	1.92	1.85	1.99

Table 6.4: Measured spring-in angle of the L-shaped specimens

flat specimens require careful handling. In this study, the specimen was carefully rested on the thickness edge side with minimum support on either surfaces to eliminate self-weight effects, shown in Figure 6.9.

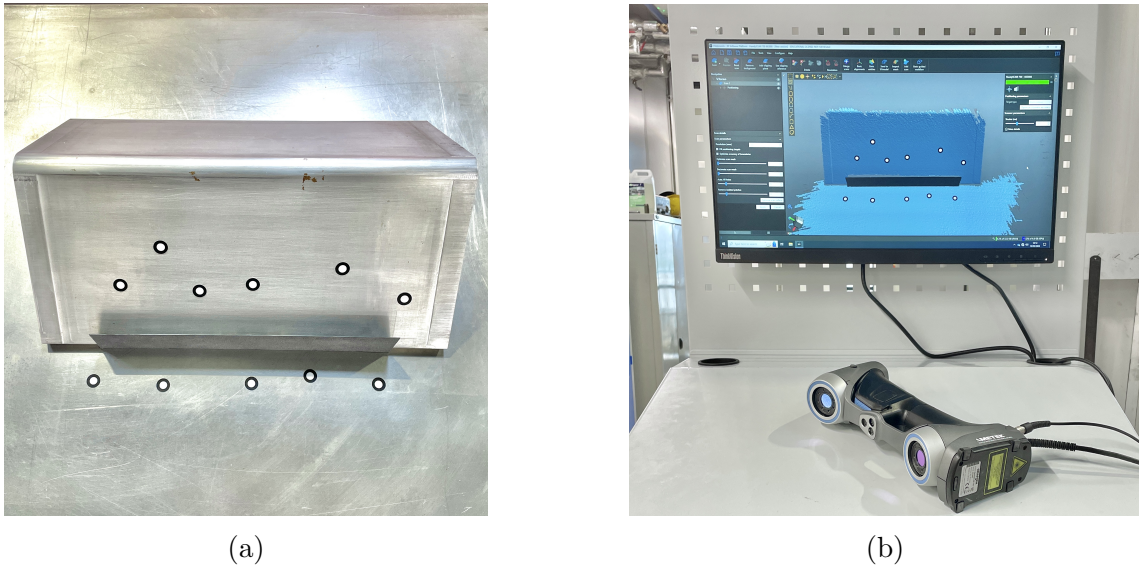


Figure 6.9: Measurements of a flat specimen using Creaform 3D HandySCAN

Processing the scanned image gives the deflection profile along the length of the flat specimens. Taking the specimens with 240 mm length for example, a third order polynomial curve was fitted to the experimental data, as illustrated in Figure 6.10. The maximum warpage is graphically interpreted, which for all the specimens are summarised in Table 6.5.

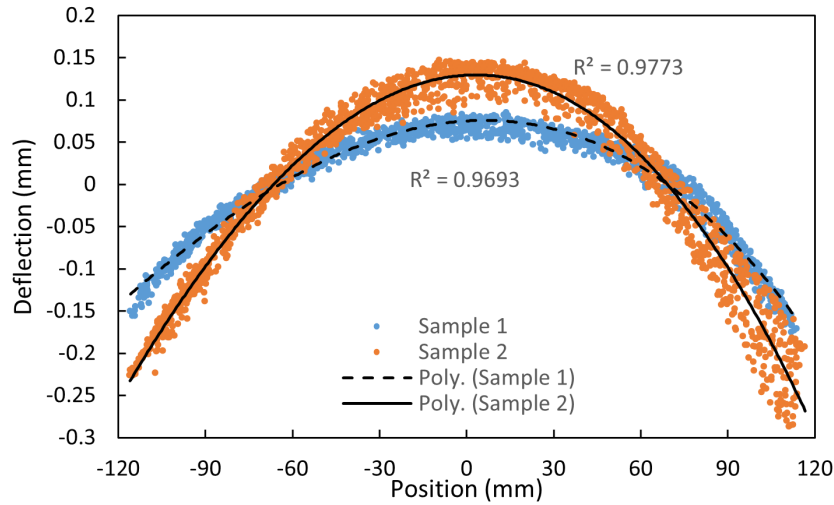


Figure 6.10: Warpage of the specimens with 240 mm flange length

lay-ups	ply	width [mm]	length [mm]	batch 1 [mm]	batch 2 [mm]	average [mm]
$[0/90]_s$	4	40	120	0.18	0.20	0.19
$[0/90]_s$	4	40	180	0.18	0.39	0.29
$[0/90]_s$	4	40	240	0.22	0.38	0.30

Table 6.5: Warpage of the flat specimens

Overall, the warpage from the second batch are more pronounced when compared to the first batch. The two 120 mm specimens give relatively close results in terms of warpage measure. However, for the specimens with a length of 180 mm and 240 mm, the results were scattered. Figure 6.11 indicates that the curvature of specimens from the second batch were more or less close to each other, while the specimens from the first batch give large variation in the measured curvature.

6.2.7.2 Warpage in the flange part of L-shaped specimens

Recall the plane fitting to the flange part as already shown in Figure 6.8, a slight warpage was also observed. To investigate the magnitude of warpage in the flange part, the scanned data points were processed as described earlier. Figure 6.12 illustrated the warpage in the flange part of measured specimens. For the L-shaped specimens with varies flange length, the plotted curvature remained relatively con-

6.2. EXPERIMENTAL INVESTIGATION ON FACTORS CONTRIBUTING TO SPRING-IN

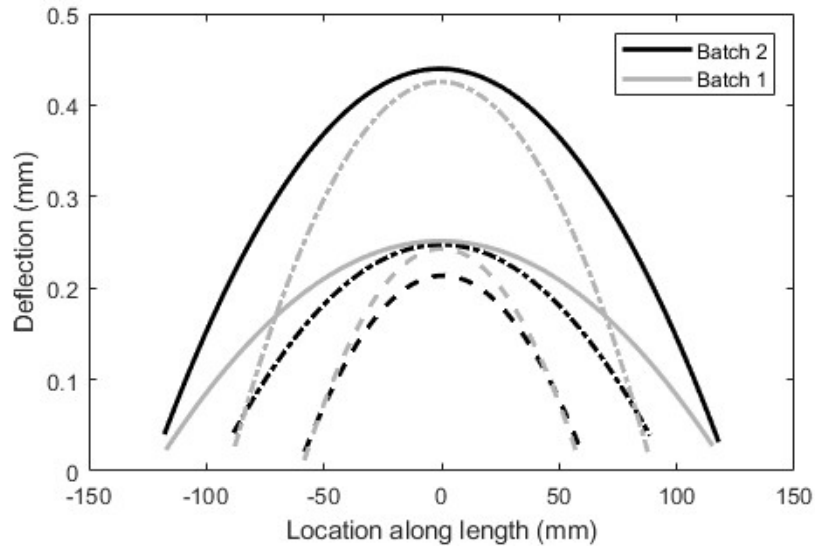


Figure 6.11: Warpage of the flat specimens from batch 1 and batch 2

sistent. This indicates that the tool-part shear effect on the flange has a consistent magnitude regardless the length of the flange. This can be attributed to the fact that the flange's deflection is constrained at one end, adjacent to the curved part.

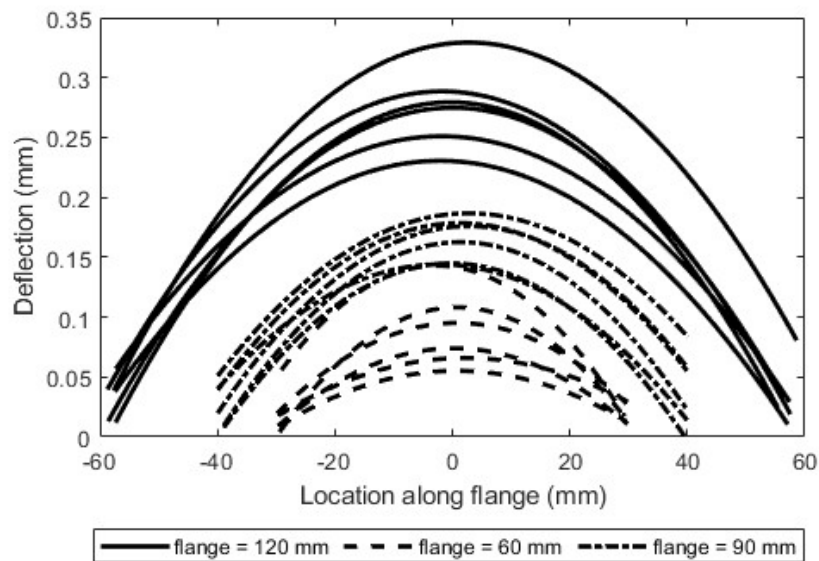


Figure 6.12: Warpage in the flange part of the L-shaped specimens

6.2.8 Experimental Uncertainties

During the manufacturing of the specimens, one potential source of error could be the fibre misalignment during hand lay-up. Without a laser projection, the fabricated prepregs could be unbalanced if one of the plies was significantly misaligned. In this work, those specimens with unsymmetrical distortions were eliminated from the analysis since their induced spring-in angles were not reliable.

A corner thinning effect was also observed from the specimens. The thickness of the corner region and that at the flange region was found to be different. Table 6.6 summarises the average thickness of each categorised specimens from all three repeated batches. The study found that the average cured single ply thickness at the flange part is 0.19mm, while the average cured single ply thickness at the corner region is between 0.17 to 0.18mm.

lay-ups	ply	radius [inch]	L_{flange} [mm]	t_{corner} [mm]	t_{flange} [mm]
$[0/90]_s$	4	0.25	60	0.66 ± 0.03	0.75 ± 0.04
$[0/90]_{2s}$	8	0.25	60	1.39 ± 0.06	1.53 ± 0.04
$[0/90]_{3s}$	12	0.25	60	2.11 ± 0.05	2.29 ± 0.05
$[0/90]_s$	4	0.5	60	0.72 ± 0.02	0.75 ± 0.04
$[0/90]_s$	4	1	60	-	-
$[0/90]_s$	4	0.25	90	0.68 ± 0.02	0.75 ± 0.04
$[0/90]_s$	4	0.25	120	0.68 ± 0.04	0.75 ± 0.03
$[0/45/ - 45/90]_s$	8	0.25	60	1.35 ± 0.01	1.53 ± 0.03
$[0/90/45/ - 45]_s$	8	0.25	60	1.37 ± 0.03	1.52 ± 0.03
$[45/ - 45/90/0]_s$	8	0.25	60	1.41 ± 0.05	1.54 ± 0.04

Table 6.6: Measured thickness at flange and corner of the specimens

Expanding upon the corner thinning effect, it is likely that there are also variations in the fibre volume fraction V_f . Higher V_f would be expected at the corner compared that at the flange. In the through-thickness direction, V_f gradient could also be a potential source of uncertainties.

6.3 Semi-empirical Investigation on Tool-Part Shear Interaction

Different methods of quantifying tool-part interactions has been discussed in Section 2.4.1. In this study, a semi-empirical approach was proposed to quantify such phenomenon using an equivalent shear stress at tool-part interface.

For a symmetric and balanced laminates, the chemical and thermal shrinkage does not contribute to the warpage deflection, therefore, the warpage observed in a flat specimen was only the result of the tool-part interaction. In this study, certain assumptions were applied based on the findings from the literature (Twigg et al., 2003, 2004a; Yuan et al., 2016). It is assumed that 1) the majority of the load was carried at the closest [0] contact layer during autoclave process, i.e. the bending moment causing warpage is solely the result of residual stresses induced in the 1st ply. 2) A uniform shear stress distribution at the tool-part interface was assumed, although this assumption does not always apply in the case of more complex geometries.

6.3.1 Analytical Prediction of Tool-Part Interaction Effect

Based on the assumptions mentioned earlier, the force equilibrium at the load-bearing layer is illustrated in Figure 6.13, written in the form of

$$d\sigma \cdot h_s + \tau_s \cdot dx = 0 \quad (6.1)$$

where h_s is the thickness of a single layer, σ is the tensile/compressive stress component, and τ_s is the shear stress. The total thickness of the laminates is h , taking symmetric geometry of the 1st [0] layer, the half length is l and the depth is b . The distance from the 1st [0] layer (load bearing layer) to the mid-plane is denoted as z_s and the distance from the k^{th} layer to the mid-plane is denoted as z_k .

6.3. SEMI-EMPIRICAL INVESTIGATION ON TOOL-PART SHEAR INTERACTION

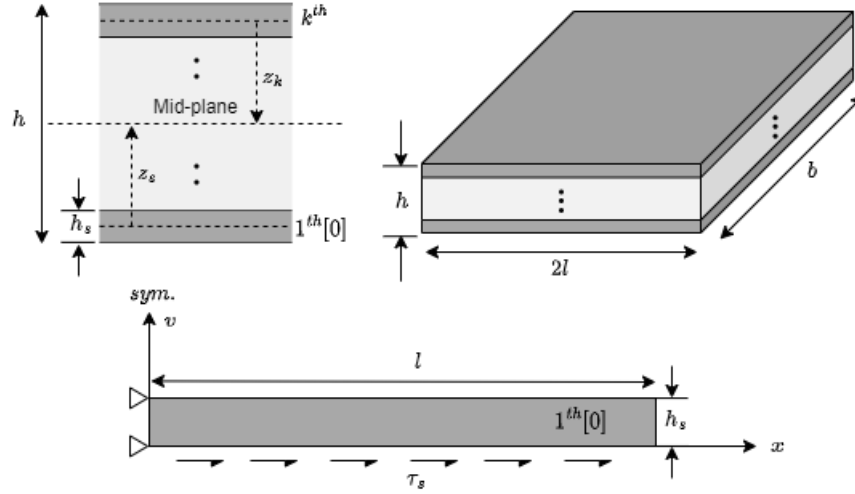


Figure 6.13: Force diagram of tool-part interaction

Integrating Eq.(6.1) gives

$$\int_0^x d\sigma = \int_0^x -\frac{\tau_s}{h_s} dx \quad (6.2)$$

$$\sigma(x) - \sigma(0) = -\frac{\tau_s}{h_s} x \quad (6.3)$$

Applying boundary conditions

$$\sigma(l) = 0 \quad (6.4)$$

gives

$$\sigma(0) = \frac{\tau_s}{h_s} l \quad (6.5)$$

Taking Eq.(6.5) into Eq.(6.3), the residual stress is expressed as

$$\sigma(x) = \frac{\tau_s}{h_s} (l - x) \quad (6.6)$$

Based on small strain theory, the curvature of a laminate is expressed as

$$\kappa = \frac{d^2 v}{dx^2} = \frac{M}{(EI)_{eff}} \quad (6.7)$$

6.3. SEMI-EMPIRICAL INVESTIGATION ON TOOL-PART SHEAR INTERACTION

in which the moment M is defined as

$$M = \sigma \cdot h_s \cdot z_s \cdot b \quad (6.8)$$

Combining Eq.(6.6), Eq.(6.7) and Eq.(6.8) gives

$$\frac{d^2v}{dx^2} = \frac{z_s \tau_s b}{EI_{eff}} (l - x) \quad (6.9)$$

The boundary conditions for this case are given as

$$\begin{cases} \frac{dv}{dx} = 0 & \text{at } x = 0 \\ v = 0 & \text{at } x = 0 \end{cases} \quad (6.10)$$

Integrating Eq.(6.9) gives

$$v = \frac{z_s \tau_s b}{2EI_{eff}} (lx^2 - \frac{1}{3}x^3) \quad (6.11)$$

Therefore, the maximum deflection can be found at $x = l$

$$v_{max} = \frac{z_s \tau_s l^3 b}{3EI_{eff}} \quad (6.12)$$

Based on CLT detailed in section 3.2, the effective flexural stiffness is expressed as

$$EI_{eff} = \sum_{k=1}^m [\bar{Q}_{11}]_k \left(\frac{1}{12} h_s^3 + z_k^2 h_s \right) b \quad (6.13)$$

where m is the number of layers. Taking Eq.(6.13) into Eq.(6.12) gives

$$v_{max} = \frac{\tau_s z_s l^3}{3 \sum_{k=1}^m [\bar{Q}_{11}]_k \left(\frac{1}{12} h_s^3 + z_k^2 h_s \right)} \quad (6.14)$$

Recall from the Figure 6.13

$$z_k = h\left(\frac{1}{2} - \frac{k}{m} + \frac{1}{2m}\right); \quad h_s = \frac{h}{m} \quad (6.15)$$

Hence, Eq.(6.14) yields

$$v_{max} = \frac{\tau_s z_s l^3}{3h^3 \sum_{k=1}^m [\bar{Q}_{11}]_k \left[\frac{1}{12m^3} + \frac{1}{m}\left(\frac{1}{2} - \frac{k}{m} + \frac{1}{2m}\right)^2\right]} \quad (6.16)$$

Rearranging Eq.(6.16) gives

$$v_{max} = \tau_s \cdot \frac{z_s}{h^3} \cdot l^3 \cdot \frac{1}{3 \sum_{k=1}^m [\bar{Q}_{11}]_k \left[\frac{1}{12m^3} + \frac{1}{m}\left(\frac{1}{2} - \frac{k}{m} + \frac{1}{2m}\right)^2\right]} \quad (6.17)$$

Eq.(6.17) indicates the maximum deflection is proportional to the length of the laminates to its third power l^3 , and is inversely proportional to z_s with respect to the laminate thickness to its third power h^3 . The analytical form agrees well with the experimental findings presented by Twigg et al. (2004a).

Rearranging Eq.(6.16), the tool-part interactive shear stress τ_s can then be derived from the warpage measurement for the given length of a laminate, shown below.

$$\tau_s = \frac{3h^3 v_{max}}{z_s l^3} \sum_{k=1}^m [\bar{Q}_{11}]_k \left[\frac{1}{12m^3} + \frac{1}{m}\left(\frac{1}{2} - \frac{k}{m} + \frac{1}{2m}\right)^2\right] \quad (6.18)$$

6.3.2 Numerical Prediction of Tool-Part Interaction Effect

The analytically prediction of shear stress τ_s from the previous section was further validated in the numerical model here. As depicted in Figure 6.14, a $[0/90]_s$ cross-ply laminate was modelled subjected to a shear load only at the bottom of the laminate. A static analysis was performed and symmetrical boundary conditions were applied. This shear load was calibrated so that the maximum deflection fits

6.3. SEMI-EMPIRICAL INVESTIGATION ON TOOL-PART SHEAR INTERACTION

the experimentally measured deflection.

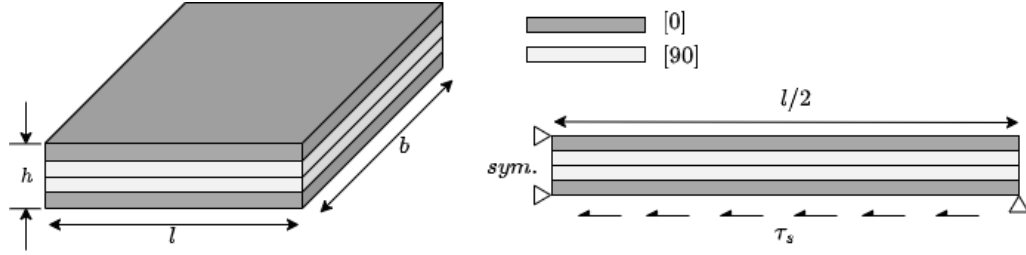


Figure 6.14: Model geometry and boundary conditions of the flat laminates

Table 6.7 compared the analytically derived shear value with numerically calibrated shear value. The analytical shear values were calculated using Eq.(6.18). The results revealed that the analytical method overestimates the shear at the tool-part interface when compared with the numerically calibrated values. Recall the experimental results show that longer specimens produce higher variability in warpage. In the case of 240 mm flat specimen, warpage measurement varying from 0.2 mm to 0.4 mm could result in the shear value varying from 5.2 kPa to 10.5 kPa.

Length [mm]	Batch 1 [mm]	Batch 2 [mm]	Avg. Warpage [mm]	Analytical τ_s [kPa]	Numerical τ_s [kPa]
120	0.18	0.20	0.19	51.2	35.0
180	0.18	0.39	0.29	23.5	15.5
240	0.22	0.38	0.30	10.9	7.9

Table 6.7: Equivalent tool-part interface shear of the flat specimens

Figure 6.15 illustrates the relationship between specimen length and its corresponding shear stress. For both numerical and analytical predictions, as the length of the specimen increased, the τ value decreases non-linearly.

Such phenomenon could be contributed by edge-effects, illustrated in Figure 6.16. The true shear stress diminishes at the edge of the specimen, however, in this work, a uniform distribution of shear stress was assumed. As the length of the specimen increased, the calculated shear stress τ_{cal} is closing up to the true shear stress τ_{true} .

6.3. SEMI-EMPIRICAL INVESTIGATION ON TOOL-PART SHEAR INTERACTION

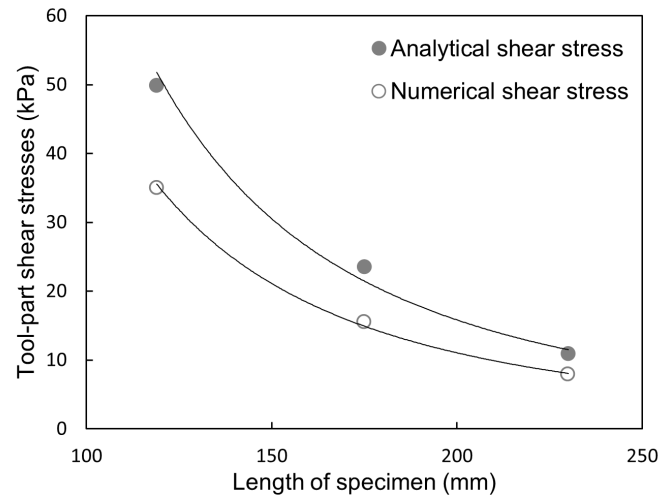


Figure 6.15: Relationship between the specimen length and its corresponding tool-part shear stress τ_s

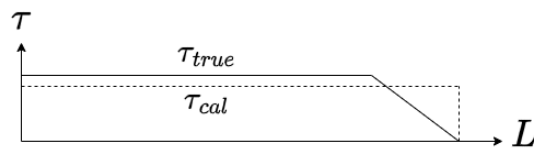


Figure 6.16: Edge effect of tool-part shear stress τ

6.3. SEMI-EMPIRICAL INVESTIGATION ON TOOL-PART SHEAR INTERACTION

In this work, For a given surface condition, the friction between the tool and the specimen should be constant regardless the length of the specimen. Therefore, a constant shear stress can be determined from fitting a curve to the available data points. Rearranging Eq.(6.16) gives

$$v_{max} = \frac{\tau_s z_s}{3h^3 \sum_{k=1}^m [\bar{Q}_{11}]_k \left[\frac{1}{12m^3} + \frac{1}{m} \left(\frac{1}{2} - \frac{k}{m} + \frac{1}{2m} \right)^2 \right]} \cdot l^3 \quad (6.19)$$

where τ_s , z_s , h , $[\bar{Q}_{11}]_k$, m and k are all constants. The maximum deflections were plotted against the length of the specimens, as shown in Figure 6.17. By fitting a curve to the experimental data, the relationship satisfying Eq.(6.16) was enforced, where the maximum deflection is proportional to the l^3 . A shear stress of 13.5 kPa can then be obtained.

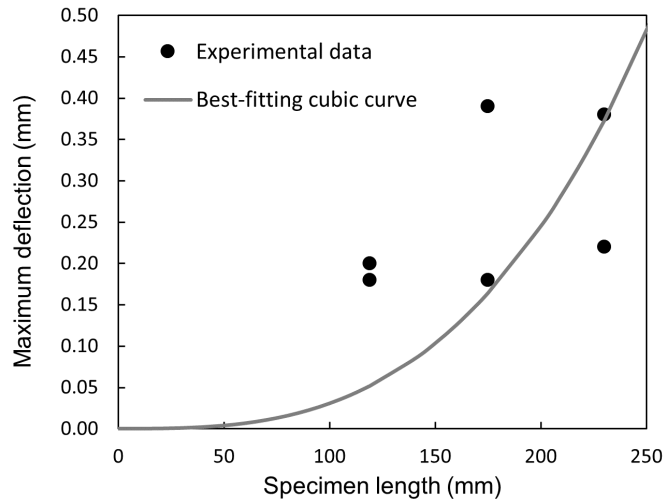


Figure 6.17: Determining shear term τ_s

It is noticeable that the experimental data was rather scattered. The 95% confidence interval for the shear stress lies within [5.7, 21.4] kPa. In the following sections, the effectiveness of the chosen TPI shear stress was examined. A sensitivity study was also conducted to reveal the variability in the corresponding spring-in angle given a wide-ranging value of shear stress.

Limited by the length of the tool in this work, data with longer specimens were

not available here. However, the author has also conducted experiments on other aluminium flat tool to examine the relationship between the length of the specimens and its corresponding maximum warpage. These experimental findings will be discussed in the next chapter.

6.4 Numerical Investigation on Factors Contributing to Spring-in

Using the modelling strategies mentioned in Section 5.2, an additional static analysis step was added to the original model taking consideration of the tool-part shear interaction.

6.4.1 Model Description

Taking advantage of symmetry, a quarter section of an L-shaped laminates was modelled, as illustrated in Figure 6.18. The model consists of a flange part and a 45° curved part. The inner radius of the curved part corresponds to the radius of the aluminium tool. The length of the flange was consistent to the specimen configurations. The simulation was performed in two analysis steps, namely a coupled temperature-displacement analysis, corresponding to the autoclave cure process, and a static analysis, representing the demoulding. In the autoclave cure process, the part was constrained in the normal direction at the tool-part contact surface, subjected to autoclave pressure load. The pressure and the surface support were then removed to simulate the demoulding process. One element per ply in the thickness direction was assigned in the through-thickness direction, while a sufficiently small meshing size was assigned to the arc direction. An 8-node coupled-temperature-displacement solid element C3D8T was selected. The ambient temperature was assumed to be 20°C. Surface film conditions were applied at the tool side and vacuum bag side of the laminates, to account for the heat transfer from autoclave temperature to part

6.4. NUMERICAL INVESTIGATION ON FACTORS CONTRIBUTING TO SPRING-IN

surface through convection. The effective film coefficients for both sides can be found in Johnston (1997). This coupled temperature-displacement model took account of the residual stresses due to chemical and thermal shrinkage only.

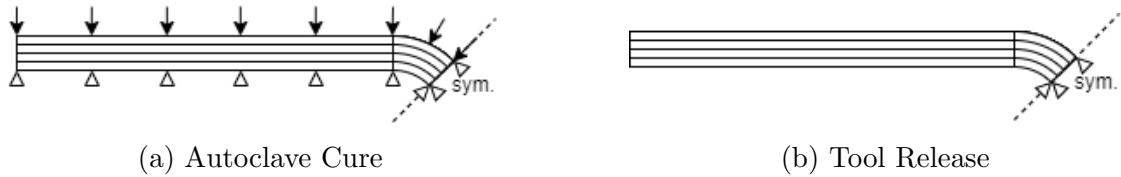


Figure 6.18: Geometry and boundary conditions for the two-step analysis of the L-shaped laminates

A follow-up static analysis was performed taking consideration of tool-part interaction only. The boundary conditions for this case are depicted in Figure 6.19. Surface shear of 13.5 kPa was applied as the equivalent residual stresses causing warpage in the flange part. The induced spring-in angle was then super-positioned onto that obtained from the previous analysis.



Figure 6.19: Boundary conditions for tool-part interaction analysis of the L-shaped laminates

Although the manufacture provided nominal cured thickness of a single ply is 0.13 mm, the average cured single ply thickness measured in the lab was 0.19 mm, which agrees well with the complementary report came with the batch. Hence, a cured ply thickness of 0.19 mm was adopted in the numerical simulation. The nominal fibre volume fraction was 57.7% and the nominal laminate density was 1570 kg/m³. The thermal, chemical and mechanical properties of IM7/8552 laminates have all been presented in section 4.4.1, thus not repeated here.

6.4.2 Definition of 'Spring-in' angle

It is important to state clearly how the 'spring-in' angle was defined as different author may adopt different method, which could result in slight different measurement even for the identical deformed shape. As aforementioned in Section 6.2.6, for experimental findings, the spring-in angle was taking as the enclosed angle between two fitted planes to the flanges. In the numerical prediction, an alternative method was chosen for the ease of post-processing. Figure 6.20 illustrates the definition of 'spring-in' angle for the numerical study.

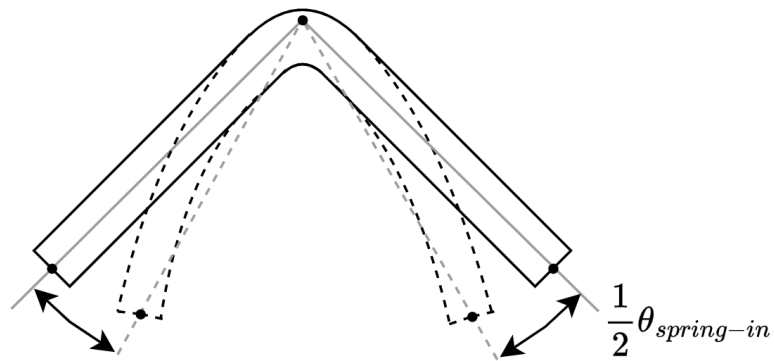


Figure 6.20: Definition of 'Spring-in' angle in numerical prediction

6.4.3 Comparison of Numerical and Experimental Results

The spring-in angle between the numerical prediction and the experimental results were compared in this section. The numerical prediction distinguishes chemical, thermal, and tool-part interaction contributions to the total spring-in angle. This investigation looked at geometric features of an L-shaped laminates, namely thickness, corner radius, and flange length effects.

It was found that doubling flange length (from 60 mm to 120 mm) has a larger impact on the spring-in angle of the specimen, when comparing thickness and radius effects. Furthermore, doubling radius from 12.7 mm to 25.4 mm seems has a larger impact on spring-in angle when compared to doubling radius from 6.35 mm to 12.7 mm. This could be the fact that larger radius specimen has a longer contact length at

6.4. NUMERICAL INVESTIGATION ON FACTORS CONTRIBUTING TO SPRING-IN

the corner part, hence induced larger TPI effect on the spring-in phenomenon.

Overall, the numerical prediction underestimates the spring-in angle by approximately half degree in average, while the trends agree well with the experimental findings. Such phenomenon could be the results of many factors. Firstly, since the chemical and thermal shrinkage strains were taken from the literature, any underestimation of the effective CTE and CCS could cause reduced spring-in distortion from the modelling results. Secondly, as previously mentioned in section 6.2.8, corner thinning effect was observed from the specimens, accompanied by variation in fibre volume fractions. The reduced thickness at the corner could also result in increased spring-in angle from the experimental measurements.

Figure 6.21 reveals a clear trend in decreased spring-in angle with increasing laminate thickness. It was found that the thermal component does not vary much with changing thickness, while the contributions from chemical shrinkage and tool-part interaction decreased with increasing thickness. As bending stiffness increases, the warpage in the flange part decreases significantly.

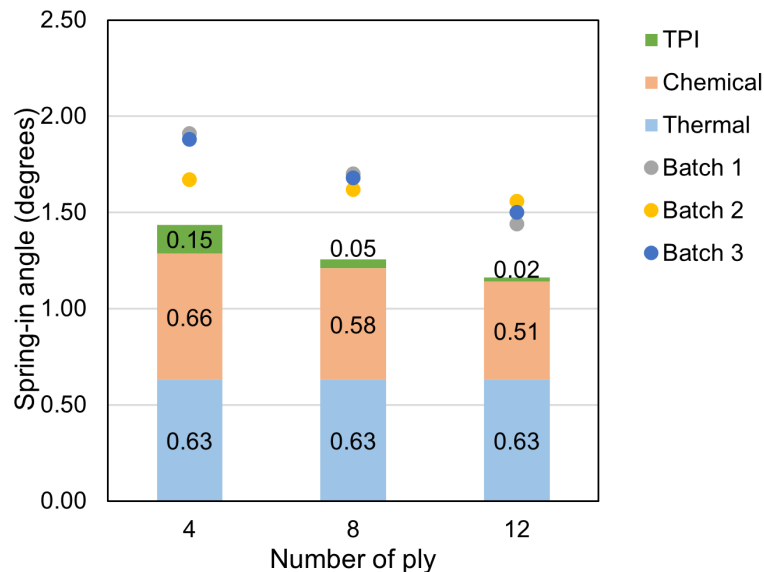


Figure 6.21: Experimental and numerical results for spring-in angle of L-shaped specimen with varying number of ply

Figure 6.23 indicates that increasing corner radius increases the spring-in angle contributions from chemical and thermal shrinkage. It also indicates that increasing corner radius gives increased discrepancy between the experimental and numerical spring-in angle. This was the result of omitting TPI modelling at the curved part. In the analysis of TPI effect, the flange length was kept constant, therefore, the tool-part interaction was found to have equal effect on the final spring-in. However, the specimens with larger radius also have longer arc length, the TPI-induced spring-in angle should increase as the corner radius increase, which narrows the gap between the experimental and numerical findings for specimens with larger corner radius.

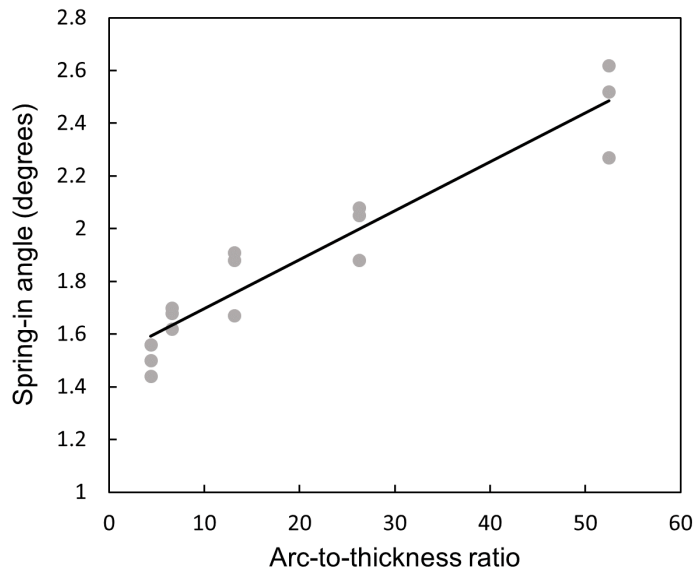


Figure 6.22: Arc-to-thickness ratio versus spring-in angle

In terms of curved part, plotting the arc-to-thickness ratio against the experimental spring-in angle gives a relatively linear relationship, as shown in Figure 6.22.

It could be observed from the experimental results that the warpage in the flange part was more prominent in the specimen with longer flange length, which resulted in larger spring-in angle, shown in Figure 6.24. This phenomenon was also captured in the numerical prediction. The chemical and thermal contribution to spring-in angle does not vary with changing flange length, while the effect from tool-part interaction was more significant as flange length increased.

6.4. NUMERICAL INVESTIGATION ON FACTORS CONTRIBUTING TO SPRING-IN

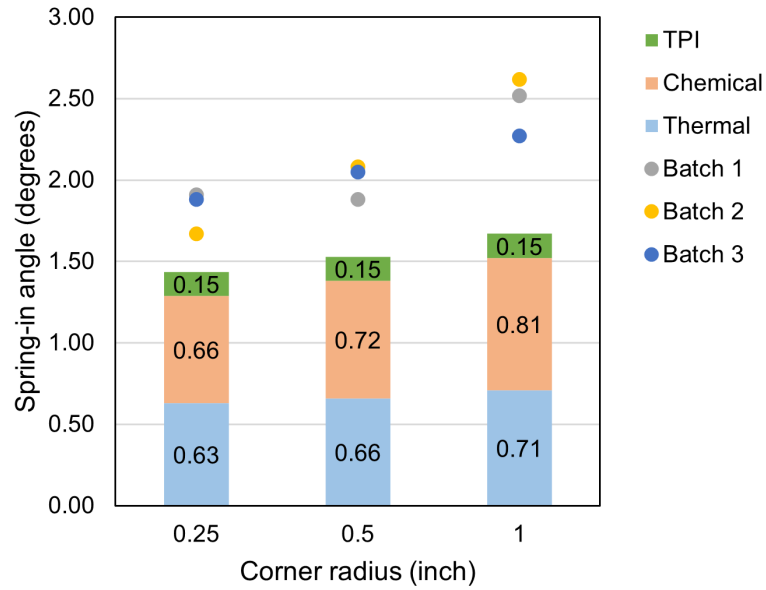


Figure 6.23: Experimental and numerical results for spring-in angle of L-shaped specimen with varying corner radius

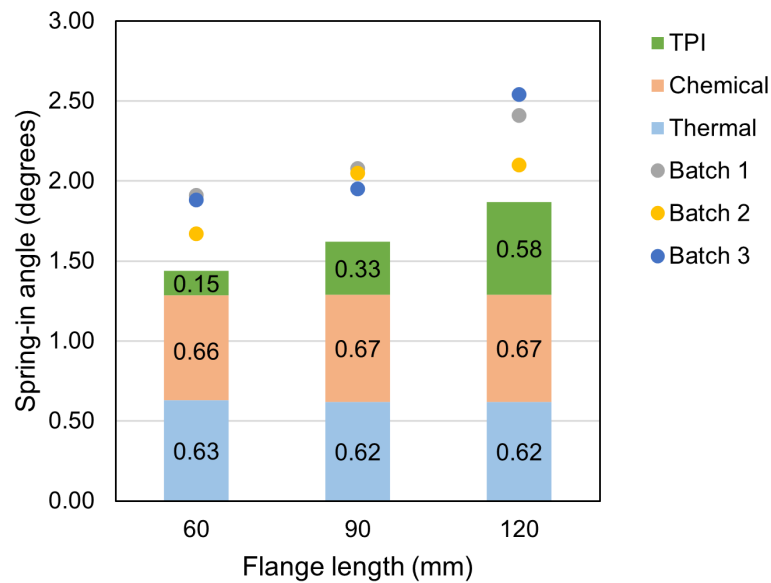


Figure 6.24: Experimental and numerical results for spring-in angle of L-shaped specimen with varying flange length

6.4.4 Sensitivity Analysis on Tool-part Shear

In the numerical simulation, the shear term 13.5 kPa was calibrated from flat specimens, bearing in mind this value could vary from 5.7kPa to 21.4kPa, as previously discussed in Section 6.3.2. For the given range of shear stress, the corresponding spring-in angle contributed by TPI only was also numerically investigated.

Figure 6.25 shows the TPI-induced spring-in angle variation subjected to TPI shear stress with 95% confidence interval. Labels 1-7 refer to specimens in Table 6.1. Overall, for specimens consisting 4 plies, the spring-in angle could vary from 0.2° to 0.6° given a shear stress also varying around 50%.

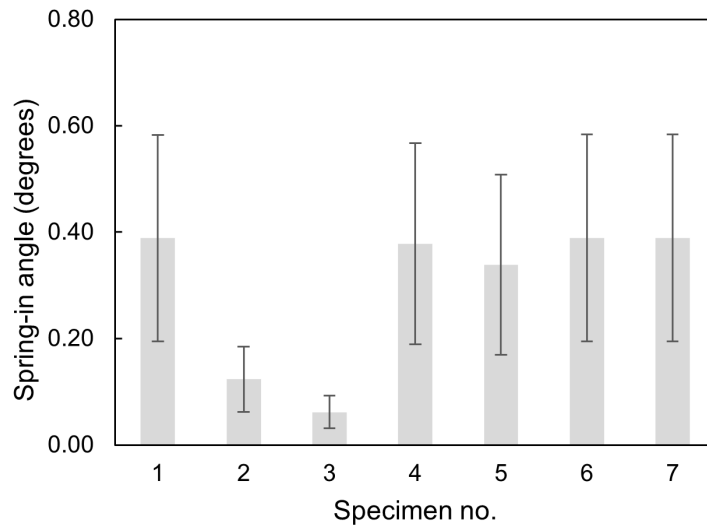


Figure 6.25: TPI-induced spring-in angle for the labelled specimen configurations with varied geometric parameters

When comparing to the overall spring-in angle of the L-shaped specimen, such variation in the spring-in angle contributed by TPI effect cannot be neglected, particular for the L-shaped part containing long flanges. In the following chapter, the effect of TPI will be further discussed in the case of more practical engineering design scenarios.

6.5 Summary

This chapter investigated the spring-in and warpage phenomenon in L-shaped laminates through experimental and numerical approaches. A total of 30 L-shaped specimens were manufactured, whose design featuring different thickness, corner radius, flange length and lay-up sequence. In addition, 6 pieces of flat cross-ply laminated specimens were manufactured to explore the effects of tool-part interactions in greater detail.

In this chapter, a novel semi-empirical method was proposed to offer a simple yet reliable estimation of warpage induced by tool-part shear interaction. This method presents a universal means of determining an approximate shear stress value for a given tool surface condition. By manufacturing a series of flat specimens on the same tool, a shear stress term can be extrapolated through the curve fitting to the experimental data.

Nonetheless, the proposed method has its own limitations. The distribution of the shear stress was estimated based on the exhibited warpage of the specimen. For scenarios that the part exhibits non-warpage like distortion, the applicability of the proposed TPI method needs to be revisited.

Overall, the developed modelling framework presented in this chapter has proven to be a valid approach when predicting the spring-in distortions of angled parts. It was concluded that this model tends to underestimate spring-in angles by approximately half degree, however, the trends in the numerical results align closely with the experimental findings. The effectiveness of the proposed modelling framework could be further examined if on-site material characterisation data is available.

Chapter 7

Investigation on Distortions of Tapered Laminates

7.1 Overview

This chapter is devoted to investigate the process-induced distortions in tapered laminates using the developed simulation framework. The previously proposed semi-empirical TPI model is also validated here.

Laminates with ply-drops are widely used in engineering applications to accommodate changing thickness requirement. This is typically achieved by terminating some plies at designated positions. The primary objective of this chapter is to uncover the influence of the ply-drops and their relationships to the process-induced distortions, and assess the extent to which these distortions can be predicted.

This chapter commences with the modelling of tapered laminates, the model geometry was complemented by a microscopy study of resin pocket geometries. The boundary condition for each analysis step was illustrated. The study then evaluated the tool surface condition by manufacturing reference specimens without ply-drops,

employing the semi-empirical method developed from the previous chapter. Subsequently, a series of experimental and numerical studies were performed to investigate the effect of various parameters. These parameters include the dropped ply orientations, the number of dropped plies, and the ply-drop ratio. The validity and limitations of the developed model in predicting process-induced distortions were thoroughly examined.

7.2 Design Guidelines

While ply-drop designs are typically tailored to specific applications, there are still some universal design principles to reduce potential risks. One obvious example is that a gradually tapered laminate with multiple drop-off locations is preferable than a single drop-off location. Here, a set of general guidelines for stacking sequence design is provided, followed by ply drop-off design recommendations.

Stacking sequence design guidelines (Irisarri et al., 2014)

- The stacking sequence should be symmetric and balanced to avoid any in-plane distortions
- The orientation difference between two consecutive plies should not exceed 45° to minimise interlaminar shear stresses
- Stack of plies should be shuffled to ensure minimum 10% and maximum 70% in each fibre directions

Ply drop-off design guidelines (Irisarri et al., 2014; Paul et al., 1990)

- Maintain $d/t > 20$ in primary load direction and $d/t > 10$ in secondary load direction
- Plies should be dropped in decreasing order of stiffness to ensure smooth trans-

fer of load and reduce stress concentrations

- Surface plies should not be dropped
- Angle ply pairs, such as $45^\circ/-45^\circ$ should be dropped off together whenever possible
- 90° plies should be adjacent to $45^\circ/-45^\circ$ whenever possible
- The inner plies should be dropped first

Although the engineering practice typically discourage the orientation difference between two consecutive plies to exceed 45° , all specimens were manufactured as $[0/90]$ cross-ply laminates to simplify the manufacturing and reduce the number of variables.

7.3 Modelling of Laminates with Ply-drops

7.3.1 Microscopy of Ply-drop Regions

The modelling geometry of the resin-rich area was initially configured based on microscopy samples. Figure 7.1 captured the resin-rich area and entrapped voids at ply drop-offs regions. The black area represents the entrapped voids and the grey triangle area represents the resin-rich region. Delamination was also observed at the right-hand side of the laminates, which is a result of the trimming process. Although the plies were intended to be dropped at the same location, the misalignment at the dropped edge is still notable at microns scale, where the distance between two dropped plies can be seen to close to 1 mm. Therefore, it is not feasible to drop two plies together in the hand lay-up process. Given the microscopic geometry, a simplified geometry is necessary for the modelling purpose, which will be discussed in the following section.

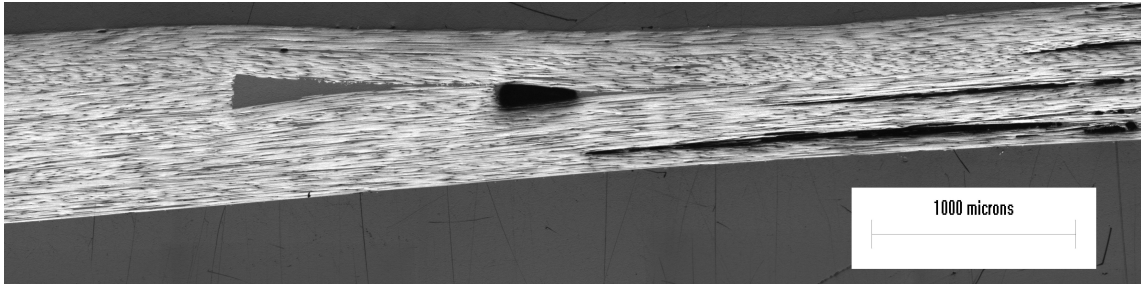


Figure 7.1: The resin-rich area and entrapped voids at ply drop-offs regions of UD laminates

7.3.2 Model Description

The modelling framework has been thoroughly discussed in the previous chapters and thus not repeated here. The resin-rich area was modelled as a triangle shape. Unless stated otherwise, the length-to-thickness ratio of the resin pocket equals to 3 for all numerical predictions. No voids were considered in the modelling procedure, all resin pockets were assumed to be fully saturated. For multiple plies dropped at the same location, no misalignment was considered. The fibre orientation at the drop-off regions were assigned to follow the exact path as illustrated in the ply-drop design configuration.

A three-step analysis was performed, namely the autoclave cure process, tool release step, and a tool-part interaction (TPI) step. This is to distinguish the process-induced distortions raised from non-TPI and TPI effect only. The shear load and boundary conditions at the TPI analysis step were depicted in Figure 7.2. The calculation of the applied shear stresses will be discussed in the following section. No load was applied at the tool-side of the ply-drop region, primarily due to the complicity of the residual stress distribution at the tapered regions. One should be reminded the symmetric distribution of the shear stress that acts equivalent to the tool-part interaction is still a simplified estimation, leaving quite a room for improvement.

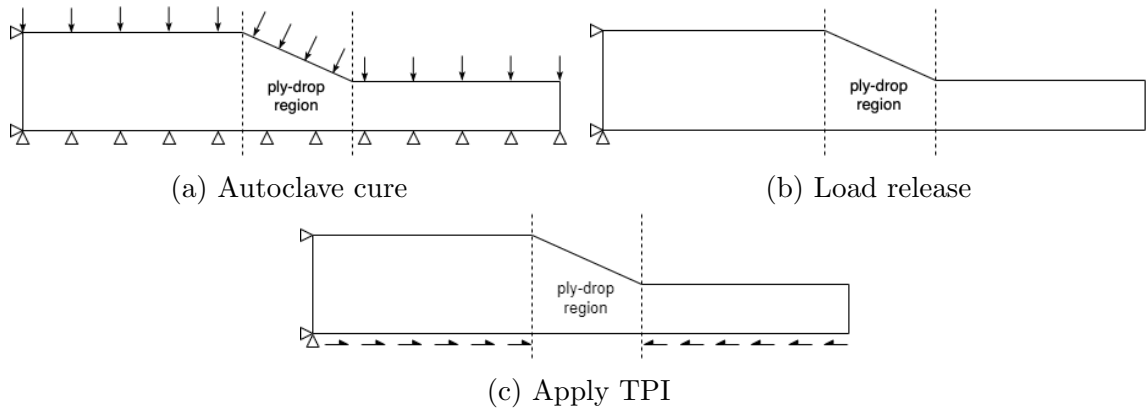


Figure 7.2: Boundary conditions for the (a) autoclave cure (b) load release and (c) TPI analyses steps in ABAQUS modelling

7.4 Investigation on the Influence of Ply-drops

The main focus of this study is to reveal how ply-drops affect the process-induced distortions in flat laminates, in particularly, around ply drop-off regions. A flat aluminium tool was used for manufacturing these specimens. Since a new tool was introduced in this chapter, the tool-part interactive effect was quantified through the semi-empirical method developed from the previous chapter. In addition, the surface smoothness was also checked.

7.4.1 Laminates without Ply-drops

The initial investigation was performed on three $[0/90]_s$ cross-ply specimen configurations without any ply drops. The specimens were measured 300 mm, 500 mm, 700 mm in length, and 60 mm in width. The measured warpage for each specimen was depicted in Figure 7.3. The displacement was taken along the mid-path and edge-path in the longitudinal direction. Their corresponding tool surface conditions were also plotted.

The results agrees well with the theoretical expectations. For the specimens with an increasing length of 300 mm, 500 mm and 700 mm, the maximum warpage measure 1.9 mm, 3.5mm and 8.9 mm. Adopting the semi-empirical approach to incorporate

the tool-part interaction effect, an effective shear stress was computed through curve fitting, shown in Figure 7.4. The fitted curve has a $R^2=0.97$.

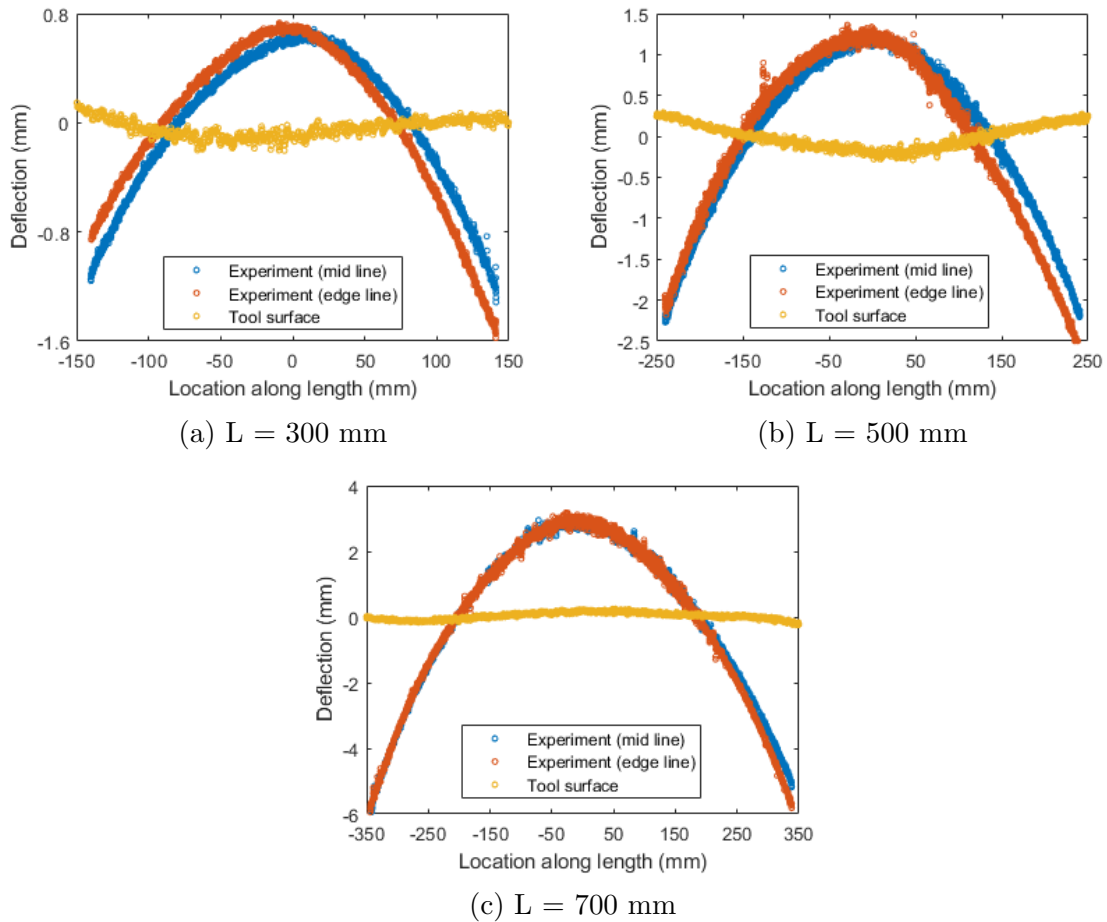


Figure 7.3: Distortion of specimens without any ply drops

Using the curve fitting method from section 6.3, for the given tool surface condition, a shear stress of 12.79 kPa was obtained, with its confidence interval of [9.59, 16.00] kPa. In the follow-up numerical study, this shear stress was assumed to be uniform and symmetric about the ply-drop zone.

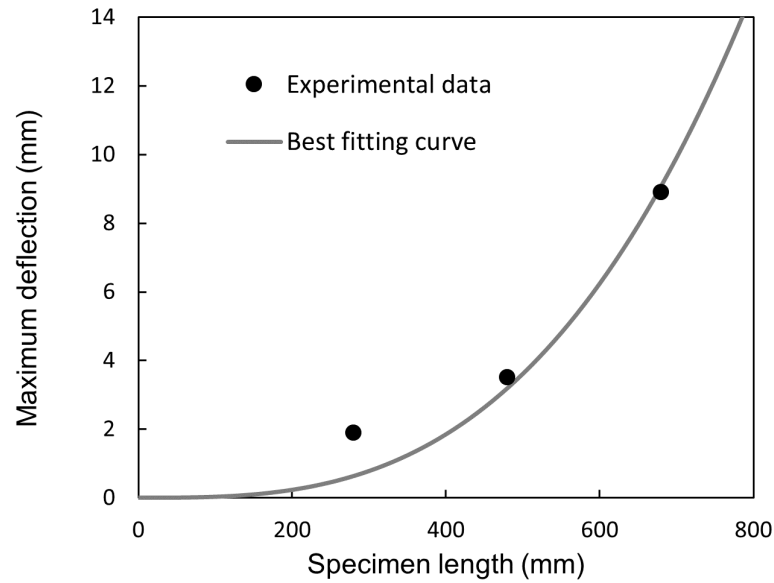


Figure 7.4: Determining tool-part shear stress through curve fitting to the experimental data

7.4.2 Laminates with Ply-drops

An initial investigation was performed on a 4-ply and 8-ply tapered laminates with ply-drops, the lay-up of which are shown in Figure 7.5. Both specimens dropped $[90^\circ]$ orientation plies at the middle, resulting in a transition from cross-ply quasi-isotropic laminates to unidirectional lamination. The specimens measure 100 mm in length and 50 mm in width. The primary focus of this study is to explore the distortion transition around ply-drop region.

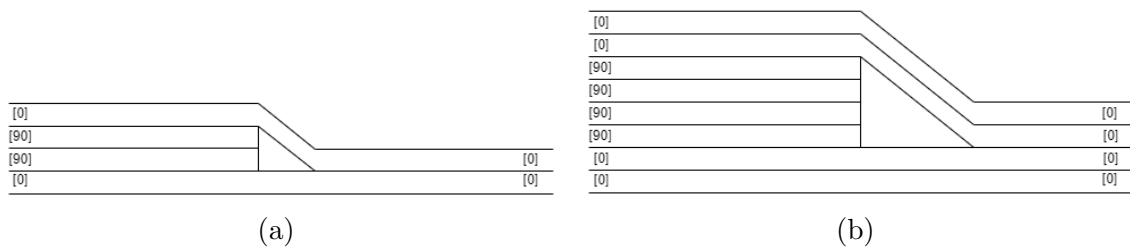


Figure 7.5: Design configuration of ply-drop from QI laminates to UD laminates

Figure 7.6 depicts the out-of-plane distortion field from a top view of two selected specimens. Distortion was primarily influenced by ply termination at the middle area. The absence of constraints in the $[90^\circ]$ orientation induced significant warpage

at the ply drop-off region.

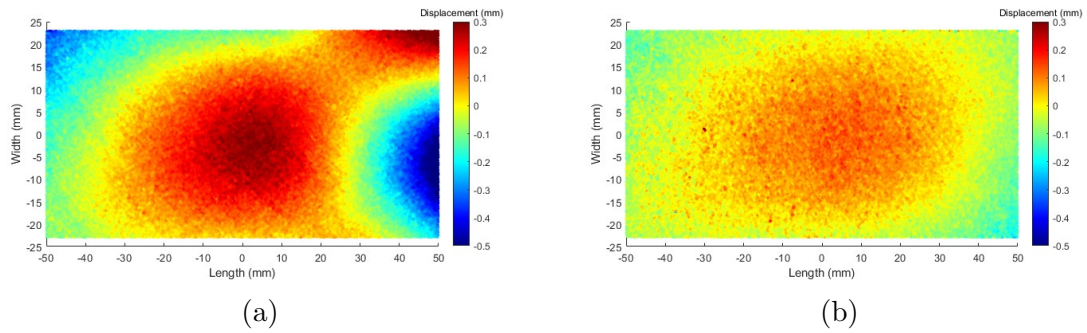


Figure 7.6: Warpage measurement of a (a) 4-to-2 ply-drop and (b) a 8-to-4 ply-drop specimens from a top view

Plotting the displacement along the width direction gives the maximum warpage of all six specimens, shown in Figure 7.7. For the 4-to-2 ply laminates, the maximum warpage in width direction was approximately 0.45 mm; whereas for the 8-to-4 ply laminates, the maximum warpage in the same direction was around 0.25 mm.

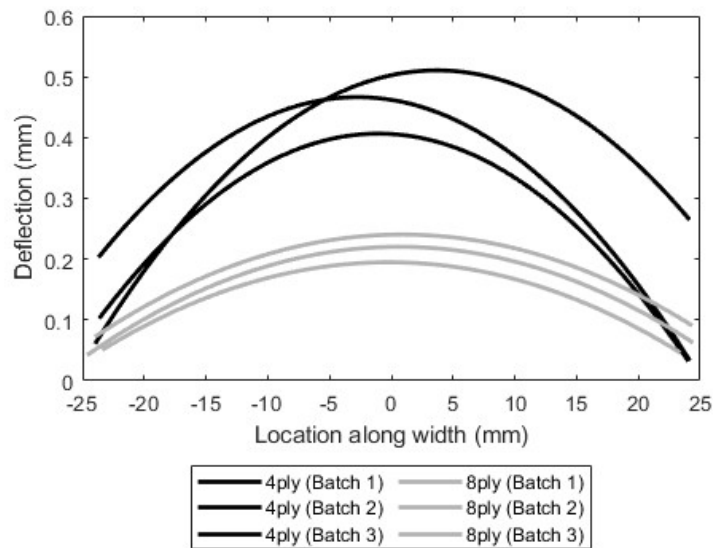


Figure 7.7: Experimental warpage along width direction at the drop-off zone

Meanwhile, the numerical prediction overestimates the maximum warpage compared to the experimental findings. The experimental and numerical results were tabulated in Table 7.1. The out-of-plane displacement fields of two laminates are shown in Figure 7.8.

One of the potential reasons for such discrepancies between the experimental and numerical findings could be the squeeze flow at the resin rich zone. Fibres oriented at $[90^\circ]$ could easily be squeezed into the resin-rich area under compaction force. Therefore, it can be understood that since there are more fibre constrains in the width direction at the resin pocket area, the experimental specimen exhibits smaller warpage in that direction. This phenomenon should better be proven through microscopic samples at the resin-rich regions. From numerical study, modelling the resin pocket filled with composite rather than pure resin would also be useful.

Despite the magnitude difference, the model successfully captured the distortion induced by stiffness change at the ply-drop region. In the longitudinal direction, $[0^\circ]$ -oriented plies do not change before and after the ply-drop region, while in the width direction, dropping $[90^\circ]$ -oriented plies results in warpage distortion. Similar to the experimental findings, the predicted maximum warpage in width direction was 0.50 mm for the 4-to-2 ply laminates, and for the 8-to-4 ply laminates, the maximum warpage in the same direction was 0.26 mm.

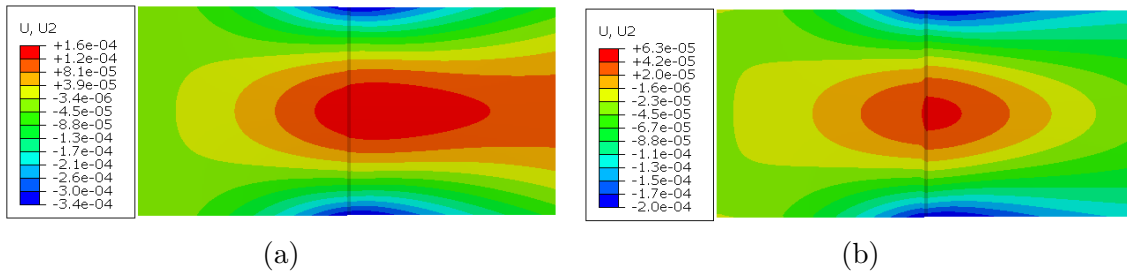


Figure 7.8: Distortion prediction of the (a) 4-to-2 ply and (b) 8-to-4 ply laminates (unit = m)

	Lay-up	Batch 1	Batch 2	Batch3	Prediction
Max. warpage (mm)	4-to-2	0.35	0.35	0.38	0.50
	8-to-4	0.13	0.15	0.13	0.26

Table 7.1: Comparison between experimental and numerically predicted warpage for two specimen configurations

This case study limited the size of the specimen to a length of 100 mm and a width of 50 mm. Tool-part interaction was not yet considered. In the following sections,

specimens were designed to be 240 mm in length and 60 mm in width, on which scale the tool-part interactive effect cannot be neglected.

7.4.3 Effect of Dropped Ply Orientations

The preceding section demonstrated how dropping plies affected the local stiffness, which triggered process-induced distortion to develop. Building upon these findings, the investigation also explored the impact of dropping a $[0^\circ]$ -oriented ply in comparison to dropping a $[90^\circ]$ -oriented ply. The design configurations of both specimens were illustrated in Figure 7.9, with dropped ply highlighted in grey. The ply-drop region was chosen to be in the middle along the total length.

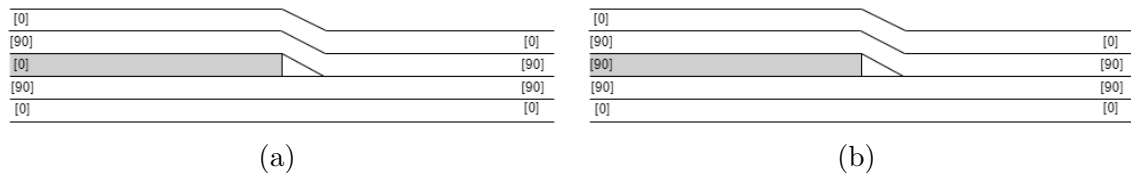


Figure 7.9: Design configuration of specimens with dropped ply of (a) $[0]$ orientation and (b) $[90]$ orientation

Figure 7.10 and Figure 7.11 shows the distortion comparison between specimens dropping $[0^\circ]$ -oriented ply and those dropping $[90^\circ]$ -oriented ply. Overall, the specimens with $[90^\circ]$ oriented ply-drop shows larger distortions in the longitudinal direction. One obvious interpretation is that $[0^\circ]$ -oriented ply provides more stiffness in the longitudinal direction, hence resulting in smaller warpage.

Figure 7.10 (b) and Figure 7.11 (b) also show slightly skewed shape in the distortion pattern. Such asymmetry of the distortion field could be the result of many factors. One major factor could be the difference of D_{12} or D_{66} of the laminates before and after ply-drop region. Other reasons could be the lack of uniform continuity along the width direction, particularly at the resin-rich area. The irregular size of resin pockets, coupled with the possibility of voids, contributes to this inconsistency.

Table 7.2 shows the comparison between the numerically predicted warpage and

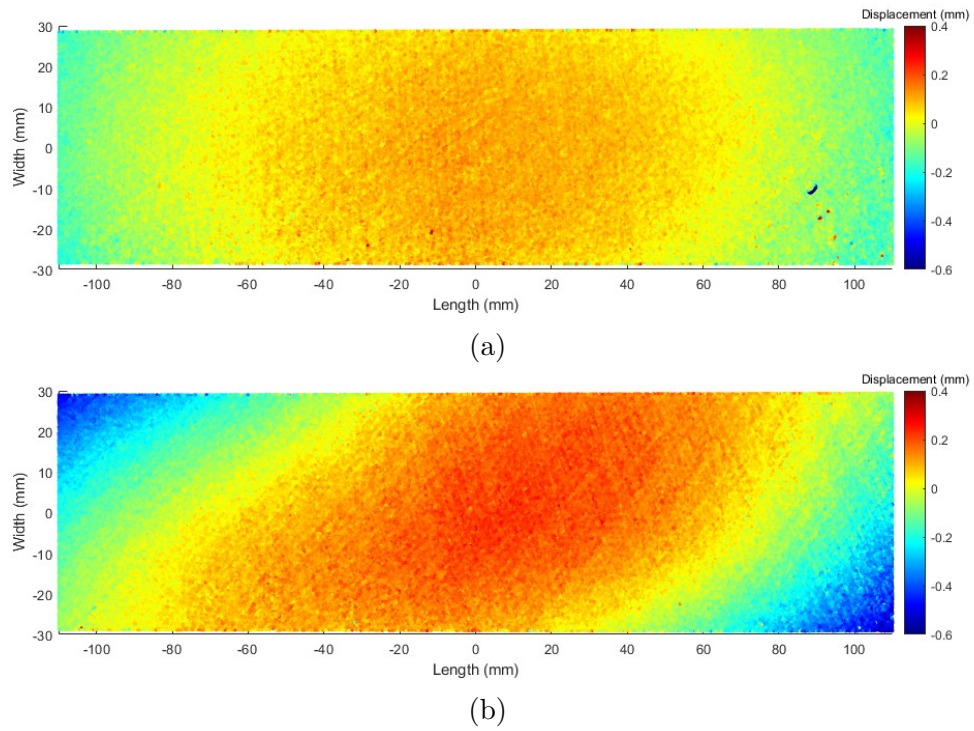


Figure 7.10: Distortion of specimens dropping (a) [0]-oriented ply and (b) [90]-oriented ply (batch 1)

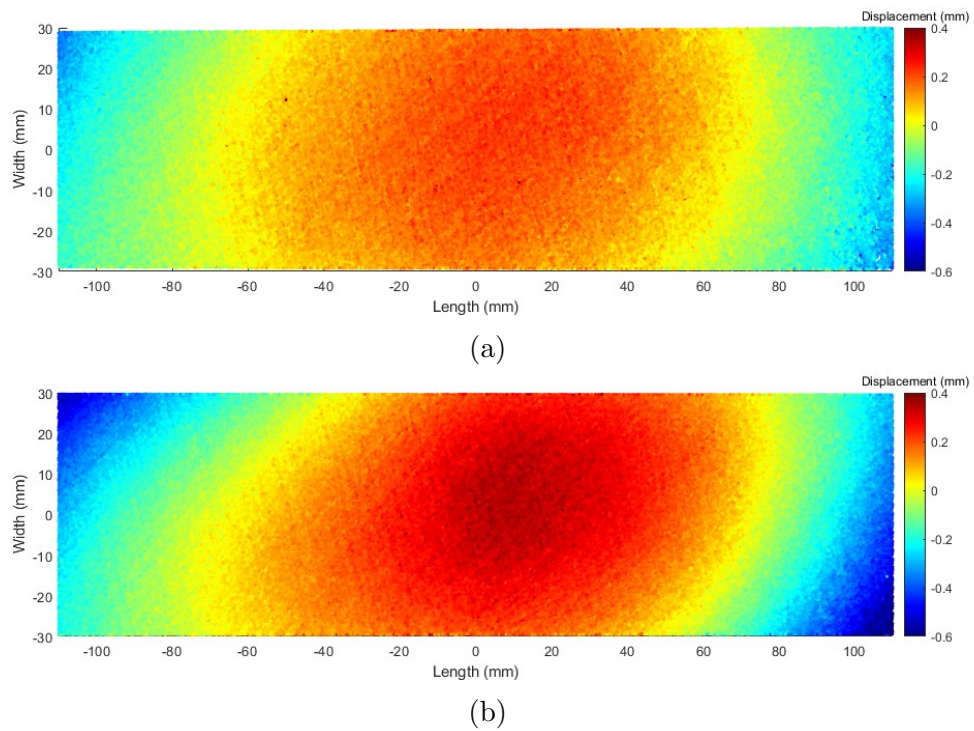


Figure 7.11: Distortion of specimens dropping (a) [0]-oriented ply and (b) [90]-oriented ply (batch 2)

the experimentally measured warpage. For some reason, the numerical prediction cannot capture the phenomenon seen from the experimental findings. The distortion due to TPI effect was overestimated. In addition, numerically prediction indicates that the distortion due to ply-drop is negligible.

		Experiment	Maximum warpage (mm)	
			Prediction w/o TPI	Prediction w. TPI
Drop [0°] ply	Batch 1	0.30	0.04	1.34
	Batch 2	0.40		
Drop [90°] ply	Batch 1	0.55	0.00	1.30
	Batch 2	0.80		

Table 7.2: Experimental measurement and numerical prediction of the maximum warpage in 5to4 ply-drop specimens

7.4.4 Effect of Number of Dropped Plies

Following the previous section, the study took a further step to examine the magnitude of warpage when two [0°]-oriented plies were dropped at the middle area, in comparison to the single [0°] ply-drop. The design configurations of both were depicted in Figure 7.12.

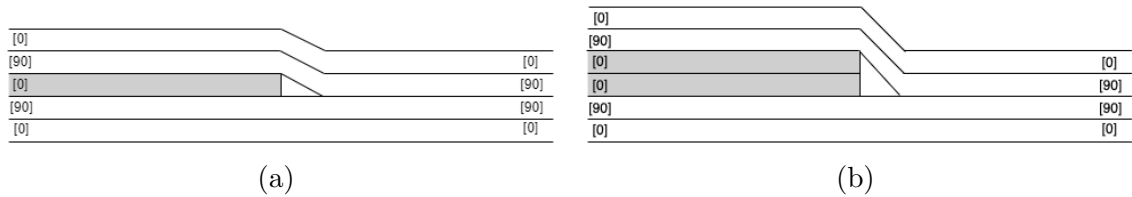


Figure 7.12: Design configuration of specimens dropping (a) single [0°]-oriented ply and (b) double [0°]-oriented plies

The experimental findings for the specimens with double ply drop were illustrated in Figure 7.13. For the ease of comparison, the displacement scale was kept the same as in Figure 7.10 and Figure 7.11 in the previous section. It can be observed that dropping two plies induced larger warpage when compared to the specimen dropping single ply, despite that 6-to-4 ply-drop specimen has higher bending stiffness at the thicker side of the laminate.

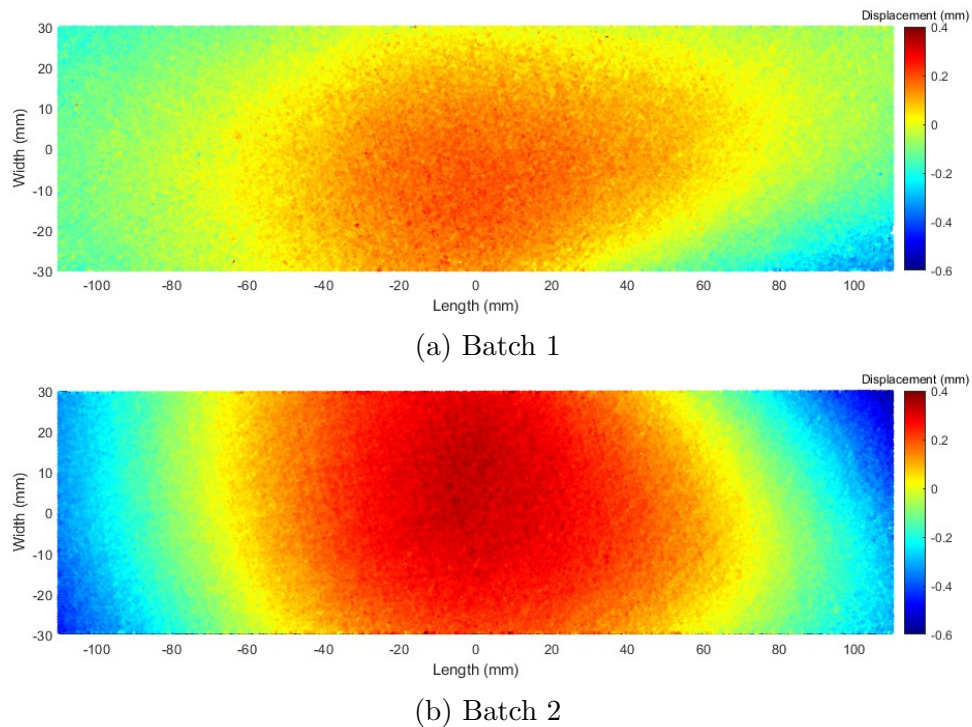


Figure 7.13: Experimental distortion of specimens dropping (a) single $[0^\circ]$ -oriented ply and (b) double $[0^\circ]$ -oriented plies

However, the observed warpage for dropping different number of plies were not captured in the numerical prediction. Table 7.3 summarised the experimentally measured and numerically predicted warpage in specimens from two batches. This might indicate that for unbalanced but symmetric lay-ups, as shown in Figure 7.9 and Figure 7.12, the distortion mechanism associated with ply-drop was not fully understood. Furthermore, the model reported a smaller warpage for dropping two plies compared with that dropping one plies. This could be contributed to the modelling geometry of the resin pocket. In this study, the geometry of the resin pocket is kept the same for both analyses. However, the reality could be very much different. For a better understanding of the observed phenomenon, a microscopy sample could be helpful.

		Experiment	Maximum warpage (mm)	
			Prediction w/o TPI	Prediction w. TPI
Drop single ply	Batch 1	0.30	0.04	1.34
	Batch 2	0.40		
Drop double plies	Batch 1	0.40	0.06	1.15
	Batch 2	0.80		

Table 7.3: Experimental measurement and numerical prediction of the maximum warpage in specimens dropping single and double $[0^\circ]$ plies

7.4.5 Effect of Ply-drop Strategies

Having investigated the effect of dropped ply orientation and the number of dropped plies for laminates consisting 4 to 6 plies, this study further explored topic by investigating ply-drop scenarios in balanced and symmetric laminates at both thick and thin ends.

Figure 7.14 shows three tapered laminates with different ply drop strategies. All three specimens were dropped from $[0^\circ/90^\circ/0^\circ/90^\circ]_s$ 8-ply to $[0^\circ/90^\circ]_s$ 4-ply, while different ply-drop designs resulted in different tapered ratios. The size of the specimens is 240 mm in length and 60 mm in width, with the ply-drop region in the middle. The distance between two successive ply-drops was denoted as ' d '. In Figure 7.14 (a), four plies were dropped together, corresponding to a maximum tapered ratio. In Figure 7.14 (b), the distance between two successive drop-offs is 15 mm. In Figure 7.14 (c), the distance between two adjacently dropped plies is 5 mm. This is close to the practical ply-drop goal where a smoother tapered ratio was pursued.

Two batches of specimens were manufactured in this study. The out-of-plane displacement fields from a top view of the first batch were depicted in Figure 7.15. It can be observed that the specimen with 4 drop-off locations exhibits largest distortion compared to the distortions in the other cases. Typically, in practice, dropping more than one ply at a single location is discouraged to avoid stress concentration. However, in this study, the use of smoothly tapered laminates aimed to minimise the potential risk of delamination originating from the resin-pocket area, yet inevitably

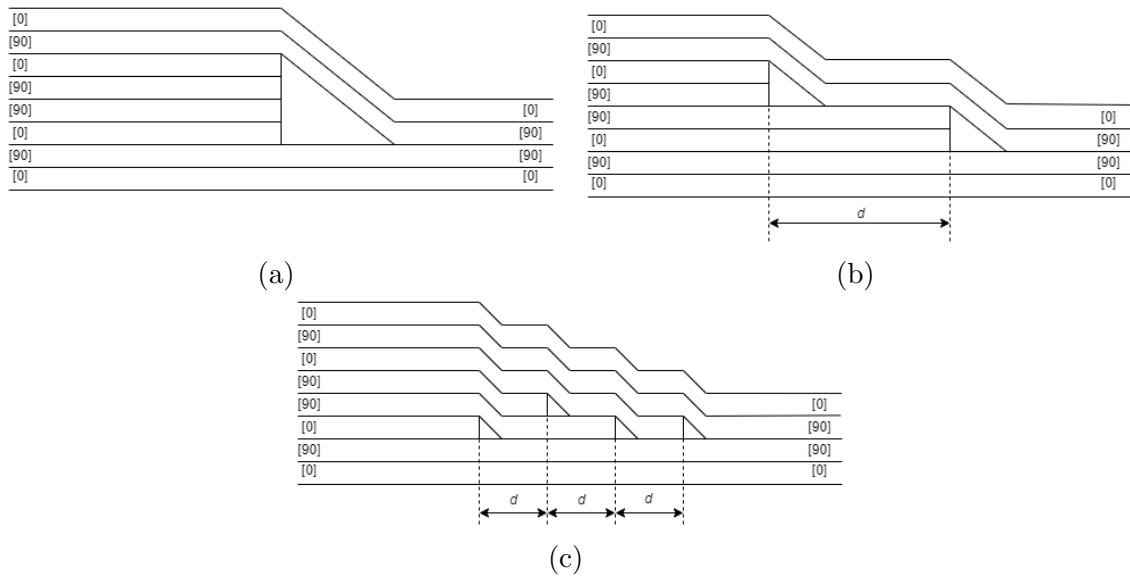
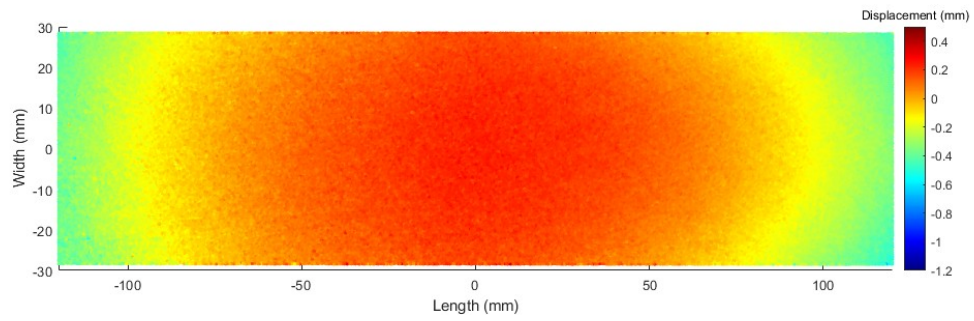


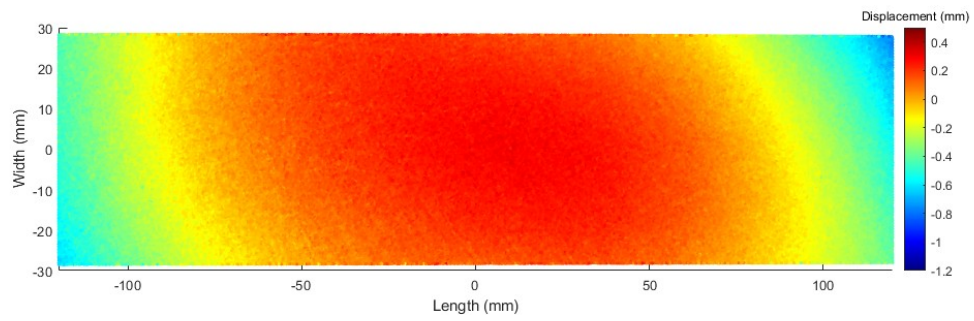
Figure 7.14: Design configuration of specimens with (a) 1 drop-off (b) 2 drop-offs and (c) 4 drop-offs

led to larger process-induced distortions. The exact warpage measurements along the length and width of all three specimens were also shown in Figure 7.16.

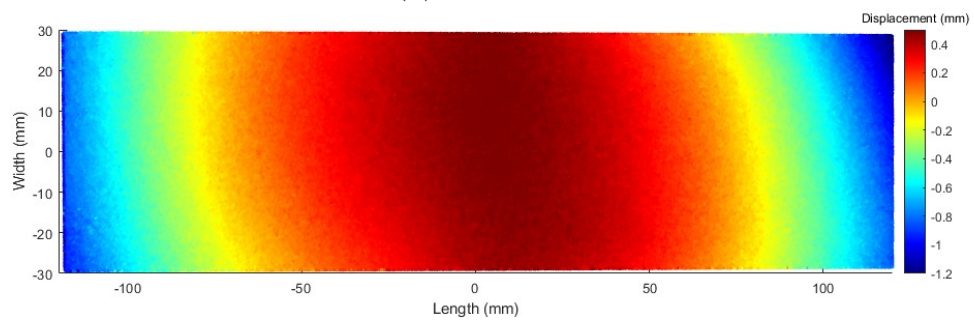
Comparing Figure 7.15 and Figure 7.17 reveals a notable batch-to-batch variation on the magnitude of distortion fields. The overall magnitude of the measured warpage from the first batch was greater than that from the second batch. Despite this variation, it is evident that the trend in the maximum warpage measured in the first batch agrees well with that of the second batch. The substantial batch-to-batch variation indicates uncertainties during the autoclave cure process that this study might have omitted. Furthermore, specimens manufactured at the different location of the tool could also contribute to the variability. In addition, the slightly skewed distortion field also indicates the uncertainties inherent in the prepreg material and hand lay-up operation.



(a) 1 drop-off

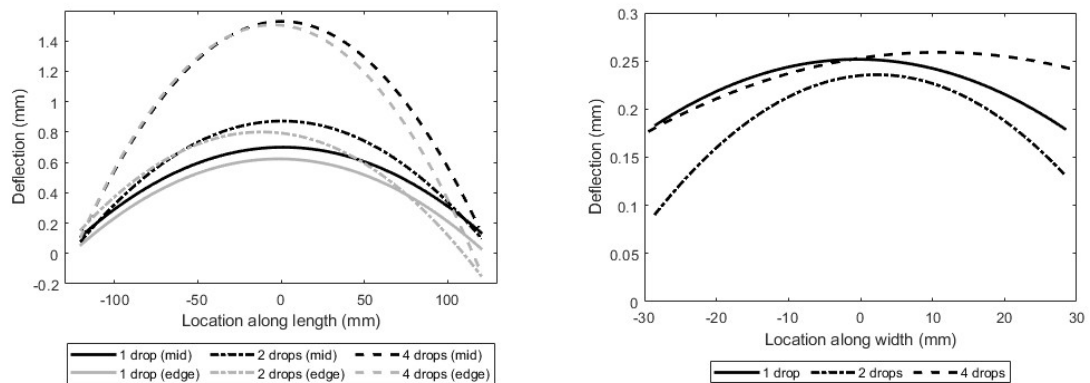


(b) 2 drop-offs



(c) 4 drop-offs

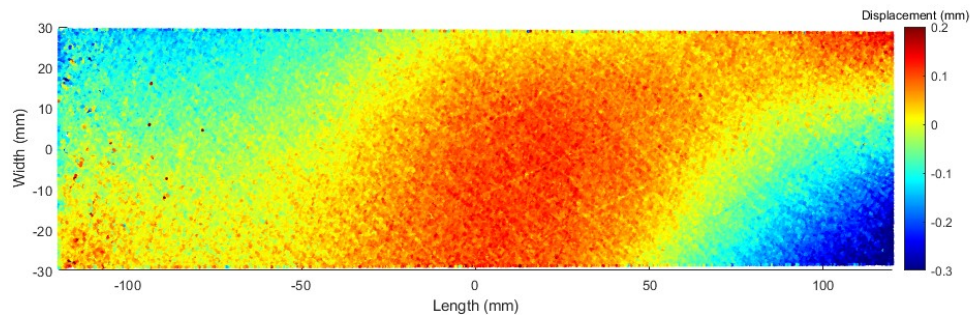
Figure 7.15: Experimental distortions of three specimens (batch 1)



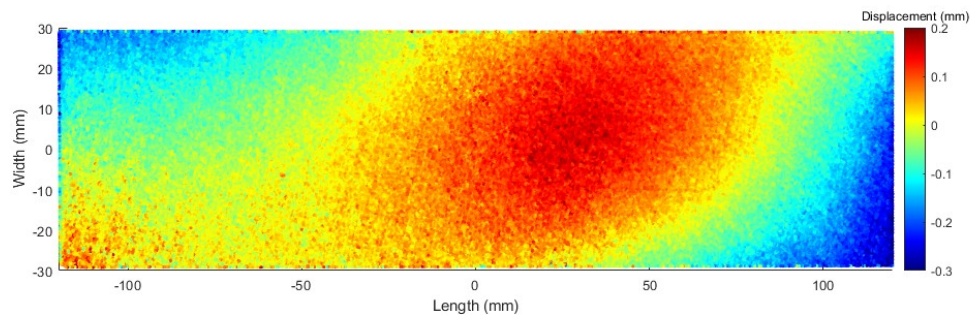
(a)

(b)

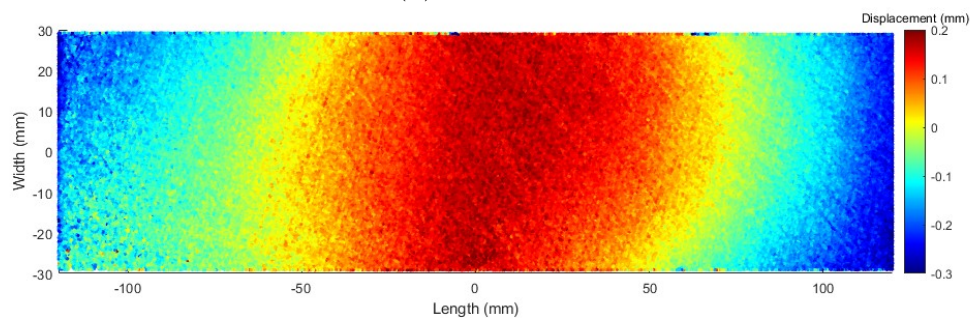
Figure 7.16: Warpage of specimens (a) along length and (b) along width at drop-off region (batch 1)



(a) 1 drop-off

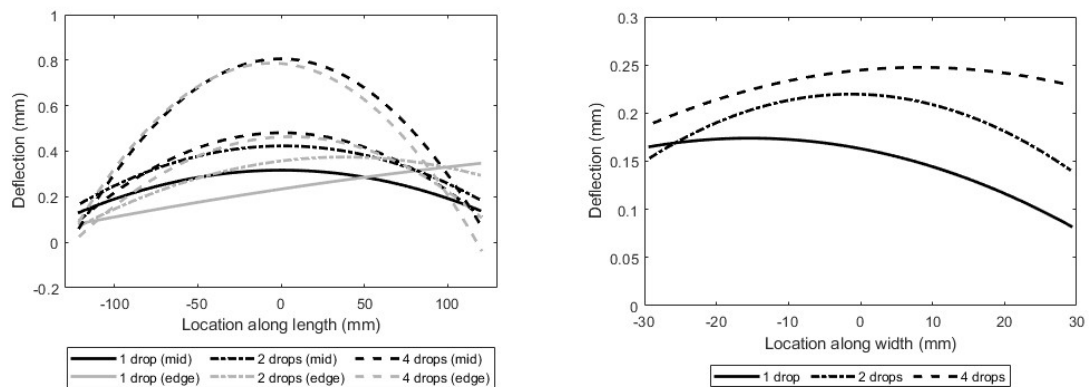


(b) 2 drop-offs



(c) 4 drop-offs

Figure 7.17: Experimental distortions of three specimens (batch 2)



(a)

(b)

Figure 7.18: Warpage of specimens (a) along length and (b) along width at drop-off region (batch2)

To uncover the distortion mechanism behind the observed phenomenon, numerical investigations were performed. The study found that the lay-up design and sequence at the ply-drop region play a key role in contributing to process-induced distortions. The model distinguished the process-induced distortion with and without the contribution from tool-part shear interaction. The predicted displacements of all three design configurations without applying tool-part shear stress were illustrated in Figure 7.19.

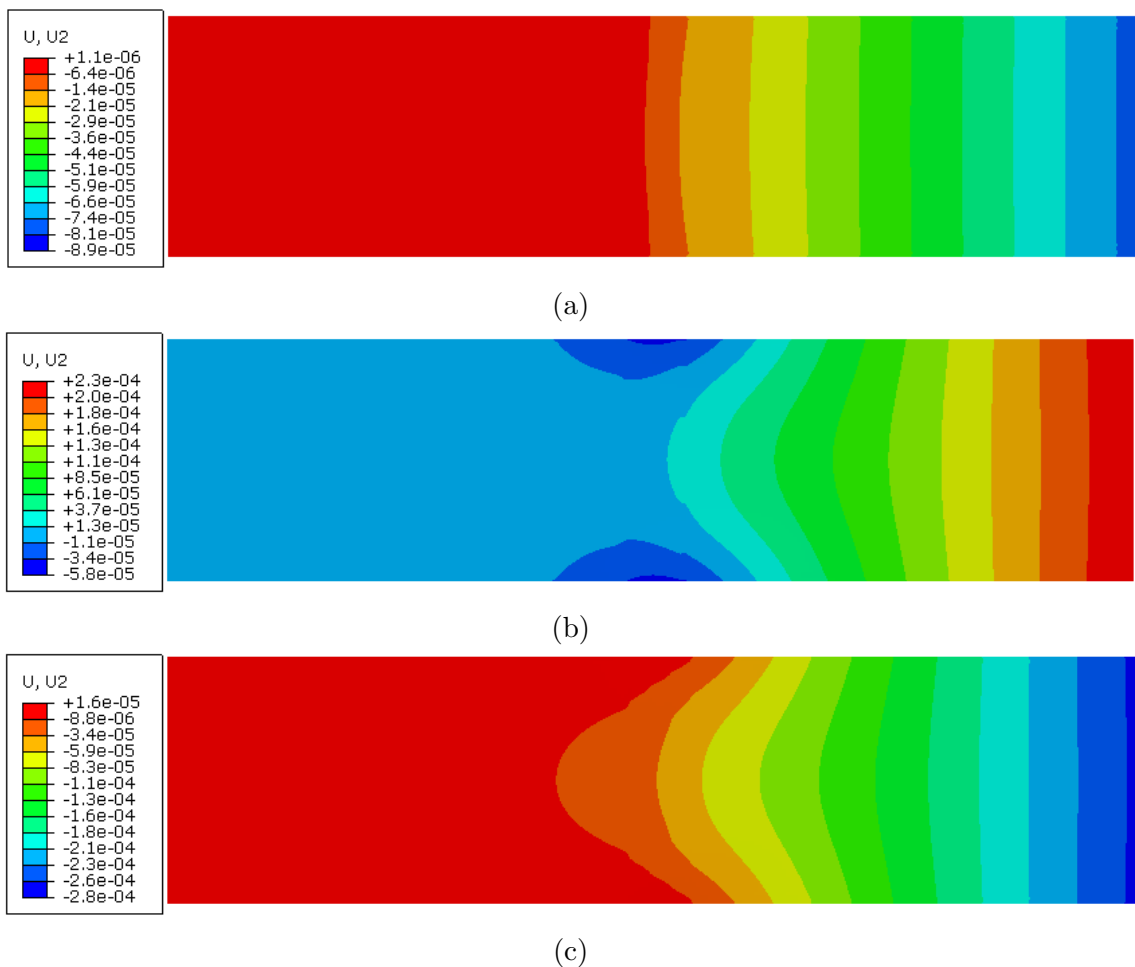


Figure 7.19: Distortion prediction of specimens with (a) 1 drop-off (b) 2 drop-offs and (c) 4 drop-offs without tool-part interaction effect (unit = m)

It is interesting to notice that in the case of the specimen (b), a reversed warpage was observed. This is primarily the result of unbalanced lay-up between two ply-drops. The lay-up sequence of $[0^\circ/90^\circ/90^\circ/0^\circ/90^\circ/0^\circ]$ indicates the unbalanced inter-lamina

stress generated within the specimen. The distance between two drops is 15 mm. The numerical study also found that reducing the distance from 15 mm to 5 mm yields reduced maximum displacement from 0.23 mm to 0.13 mm. Further reducing the distance to zero corresponds to the specimen dropping four plies together. Therefore, Figure 7.19 (a) indicates the lower bound of the warpage, the magnitude of the distortion is negligible.

Specimen (c) reported the largest warpage when comparing to the other two cases. Such phenomenon could again be explained as the consequence of unbalanced lay-up when looking at the lay-up sequence at the ply-drop region. The lay-up sequence after the first ply-drop is $[0^\circ/90^\circ/0^\circ/90^\circ/90^\circ/90^\circ/0^\circ]$, the lay-up sequence after the second ply-drop is $[0^\circ/90^\circ/0^\circ/90^\circ/90^\circ/0^\circ]$. Although the laminate before the first ply-drop and after the last ply-drop are balanced and symmetric, the tapered laminates spacing 15 mm generated a maximum displacement of 0.28 mm, the displacement field is shown in Figure 7.19 (c).

Up to this point, the distortion induced by the unbalanced lay-up at ply-drop regions has been numerically investigated. On top of the aforementioned distortion prediction, applying TPI gives the final warpage for all three specimens. Table 7.4 summarised the predicted maximum warpage of the specimens with and without considering tool-part interaction, in comparison to the experimental findings.

		Maximum warpage (mm)		
		Experiment	Prediction w/o TPI	Prediction w. TPI
Design (a)	Batch 1	0.60	0.09	0.94
	Batch 2	0.30		
Design (b)	Batch 1	0.80	-0.23	0.62
	Batch 2	0.30		
Design (c)	Batch 1	1.50	0.28	1.14
	Batch 2	0.50		

Table 7.4: Experimental measurement and numerical prediction of the maximum warpage in three specimens

It is evident that the specimen distortions contributed from TPI effect is more

significant when comparing to the non-TPI effect. From the numerical perspective, it is important to quantifying TPI effect so that the overall distortion could be best predicted.

7.4.6 Effect of Resin Pocket Ratio

As a supplementary investigation to the previous section, the effect of resin pocket ratio was also numerically investigated. In the previously presented simulation predictions, the resin pocket has a triangular ratio of 1:3. This modelling geometry was based on the microscopic sample as shown in Figure 7.1. However, for multiple plies dropped together, this assumption needs to be revised.

The study found that the maximum warpage for the models employing different resin pocket geometry differs in the case of specimen configuration shown in Figure 7.14 (a). As mentioned in Table 7.4, the predicted maximum warpage without TPI was only up to 0.09 mm. However, the model with a resin pocket ratio of 1:1 reported a maximum warpage of 0.34 mm.

It is therefore suggested that the resin pocket geometry to be characterised through microscopy image, so that the numerical prediction could better reflect the real cases.

7.5 Summary

This chapter investigated the process-induced distortion exhibited in the tapered laminates. The validity of the TPI model developed from the previous chapter was examined here. The shear stresses before and after the ply-drop zone are uniform and symmetric. This assumption is based on the observation that specimens exhibiting warpage shape of distortion. It is important to note that this assumption may not be applicable for specimens with more complex geometries or those exhibiting more intricate distortions.

The study also examined the validity of the developed modelling framework on predicting the distortion field of tapered laminates. The model distinguished the TPI and non-TPI contributions to specimen warpage. It was found that the lay-up sequence at the ply-drop zone is crucial in determining the displacement field due to non-TPI effect. Additionally, the study emphasised the importance of capturing microscopy images of ply-drop regions when modelling the geometry of the resin pocket.

To point out the insight of this study, the traditional design of a tapered laminate often prioritises the mechanical performance satisfying the load requirements. Ply-drop optimisation methods have been developed to fulfil this purpose. While many studies investigated the stress concentration and failure initiation at resin pockets, this chapter highlights that the distortion present in tapered laminates should also be considered during the design stage.

Chapter 8

Conclusions and Future Works

In this work, the process-induced distortions (PIDs) of laminated structures during the autoclave cure process was investigated. A simulation framework for predicting PIDs was developed and refined as the study explored a series of laminated structures with increased geometric complexities.

This framework was developed upon a thermal-chemical-mechanical analysis, where the temperature and degree-of-cure (DoC) domain were computed, and sequentially passed onto the mechanical model of the laminates. In the thermal-chemical analysis, internal heat generation was incorporated to account for exothermic reaction of the resin. In the mechanical analysis, process-induced thermal and chemical strains were determined from the temperature and DoC history field. At each time increment, the stiffness matrix was updated to compute the residual stress and displacement field.

The modelling procedure begins with a CLT-based Matlab model where forward discretisation method was employed. This model demonstrated the arise of residual stresses within a flat laminate when it experiences temperature or DoC gradient in the through-thickness direction. However, such gradient can be mitigated through

careful control of the cure cycle. The study emphasises the need to evaluate the manufacturing-recommended cure cycle, especially for producing thick laminates. Ideally, an optimised cure cycle should be pursued for a given structure to achieve an energy-efficient product without compromising its performance.

The developed model was then fully executed in ABAQUS to predict the spring-in angle of curved AS4/8552 laminates. Using the versatile user-subroutines provided by the FE package, the temperature-dependent and DoC dependent material properties can be specified. In this study, CHILE constitutive material model was employed. The spring-in angle with respect to the geometric features including thickness, radius and various lay-ups, were investigated. The study demonstrated that the spring-in angle increases as the arc-to-thickness ratio increases. From the numerical perspective, it also unveiled the shear-lag effect in governing the spring-in angle of a curved laminates, which in a good agreement with the findings in the literature.

Having explored the spring-in of a curved laminates, this research then investigated L-shaped laminates with consideration of TPI effect. Experimental work was conducted and compared with the numerical predictions. In total, 30 L-shaped specimens were manufactured, the design of which consists of different thickness, corner radius, flange length and lay-up sequence. Additional, 6 pieces of flat cross-ply specimens were manufactured to explore the TPI effect only. This work proposed a semi-empirical novel approach to predict TPI-induced warpage with the curve fitting data from a series of warpage measurement of specimens with varying lengths. On top of that, the proportion of chemical, thermal and TPI effects contributing to the total spring-in angle was investigated numerically. Results indicate that overall the CHILE material model underestimated the spring-in angle by 0.5° .

The validity of the developed modelling framework on predicting the distortion of tapered laminates was evaluated. The resin-rich area were microscopically examined,

from which the geometry of the resin pocket was identified. A total of 6 specimens without ply-drops and a total of 18 specimens with ply-drops were manufactured. This work found that the lay-up sequence at the ply-drop zone is crucial in determining the displacement field due to non-TPI effect. However, the magnitude of warpage due to TPI is still the major factor when compared with that induced by non-TPI effect. Therefore, characterising the mechanism of tool-part interaction under the autoclave cure cycle is crucial for predicting distortion of laminates with more complex geometries, in particular, if an aluminium tool was used in the manufacturing process. This research also emphasised the importance of distortion prediction in tapered laminates at the design stage. Although the mechanical performance is the design priority for laminates with ply-drops, the PIDs could also be mitigated with careful ply-drop optimisation.

8.1 Concluding Remarks

- This work contributes to academic knowledge by developing a robust simulation framework for predicting PIDs in laminated structures, offering insights into complex distortion mechanisms during manufacturing processes. It also provides valuable experimental dataset of flat and L-shaped specimens made from IM7/8552 prepregs. In particular, this work proposed a novel semi-empirical approach to facilitate fast prediction of TPI effects on laminates.
- The research challenges described in Section 1.4 Research Objectives has been effectively tackled. The proposed TPI modelling approach is easy to adopt yet yields reliable warpage estimations, but its current limitation to simple geometries requires further efforts to extend its application to more complex geometries.
- This work has partially fulfilled the industrial need for precise prediction of

PIDs during manufacturing process. The proposed simulation framework is not limited to the autoclave cure process, but has a potential to be adapted to various cure process such as resin infusion process and resin transfer moulding, which are all relevant to the industrial interests.

8.2 Future Works

Remaining gaps in PID prediction include further understanding the TPI so that a more comprehensive modelling technique could be developed to account for the TPI effects. Firstly, the pressure applied at the vacuum surface is non-uniform, causing potential variation in the tool-part shear interaction. A pressure-dependent shear model could be developed. Alternatively, a precise model of the tool could also improve the accuracy of the PID prediction. The characterisation of the tool-part interaction should be experimentally designed so that a universal TPI model could be developed regardless the complexity of the geometry.

Building upon the existing modelling framework, potential area of future work is to include other factors contributing to PIDs. For instance, fibre volume fraction gradients around the corner of the L-shaped laminates could be included. In this work, the thickness variation has been experimental measured, but not implemented in the geometry of modelling. For a more accurate prediction of the PIDs, the thickness and fibre volume fraction variation could also be simulated.

From the perspective of input modelling parameters, all of the material characterisation data presented in this work was taken from the literature. However, batch-to-batch variation exists for the same manufacturing producer. The cured ply thickness of the IM7/8552 used in this work was very different from the data sheet. A sensitivity study could be performed to investigate the impact of the material variability on the prediction of PIDs.

8.2. FUTURE WORKS

In the investigation of laminates with ply-drops, microscopic images at the resin-rich area could be taken to facilitate the discussion of the PIDs. Furthermore, the geometry of the resin pocket could also be derived from the microscopic image so that a more precise prediction could be obtained.

Bibliography

(2023).

Advani, S. G. and Sozer, E. M. (2002). *Process modeling in composites manufacturing*. CRC press.

Albert, C. and Fernlund, G. (2002). Spring-in and warpage of angled composite laminates. *Composites Science and Technology*, 62(14):1895–1912.

Arafath, A. R. A., Vaziri, R., and Poursartip, A. (2008). Closed-form solution for process-induced stresses and deformation of a composite part cured on a solid tool: part i–flat geometries. *Composites Part A: Applied Science and Manufacturing*, 39(7):1106–1117.

Baran, I., Cinar, K., Ersoy, N., Akkerman, R., and Hattel, J. H. (2017). A review on the mechanical modeling of composite manufacturing processes. *Archives of computational methods in engineering*, 24(2):365–395.

Berthelot, J.-M. and Ling, F. F. (1999). *Composite materials: mechanical behavior and structural analysis*, volume 435. Springer.

Bogetti, T. A. and Gillespie Jr, J. W. (1992). Process-induced stress and deformation in thick-section thermoset composite laminates. *Journal of composite materials*, 26(5):626–660.

- Chen, W. and Zhang, D. (2019). Improved prediction of residual stress induced warpage in thermoset composites using a multiscale thermo-viscoelastic processing model. *Composites Part A: Applied Science and Manufacturing*, 126:105575.
- Dai, J., Xi, S., and Li, D. (2019). Numerical analysis of curing residual stress and deformation in thermosetting composite laminates with comparison between different constitutive models. *Materials*, 12(4):572.
- Darrow Jr, D. A. and Smith, L. V. (2002). Isolating components of processing induced warpage in laminated composites. *Journal of Composite Materials*, 36(21):2407–2419.
- Ding, A., Fang, S., Li, X., Sun, L., Wang, J., and Chen, H. (2022). Experimental and numerical investigation of tool-part interaction on the process-induced distortions in composite structures. *Composite Structures*, 279:114871.
- Ding, A., Li, S., Sun, J., Wang, J., and Zu, L. (2016a). A comparison of process-induced residual stresses and distortions in composite structures with different constitutive laws. *Journal of Reinforced Plastics and Composites*, 35(10):807–823.
- Ding, A., Li, S., Wang, J., Ni, A., Sun, L., and Chang, L. (2016b). Prediction of process-induced distortions in l-shaped composite profiles using path-dependent constitutive law. *Applied Composite Materials*, 23:1027–1045.
- Ding, A., Li, S., Wang, J., and Zu, L. (2015). A three-dimensional thermo-viscoelastic analysis of process-induced residual stress in composite laminates. *Composite Structures*, 129:60–69.
- Ding, A., Wang, J., Ni, A., and Li, S. (2019). A new analytical solution for cure-induced spring-in of l-shaped composite parts. *Composites Science and Technology*, 171:1–12.

- Ersoy, N., Garstka, T., Potter, K., Wisnom, M. R., Porter, D., Clegg, M., and Stringer, G. (2010a). Development of the properties of a carbon fibre reinforced thermosetting composite through cure. *Composites Part A: Applied Science and Manufacturing*, 41(3):401–409.
- Ersoy, N., Garstka, T., Potter, K., Wisnom, M. R., Porter, D., and Stringer, G. (2010b). Modelling of the spring-in phenomenon in curved parts made of a thermosetting composite. *Composites Part A: Applied Science and Manufacturing*, 41(3):410–418.
- Ersoy, N., Potter, K., Wisnom, M. R., and Clegg, M. J. (2005a). Development of spring-in angle during cure of a thermosetting composite. *Composites Part A: Applied Science and Manufacturing*, 36(12):1700–1706.
- Ersoy, N., Potter, K., Wisnom, M. R., and Clegg, M. J. (2005b). An experimental method to study the frictional processes during composites manufacturing. *Composites Part A: Applied science and manufacturing*, 36(11):1536–1544.
- Fernlund, G., Rahman, N., Courdji, R., Bresslauer, M., Poursartip, A., Willden, K., and Nelson, K. (2002). Experimental and numerical study of the effect of cure cycle, tool surface, geometry, and lay-up on the dimensional fidelity of autoclave-processed composite parts. *Composites part A: applied science and manufacturing*, 33(3):341–351.
- Garschke, C., Parlevliet, P., Weimer, C., and Fox, B. (2013). Cure kinetics and viscosity modelling of a high-performance epoxy resin film. *Polymer Testing*, 32(1):150–157.
- Garstka, T., Ersoy, N., Potter, K., and Wisnom, M. (2007). In situ measurements of through-the-thickness strains during processing of as4/8552 composite. *Composites Part A: applied science and manufacturing*, 38(12):2517–2526.

- Gillham, J. K. (1986). Formation and properties of thermosetting and high tg polymeric materials. *Polymer Engineering & Science*, 26(20):1429–1433.
- Hardis, R., Jessop, J. L., Peters, F. E., and Kessler, M. R. (2013). Cure kinetics characterization and monitoring of an epoxy resin using dsc, raman spectroscopy, and dea. *Composites Part A: Applied Science and Manufacturing*, 49:100–108.
- He, K., Hoa, S., and Ganesan, R. (2000). The study of tapered laminated composite structures: a review. *Composites Science and Technology*, 60(14):2643–2657.
- Hill, R. (1965). A self-consistent mechanics of composite materials. *Journal of the Mechanics and Physics of Solids*, 13(4):213–222.
- Hubert, P. (2023). Autoclave and out-of-autoclave processing of prepregs. In *Design and Manufacture of Structural Composites*, pages 209–236. Elsevier.
- Hubert, P., Johnston, A., Poursartip, A., and Nelson, K. (2001). Cure kinetics and viscosity models for hexcel 8552 epoxy resin. In *International SAMPE symposium and exhibition*, pages 2341–2354. SAMPE; 1999.
- Irisarri, F.-X., Lasseigne, A., Leroy, F.-H., and Le Riche, R. (2014). Optimal design of laminated composite structures with ply drops using stacking sequence tables. *Composite Structures*, 107:559–569.
- Javdanitehran, M., Berg, D. C., Duemichen, E., and Ziegmann, G. (2016). An iterative approach for isothermal curing kinetics modelling of an epoxy resin system. *Thermochimica Acta*, 623:72–79.
- Johnston, A., Vaziri, R., and Poursartip, A. (2001). A plane strain model for process-induced deformation of laminated composite structures. *Journal of composite materials*, 35(16):1435–1469.
- Johnston, A. A. (1997). *An integrated model of the development of process-induced*

- deformation in autoclave processing of composite structures*. PhD thesis, University of British Columbia.
- Kaddour, A. and Hinton, M. (2012). Input data for test cases used in benchmarking triaxial failure theories of composites. *Journal of Composite Materials*, 46(19-20):2295–2312.
- Kamal, M. and Sourour, S. (1973). Kinetics and thermal characterization of thermoset cure. *Polymer Engineering & Science*, 13(1):59–64.
- Kappel, E. (2016). Forced-interaction and spring-in–relevant initiators of process-induced distortions in composite manufacturing. *Composite Structures*, 140:217–229.
- Kappel, E., Stefaniak, D., and Hühne, C. (2013). Process distortions in prepreg manufacturing—an experimental study on cfrp l-profiles. *Composite Structures*, 106:615–625.
- Karkanias, P. I., Partridge, I. K., and Attwood, D. (1996). Modelling the cure of a commercial epoxy resin for applications in resin transfer moulding. *Polymer International*, 41(2):183–191.
- Kaushik, V. and Raghavan, J. (2010). Experimental study of tool–part interaction during autoclave processing of thermoset polymer composite structures. *Composites Part A: Applied Science and Manufacturing*, 41(9):1210–1218.
- Kenny, J., Apicella, A., and Nicolais, L. (1989). A model for the thermal and chemorheological behavior of thermosets. i: Processing of epoxy-based composites. *Polymer Engineering & Science*, 29(15):973–983.
- Kenny, J., Maffezzoli, A., and Nicolais, L. (1990). A model for the thermal and chemorheological behavior of thermoset processing:(ii) unsaturated polyester

- based composites. *Composites Science and Technology*, 38(4):339–358.
- Khoun, L. (2009). *Process-induced stresses and deformations in woven composites manufactured by resin transfer moulding*. PhD thesis, McGill University Montreal.
- Khoun, L., Centea, T., and Hubert, P. (2010). Characterization methodology of thermoset resins for the processing of composite materials—case study: Cycom 890rtm epoxy resin. *Journal of Composite Materials*, 44(11):1397–1415.
- Khoun, L. and Hubert, P. (2010). Cure shrinkage characterization of an epoxy resin system by two in situ measurement methods. *Polymer Composites*, 31(9):1603–1610.
- Kim, J., Moon, T. J., and Howell, J. R. (2002). Cure kinetic model, heat of reaction, and glass transition temperature of as4/3501-6 graphite–epoxy prepregs. *Journal of Composite Materials*, 36(21):2479–2498.
- Lee, W. I., Loos, A. C., and Springer, G. S. (1982). Heat of reaction, degree of cure, and viscosity of hercules 3501-6 resin. *Journal of Composite Materials*, 16(6):510–520.
- Li, C., Potter, K., Wisnom, M. R., and Stringer, G. (2004). In-situ measurement of chemical shrinkage of my750 epoxy resin by a novel gravimetric method. *Composites Science and Technology*, 64(1):55–64.
- Liu, X., Guan, Z., Wang, X., Jiang, T., Geng, K., and Li, Z. (2021). Study on cure-induced residual stresses and spring-in deformation of l-shaped composite laminates using a simplified constitutive model considering stress relaxation. *Composite Structures*, 272:114203.
- Moretti, L., Castanié, B., Bernhart, G., and Olivier, P. (2020). Characterization and

- modelling of cure-dependent properties and strains during composites manufacturing. *Journal of Composite Materials*, 54(22):3109–3124.
- Mulle, M., Collombet, F., Olivier, P., and Grunevald, Y.-H. (2009). Assessment of cure residual strains through the thickness of carbon–epoxy laminates using fbgs, part i: Elementary specimen. *Composites Part A: Applied Science and Manufacturing*, 40(1):94–104.
- Naji, M. I. and Hoa, S. V. (1999). Curing of thick angle-bend thermoset composite part: curing cycle effect on thickness variation and fiber volume fraction. *Journal of reinforced Plastics and Composites*, 18(8):702–723.
- Nawab, Y., Shahid, S., Boyard, N., and Jacquemin, F. (2013). Chemical shrinkage characterization techniques for thermoset resins and associated composites. *Journal of Materials Science*, 48(16):5387–5409.
- Nelson, R. H. and Cairns, D. S. (1989). Prediction of dimensional changes in composite laminates during cure. *Tomorrow’s Materials: Today.*, 34:2397–2410.
- O’Brien, D. J., Mather, P. T., and White, S. R. (2001). Viscoelastic properties of an epoxy resin during cure. *Journal of composite materials*, 35(10):883–904.
- O’Brien, T. K. and Krueger, R. (2001). Analysis of ninety degree flexure tests for characterization of composite transverse tensile strength. Technical report.
- Parlevliet, P. P., Bersee, H. E., and Beukers, A. (2007). Residual stresses in thermoplastic composites—a study of the literature. part iii: Effects of thermal residual stresses. *Composites Part A: Applied Science and Manufacturing*, 38(6):1581–1596.
- Paul, P. C., Saff, C., Sanger, K. B., Mahler, M., Kan, H. P., and Kautz, E. F. (1990). Out of plane analysis for composite structures. In *NASA. Langley*

- Research Center, Eighth DOD (NASA) FAA Conference on Fibrous Composites in Structural Design, Part 1.*
- Peeters, D., Deane, M., O'Higgins, R., and Weaver, P. M. (2020). Morphology of ply drops in thermoplastic composite materials manufactured using laser-assisted tape placement. *Composite Structures*, 251:112638.
- Qiao, W. and Yao, W. (2020). Modelling of process-induced deformation for composite parts considering tool-part interaction. *Materials*, 13(20):4503.
- Radford, D. and Diefendorf, R. (1993). Shape instabilities in composites resulting from laminate anisotropy. *Journal of Reinforced Plastics and Composites*, 12(1):58–75.
- Radford, D. and Rennick, T. (2000). Separating sources of manufacturing distortion in laminated composites. *Journal of Reinforced Plastics and Composites*, 19(8):621–641.
- Ratcliffe, J. G., Czabaj, M. W., and O'Brien, T. K. (2013). A test for characterizing delamination migration in carbon/epoxy tape laminates. Technical report.
- Reddy, J. N. (2004). *Mechanics of laminated composite plates and shells: theory and analysis*. CRC press.
- Russell, J. D., Madhukar, M. S., Genidy, M. S., and Lee, A. Y. (2000). A new method to reduce cure-induced stresses in thermoset polymer composites, part iii: correlating stress history to viscosity, degree of cure, and cure shrinkage. *Journal of composite materials*, 34(22):1926–1947.
- Saad, M. T., Miller, S. G., and Marunda, T. (2014). Thermal characterization of im7/8552-1 carbon-epoxy composites. In *ASME International mechanical engineering congress and exposition*, volume 46569, page V08BT10A091. American

- Society of Mechanical Engineers.
- Shah, D. U. and Schubel, P. J. (2010). Evaluation of cure shrinkage measurement techniques for thermosetting resins. *Polymer Testing*, 29(6):629–639.
- Sun, L., Wang, J., Ni, A., Li, S., and Ding, A. (2017). Modelling and experiment of process-induced distortions in unsymmetrical laminate plates. *Composite Structures*, 182:524–532.
- Svanberg, J., Altkvist, C., and Nyman, T. (2005). Prediction of shape distortions for a curved composite c-spar. *Journal of reinforced plastics and composites*, 24(3):323–339.
- Svanberg, J. M. and Holmberg, J. (2001). An experimental investigation on mechanisms for manufacturing induced shape distortions in homogeneous and balanced laminates. *Composites Part A: Applied Science and Manufacturing*, 32(6):827–838.
- Svanberg, J. M. and Holmberg, J. A. (2004). Prediction of shape distortions part i. fe-implementation of a path dependent constitutive model. *Composites part A: applied science and manufacturing*, 35(6):711–721.
- Takagaki, K., Minakuchi, S., and Takeda, N. (2017). Process-induced strain and distortion in curved composites. part ii: Parametric study and application. *Composites Part A: Applied Science and Manufacturing*, 103:219–229.
- Traiforos, N., Matveev, M., Chronopoulos, D., and Turner, T. (2023). Spring-in of composite l-shape specimens: An experimental and numerical investigation. *Composite Structures*, 310:116772.
- Traiforos, N., Turner, T., Runeberg, P., Fernass, D., Chronopoulos, D., Glock, F., Schuhmacher, G., and Hartung, D. (2021). A simulation framework for pre-

- dicting process-induced distortions for precise manufacturing of aerospace thermoset composites. *Composite Structures*, 275:114465.
- Trofimov, A., Le-Pavic, J., Ravey, C., Albouy, W., Therriault, D., and Lévesque, M. (2021). Multi-scale modeling of distortion in the non-flat 3d woven composite part manufactured using resin transfer molding. *Composites Part A: Applied Science and Manufacturing*, 140:106145.
- Twigg, G., Poursartip, A., and Fernlund, G. (2003). An experimental method for quantifying tool–part shear interaction during composites processing. *Composites Science and Technology*, 63(13):1985–2002.
- Twigg, G., Poursartip, A., and Fernlund, G. (2004a). Tool–part interaction in composites processing. part i: experimental investigation and analytical model. *Composites Part A: Applied Science and Manufacturing*, 35(1):121–133.
- Twigg, G., Poursartip, A., and Fernlund, G. (2004b). Tool–part interaction in composites processing. part ii: numerical modelling. *Composites Part A: Applied Science and Manufacturing*, 35(1):135–141.
- Um, M.-K., Daniel, I. M., and Hwang, B.-S. (2002). A study of cure kinetics by the use of dynamic differential scanning calorimetry. *Composites Science and Technology*, 62(1):29–40.
- Wang, B., Fan, S., Chen, J., Yang, W., Liu, W., and Li, Y. (2023). A review on prediction and control of curing process-induced deformation of continuous fiber-reinforced thermosetting composite structures. *Composites Part A: Applied Science and Manufacturing*, 165:107321.
- White, S. R. and Kim, Y. K. (1998). Process-induced residual stress analysis of as4/3501-6 composite material. *Mechanics of Composite Materials and Structures an International Journal*, 5(2):153–186.

- Wisnom, M., Gigliotti, M., Ersoy, N., Campbell, M., and Potter, K. (2006). Mechanisms generating residual stresses and distortion during manufacture of polymer–matrix composite structures. *Composites Part A: Applied Science and Manufacturing*, 37(4):522–529.
- Wisnom, M. R., Potter, K. D., and Ersoy, N. (2007). Shear-lag analysis of the effect of thickness on spring-in of curved composites. *Journal of Composite Materials*, 41(11):1311–1324.
- Xiao, Y., Li, D., Qian, Z., and Li, Y. (2023). An experimental and numerical study of curing deformation considering tool-part interaction for two-step curing tooling composite materials. *Journal of Manufacturing Processes*, 94:435–453.
- Xin, C., Li, M., Gu, Y., Luo, J., and Zhang, Z. (2011). Study on the resin flow and fiber compaction of tapered composite laminates during autoclave processing. *Journal of Reinforced Plastics and Composites*, 30(16):1399–1411.
- Yuan, Z., Wang, Y., Peng, X., Wang, J., and Wei, S. (2016). An analytical model on through-thickness stresses and warpage of composite laminates due to tool–part interaction. *Composites Part B: Engineering*, 91:408–413.
- Yuan, Z., Wang, Y., Wang, J., Wei, S., Liu, T., Cai, Y., He, J., and Wang, W. (2018). A model on the curved shapes of unsymmetric laminates including tool-part interaction. *Science and Engineering of Composite Materials*, 25(1):1–8.
- Zbed, R. S., Le Corre, S., and Sobotka, V. (2022). Process-induced strains measurements through a multi-axial characterization during the entire curing cycle of an interlayer toughened carbon/epoxy prepreg. *Composites Part A: Applied Science and Manufacturing*, 153:106689.
- Zeng, X. and Raghavan, J. (2010). Role of tool-part interaction in process-induced warpage of autoclave-manufactured composite structures. *Composites Part A:*

- Applied Science and Manufacturing*, 41(9):1174–1183.
- Zhao, L., Warrior, N., and Long, A. (2006). A micromechanical study of residual stress and its effect on transverse failure in polymer–matrix composites. *International journal of solids and structures*, 43(18-19):5449–5467.
- Zobeiry, N., Vaziri, R., and Poursartip, A. (2010). Computationally efficient pseudo-viscoelastic models for evaluation of residual stresses in thermoset polymer composites during cure. *Composites Part A: Applied Science and Manufacturing*, 41(2):247–256.
- Zocher, M., Groves, S., and Allen, D. H. (1997). A three-dimensional finite element formulation for thermoviscoelastic orthotropic media. *International Journal for Numerical Methods in Engineering*, 40(12):2267–2288.